Max Planck Institute
of Colloids and Interfaces

Universität Potsdam

Coiled Coils as Molecular Force Sensors for the Extracellular Matrix

---

Dissertation

zur Erlangung des akademischen Grades
"doctor rerum naturalium"
(Dr. rer. nat.)
in der Wissenschaftsdisziplin "Physikalische Biochemie"

eingereicht an der
Mathematisch-Naturwissenschaftlichen Fakultät
Institut für Biochemie und Biologie
der Universität Potsdam

angefertigt in der
Max-Planck-Forschungsgruppe "Mechano(bio)chemie"
Max-Planck-Institut für Kolloid- und Grenzflächenforschung

von
Melis Goktas

Potsdam, January 2019

Declaration

The enclosed research was conducted in the Max Planck Research Group ‘Mechano(bio)chemistry’ at the Max Planck Institute of Colloids and Interfaces (MPIKG), under the supervision of Dr. Kerstin G. Blank between October 2014 and September 2018. This thesis has not been submitted for any other qualifications at this or any other institution. This dissertation is the original work of the author and does not include any research that is the outcome of work done in collaboration with others, apart from those specifically indicated in the text and acknowledgements.

Eidesstattliche Erklärung

Die vorliegende Arbeit wurde in der Zeit von Oktober 2014 bis September 2018 am Max-Planck-Institut für Kolloid- und Grenzflächenforschung in der Max-Planck-Forschungsgruppe 'Mechano(bio)chemie' unter der Leitung von Dr. Kerstin G. Blank angefertigt. Die Arbeit ist bisher an keiner anderen Hochschule eingereicht worden und wurde zudem selbständig und ausschließlich mit den angegebenen Mitteln angefertigt. Hiermit erkläre ich an Eides statt, dass ich die vorliegende Arbeit selbstständig verfasst und nur unter Zuhilfenahme der ausgewiesenen Quellen und Hilfsmittel angefertigt habe. Beiträge von Kooperationspartnern wurden explizit gekennzeichnet.

Referees

Dr. Kerstin G. Blank (MPIKG, Germany)

Prof. Dr. John Dunlop (Universität Salzburg, Austria)

Prof. Dr. Aránzazu del Campo Bécares (Leibniz Institut für neue Materialien, Germany)

Potsdam, January 2019

Melis Goktas

List of Publications and Contributions

The following papers have been published within the scope of this work:

Goktas, M., Blank, K.G. (2017). Molecular force sensors: from fundamental concepts toward applications in cell biology. *Adv. Mater. Interfaces* 4(1), 1600441. DOI: 10.1002/admi.201600441

Goktas, M., Luo, C., Sullan, R.M.A., Bergues-Pupo, A.E., Lipowsky, R. Vila Verde, A., Blank, K.G. (2018). Molecular mechanics of coiled coils loaded in the shear geometry. *Chem. Sci.* 9(20), 4610-4621. DOI: 10.1039/C8SC01037D

Zusammenfassung

Kraft spielt eine fundamentale Rolle bei der Regulation von biologischen Prozessen. Zellen messen mechanische Eigenschaften der extrazellulären Matrix und benutzen diese Information zur Regulierung ihrer Funktion. Dazu werden im Zytoskelett Kräfte generiert und auf extrazelluläre Rezeptor-Ligand Wechselwirkungen übertragen. Obwohl der grundlegende Einfluss von mechanischen Signalen für das Zellschicksal eindeutig belegt ist, sind die auf molekularer Ebene wirkenden Kräfte kaum bekannt. Zur Messung dieser Kräfte wurden verschiedene molekulare Kraftsensoren entwickelt, die ein mechanisches Inputsignal aufnehmen und in einen optischen Output (Fluoreszenz) umwandeln.

Diese Arbeit etabliert einen neuen Kraftsensor-Baustein, der die mechanischen Eigenschaften der extrazellulären Matrix nachbildet. Dieser Baustein basiert auf natürlichen Matrixproteinen, sogenannten coiled coils (CCs), die α-helikale Strukturen im Zytoskelett und der Matrix formen. Eine Serie an CC-Heterodimeren wurde konzipiert und mittels Einzelmolekül-Kraftspektroskopie und Molekulardynamik-Simulationen charakterisiert. Es wurde gezeigt, dass eine anliegende Scherkraft die Entfaltung der helikalen Struktur induziert. Die mechanische Stabilität (Separation der CC Helices) wird von der CC Länge und der Zuggeschwindigkeit bestimmt. Im Folgenden wurden 2 CCs unterschiedlicher Länge als Kraftsensoren verwendet, um die Adhäsionskräfte von Fibroblasten und Endothelzellen zu untersuchen. Diese Kraftsensoren deuten an, dass diese Zelltypen unterschiedlich starke Kräften generieren und mittels Integrin-Rezeptoren auf einen extrazellulären Liganden (RGD-Peptid) übertragen.

Dieses neue CC-basierte Sensordesign ist ein leistungsstarkes Werkzeug zur Betrachtung zellulärer Kraftwahrnehmungsprozesse auf molekularer Ebene, das neue Erkenntnisse über die involvierten Mechanismen und Kräfte an der Zell-Matrix-Schnittstelle ermöglicht. Darüber hinaus wird dieses Sensordesign auch Anwendung bei der Entwicklung mechanisch kontrollierter Biomaterialien finden. Dazu können mechanisch charakterisierte, und mit einem Fluoreszenzreporter versehene, CCs in Hydrogele eingefügt werden. Dies erlaubt die Untersuchung der Zusammenhänge zwischen molekularer und makroskopischer Mechanik und eröffnet neue Möglichkeiten zur Diskriminierung von lokalen und globalen Faktoren, die die zelluläre Antwort auf mechanische Signale bestimmen.

Abstract

Force plays a fundamental role in the regulation of biological processes. Cells can sense the mechanical properties of the extracellular matrix (ECM) by applying forces and transmitting mechanical signals. They further use mechanical information for regulating a wide range of cellular functions, including adhesion, migration, proliferation, as well as differentiation and apoptosis. Mechanical forces are generated in the cytoskeleton and are transmitted to the ECM through membrane receptors that specifically bind to ECM components. Even though it is well understood that mechanical signals play a crucial role in directing cell fate, surprisingly little is known about the range of forces that define cell-ECM interactions at the molecular level.

Recently, synthetic molecular force sensor (MFS) designs have been established for measuring the molecular forces acting at the cell-ECM interface. MFSs detect the traction forces generated by cells and convert this mechanical input into an optical readout. They are composed of calibrated mechanoresponsive building blocks and are usually equipped with a fluorescence reporter system. When the MFS experiences a force that exceeds a given threshold value, its response is converted into an optical readout signal. Up to date, many different MFS designs have been introduced and successfully used for measuring forces involved in the adhesion of mammalian cells. These MFSs utilize different molecular building blocks, such as double-stranded deoxyribonucleic acid (dsDNA) molecules, DNA hairpins and synthetic polymers like polyethylene glycol (PEG). These currently available MFS designs lack ECM mimicking properties.

In this work, I introduce a new MFS building block for cell biology applications, derived from the natural ECM. It combines mechanical tunability with the ability to mimic the native cellular microenvironment. Inspired by structural ECM proteins with load bearing function, this new MFS design utilizes coiled coil (CC)-forming peptides. CCs are involved in structural and mechanical tasks in the cellular microenvironment and many of the key protein components of the cytoskeleton and the ECM contain CC structures. The well-known folding motif of CC structures, an easy synthesis via solid phase methods and the many roles CCs play in biological processes have inspired studies to use CCs as tunable model systems for protein design and assembly. All these properties, especially their tunable sequence and natural mechanical function, make CCs ideal candidates as building blocks for MFSs. In this work, a series of heterodimeric CCs were designed, characterized and further used as molecular building blocks for establishing a novel, next-generation MFS prototype.

A mechanistic molecular understanding of their structural response to mechanical load is essential for revealing the sequence-structure-mechanics relationships of CCs and for utilizing them as tunable molecular building blocks for MFSs. Here, synthetic heterodimeric CCs of different length were loaded in shear geometry and their mechanical response was investigated using a combination of atomic force microscope (AFM)-based single-molecule force spectroscopy (SMFS) and steered molecular dynamics (SMD) simulations. SMFS showed that the rupture forces of short heterodimeric CCs (3-5 heptads) lie in the range of 20-50 pN, depending on CC length, pulling geometry and the applied loading rate ($\mathrm{d}F/\mathrm{d}t$). Upon shearing, an initial rise in the force, followed by a force plateau and ultimately strand separation was observed in SMD simulations. A detailed structural analysis revealed that CCs show a complex structural response to shear load. This response depends on the loading rate and involves helix uncoiling, uncoiling-assisted sliding in the direction of the applied force and uncoiling-assisted dissociation perpendicular to the force axis.

The application potential of these mechanically characterized CCs as building block for MFSs has been tested in 2D cell culture applications with the goal of determining the threshold force for cell adhesion. Fully calibrated, 4- to 5-heptad long, CC motifs (CC-A_4B_4 and CC-A_5B_5) were used for functionalizing glass surfaces with MFSs. 3T3 fibroblasts and endothelial cells carrying mutations in a signaling pathway linked to cell adhesion and mechanotransduction processes were used as model systems for time-dependent adhesion experiments. A_5B_5-MFS efficiently supported cell attachment to the functionalized glass surfaces for both cell types, while A_4B_4-MFS failed to maintain attachment of 3T3 fibroblasts after the first 2 hours of initial cell adhesion. This difference in cell adhesion behavior demonstrates that the magnitude of cell-ECM forces varies depending on the cell type and further supports the application potential of CCs as mechanoresponsive and tunable molecular building blocks for the development of next-generation protein-based MFSs.

This novel CC-based MFS design is expected to provide a powerful new tool for observing cellular mechanosensing processes at the molecular level and to deliver new insights into the mechanisms and forces involved. This MFS design, utilizing mechanically tunable CC building blocks, will not only allow for measuring the molecular forces acting at the cell-ECM interface, but also yield a new platform for the development of mechanically controlled materials for a large number of biological and medical applications. CC-based MFSs can easily be integrated into 3D biomaterial systems (e.g., hydrogels) to develop synthetic ECM mimics. Using mechanically characterized CC building blocks for materials design will further allow for establishing a direct relationship between molecular and bulk mechanics. The possibility of equipping CC-based MFSs with fluorophores and integrating them into 3D hydrogels as mechanosensitive and tunable crosslinks will also open up new opportunities for investigating the simultaneous effect of local and global material properties on cellular mechanosensing.

Table of Contents

List of Figures

List of Tables

List of Abbreviations

AFM	Atomic force microscope
Ala	Alanine
Asn	Asparagine
ATP	Adenosine triphospate
AuNP	Gold nanoparticle
BFP	Biomembrane force probe
BSA	Bovine serum albumin
CC	Coiled coil
CD	Circular dichroism
CHO	Chinese hamster ovary
Cys	Cysteine
DFA	Differential force assay
DMEM	Dulbecco's modified eagle medium
dsDNA	Double-stranded deoxyribonucleic acid
ECM	Extracellular matrix
EDTA	Ethylenediaminetetraacetic acid
EGF	Epidermal growth factor
F	Force
FA	Focal adhesion
FCS	Fetal calf serum
FJC	Freely-jointed chain
FRET	Förster resonance energy transfer
Gln	Glutamine
Glu	Glutamic acid
h	hour

h	hydrophobic
Ile	Isoleucine
k_B	Boltzmann constant
k_{off}	force-free dissociation constant
L	contour length
Leu	Leucine
Met	Methionine
MFS	Molecular force sensor
min	minute
mPAD	Micropillar array detector
M1	Mutant 1
M2	Mutant 2
NHS	*N*-hydroxy succinimide
NSET	Nanometal surface energy transfer
p	polar
PAA	Polyacrylamide
PBS	Phosphate buffered saline
PEG	Polyethylene glycol
Phe	Phenylalanine
QI	Quantitative imaging
Rho	Rhodamine
SCFS	Single-cell force spectroscopy
SEM	Standard error of the mean
SMD	Steered molecular dynamics
SMFS	Single-molecule force spectroscopy
SPPS	Solid phase peptide synthesis
T	Temperature

T_m	Melting temperature
TCP	Tissue culture plate
TFM	Traction force microscopy
TGT	Tension gauge tether
Trp	Tryptophan
Tyr	Tyrosine
TSP	Thrombospondin
UV	Ultra-violet
Val	Valine
WLC	Worm-like chain
WT	Wild type
z	persistence length
ΔG	Gibbs free energy
Δx	Potential width

1 Introduction

1.1 Molecular force sensors for detecting cellular traction forces

The molecular machinery of cells utilizes a large variety of intracellular mechanosensors and actuators to regulate biological processes such as cell movement, cell division, vesicle transport, as well as membrane shaping and fusion [1]. In addition to this intracellular machinery, receptor-ligand interactions between cells and their extracellular microenvironment play a fundamental role in the mechanoregulation of cellular processes [2, 3]. Cells probe the physical properties of their surroundings, constantly transmitting mechanical signals (i.e., forces) from the extracellular to the intracellular microenvironment and vice versa. These mechanical signals are translated into biochemical activity and initiate specific intracellular signaling pathways in a process termed mechanotransduction.

Receptor-mediated force transduction takes part in the regulation of many cellular processes such as adhesion [4], migration [5], proliferation [6], as well as differentiation [7]. This is a clear indication that force transduction across the cell-ECM interface is crucial for the regulation of cell fate via mechanosensing and mechanotransduction cascades. Therefore, a detailed molecular understanding of the highly complex and sophisticated response of cells to the different physical parameters of their microenvironment is required. A large number of proteins involved in mechanotransduction cascades have been identified in recent years [8] and it is now widely accepted that these mechanosensitive proteins undergo force-induced conformational changes altering their molecular activity [2, 3, 9]. However, little is known about the magnitude of the molecular forces that are required to trigger these conformational changes.

Detailed knowledge of the molecular forces is crucially important for elucidating the structure-function-mechanics relationships of mechanoresponsive proteins and for understanding the progression of diseases that involve malfunctioning mechanotransduction cascades, such as arteriosclerosis, osteoporosis, muscular dystrophies, developmental disorders and cancer [10]. Molecular force sensors will allow for the direct measurement of molecular forces acting between cell-surface receptors and their extracellular ligands and provide information of fundamental importance for understanding molecular disease mechanisms. Knowledge obtained from these measurements will further provide crucial input for designing synthetic materials that mimic the physical properties of the natural ECM.

1.1.1 Mechanosensing and mechanotransduction at the cell-ECM interface

The key mechanical link between the structural components of the intracellular and extracellular microenvironment is established via focal adhesions (FAs), which are composed of hierarchical assemblies of mechanosensitive proteins. FAs are complex protein assemblies that directly connect the cytoskeleton with the ECM. Within these complex assemblies, integrin receptors mediate the primary cell-ECM interaction [9, 11-13]. Integrins are heterodimeric transmembrane proteins that are composed of one α and one β subunit. In mammals, 18 different α and β subunits are found, which can assemble into 24 different heterodimers [14]. The β subunit mediates the attachment of the integrin heterodimer to the actin cytoskeleton via adaptor proteins, while the α subunit determines the specificity of cell-ECM interactions [15]. Depending on this specificity, integrins can mediate cell attachment to a large variety of ECM proteins, including fibronectin, collagen, laminin and vitronectin [16, 17].

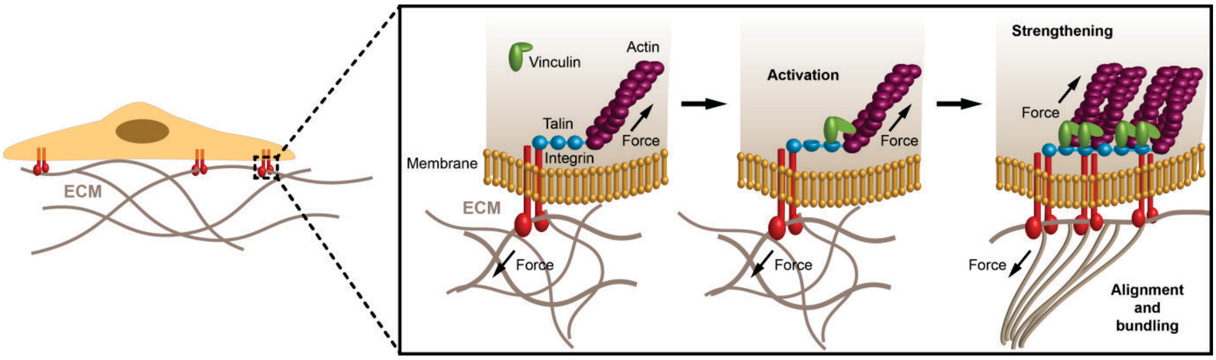

Figure 1. Mechanotransduction at focal adhesions. Cells adhere to ECM ligands *via* integrin receptors. Following integrin activation, talin is recruited at the intracellular side where it forms the link between integrins and the actin cytoskeleton. After the formation of integrin-actin bridges, forces transmitted via the FAs cause conformational changes in talin. Mechanically stretched talin exposes cryptic binding sites for vinculin, a protein that provides additional links to actin. This critical step ensures stress fiber formation and FA strengthening. (Reproduced with permission from ref. [18], copyright © WILEY-VCH Verlag GmbH & Co.)

FAs are highly dynamic and complex structures that form in several sequential steps (**Figure 1**) [9, 12, 13]. On the intracellular side, they are composed of different structural and signaling proteins including the adaptor proteins that built the bridge between the integrin receptors and the actin cytoskeleton. Talin is the primary adaptor protein that establishes a direct connection between integrin receptors and the actin cytoskeleton through its multiple binding domains for F-actin and β-integrin molecules. In addition to talin, other adaptor proteins such as α-actinin, filamin and tensin also take part in the formation of the link between integrins and the actin cytoskeleton. During cell attachment, integrin receptors found in cellular lamellipodia at the leading edge of the cell bind to their ECM ligands at the FA sites. This primary integrin-ligand interaction initiates the recruitment of adaptor proteins to FA sites to form the primary integrin-actin bridges. After the formation of integrin-actin bridges, the forces generated due to actin retrograde flow cause conformational changes in talin. These forces result in the exposure of cryptic binding sites for vinculin, which is a protein that provides additional links to actin [19]. During these processes, initial FAs get translocated toward the lamellum of the cell and myosin gets engaged with actin, followed by the formation of actin stress fibers [20]. At this stage, acto-myosin contractility becomes the main source of forces acting on the matured FAs and several other mechanosensitive molecules become activated to provide further recruitment of proteins to strengthen the actin-FA linkage.

All these mechanical linkages within FA sites are highly dynamic and reversible in the presence of force, resulting in a high turnover of FA proteins. The forces transmitted via these dynamic protein assemblies are heterogeneous and the dynamics of these structures further affects the nature and stoichiometry of the FA-actin linkage. Bonds may break and reform under force, thereby redirecting the force transduction pathway within the FA protein assembly. This dynamic organization becomes even more complicated considering the different binding affinities of different integrin subclasses and the catch bond behavior (i.e., bonds that strengthen under load) of some integrins [21, 22]. Altogether, the dynamic nature and the complex interplay of FA proteins in mechanotransduction cascades clearly indicates the need for the direct measurement of forces involved in this process at the molecular level.

1.1.2 Experimental techniques for determining cellular traction forces

Methods for directly measuring the forces involved in cell-ECM adhesion were developed long before the complex architecture of FAs was revealed by proteomic studies. Most frequently used approaches for measuring cell adhesion forces can be divided into 3 main categories: single-cell force spectroscopy (SCFS), single-molecule force spectroscopy (SMFS) and traction force microscopy (TFM).

1.1.2.1 Single-cell force spectroscopy

The first SCFS method used for measuring the forces involved in cell adhesion was the biomembrane force probe (BFP) technique which allows for picking up and immobilizing an individual cell via the suction at a micropipette tip [23, 24]. The immobilized cell is then brought into contact with another cell that is adhered to a substrate or a surface functionalized with cell adhesive ligands. Once the adhesive contacts have formed, the micropipette is retracted from the surface and the adhesion force of the cell is determined. Using the BFP technique, forces ranging from 10^{-2} to 100 pN can be detected [24]. Subsequently, other SCFS techniques, covering different detectable force ranges, such as optical tweezers (~0.1-100 pN force range) and magnetic tweezers (~10^{-3}-10^{4} pN force range) have been developed for measuring the adhesion forces [25-29]. Among all the methods developed for measuring cell adhesion forces, atomic force microscopy (AFM)-based SCFS is the most versatile technique due to its large detectable force range (~10-10^{6} pN) and superior spatial (~1 nm to 100 µm) and temporal (~0.1 s to >10 min) resolution [30-33]. AFM-based SCFS further provides the possibility for measuring the forces acting between biomolecules in a dynamic fashion, which allows the user to investigate the effect of the force loading rate (i.e., loading rate $\dot{F} = \mathrm{d}F/\mathrm{d}t$) on the strength of biomolecular interactions.

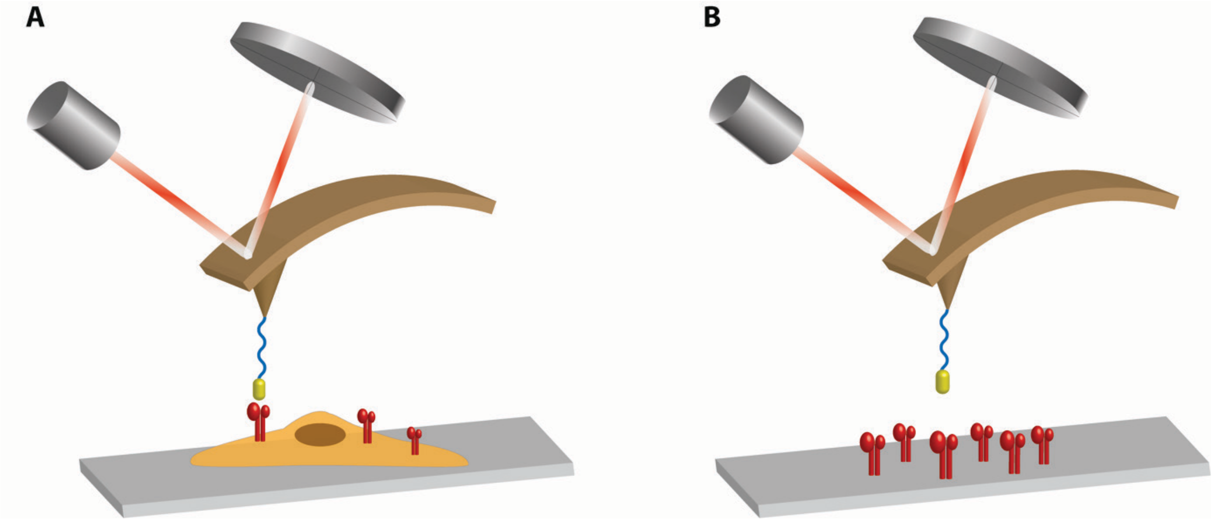

Figure 2. Force spectroscopy approaches for quantifying the forces involved in cell adhesion. A) Single-cell force spectroscopy (SCFS). The tip of the AFM cantilever is functionalized with cell-adhesive ligands. To measure the adhesion forces, the tip is brought into contact with a cell that adheres to a substrate. B) Single-molecule force spectroscopy (SMFS). The rupture forces between purified cell-surface receptors and small cell-adhesive ligands or full-length ECM proteins are measured. (Reproduced with permission from ref. [18], copyright © WILEY-VCH Verlag GmbH & Co.)

AFM-based SCFS allows for two different configurations. The cell, which is adhered to a substrate, can be probed with an AFM cantilever modified with cell-adhesive ligands (**Figure 2A**). Cell-adhesive ligands are immobilized to the cantilever tip directly or via a micrometer-sized bead that is attached to a tip-less cantilever. Even though the implementation of the setup is very straightforward, this configuration has several disadvantages. During long measurements, contamination of the tip with cellular material is one problem. Also, the local density of cell-surface receptors might vary due to differences in the spreading area and the polarization of the cells adhered to the surfaces [32]. Another configuration, where a single cell is attached to the AFM cantilever, provides a solution to this problem. The cell is then brought into contact with another cell adhered to a substrate or with a surface functionalized with cell-adhesive ligands [34]. This strategy eliminates possible differences in the local density of cell-surface receptors since the spreading of the cell on the cantilever is prevented by the size and shape of the cantilever. The system can be further improved when using locally functionalized cantilevers that direct cell adhesion to pre-defined areas [32].

The common drawback for all SCFS techniques is that the number and the specificity of the receptor-ligand interactions between the cell and the substrate cannot be fully controlled. It is known that different integrin receptors can bind to the same ligand and full-length ECM proteins carry more than one integrin-binding site. As a result, rather complicated force-distance curves containing many overlapping rupture events are observed. Although this brings a challenge to interpreting the force signature, it is often possible to extract the desired information via comparing force-distance curves measured in the absence and presence of specific blocking agents, such as freely soluble ligands that block a target receptor.

Many research groups used SCFS with different cell lines for investigating the adhesion forces between a variety of ligands and integrin receptors. Examples include collagen I and collagen IV coated surfaces used for measuring the adhesion forces to $\alpha_2\beta_1$ integrins of Chinese hamster ovary (CHO) cells [35], fibronectin coated substrates for probing the adhesion to $\alpha_5\beta_1$ integrins of K562 cells [36], as well as vascular cell adhesion molecule-1 (VCAM-1) functionalized substrates for probing the adhesion forces to $\alpha_4\beta_1$ integrins of U937 cells [37]. These studies demonstrated a broad range of rupture forces from 20 to 140 pN for different integrin-ligand interactions, depending on the loading rate (**Table 1**).

Table 1. Integrin-ligand forces measured using single-cell force spectroscopy (SCFS) and single-molecule force spectroscopy (SMFS). (Reproduced with permission from ref. [18], copyright © WILEY-VCH Verlag GmbH & Co.)

Method	Integrin	Ligand	Force Range [pN]	Loading Rate Range [pN s^{-1}]	References
SCFS	$\alpha_2\beta_1$	Collagen	38-90	180-8800	[35]
SCFS	$\alpha_5\beta_1$	Fibronectin	40-140	230-13000	[36]
SCFS	$\alpha_4\beta_1$	VCAM-1	20-125	100-10000	[37]
SMFS	$\alpha_4\beta_1$	VCAM-1	40-175	150-100000	[37]
SMFS	$\alpha_5\beta_1$	GRGDSP	15-109	1000-305000	[38]
SMFS	$\alpha_{IIb}\beta_1$	Fibrinogen	20-150	160-16000	[39]

1.1.2.2 Single-molecule force spectroscopy

Receptor-ligand forces can also be determined using AFM-based SMFS when the purified receptors or ligands are immobilized to the AFM cantilever and probed against their binding partners immobilized to the substrate (**Figure 2B**). After approaching the surface with the tip of the cantilever and allowing the receptor-ligand interaction to form, the tip is retracted from the surface. At a certain point, the receptor-ligand interaction ruptures and the rupture force is extracted from the force-distance curves. Using purified receptors has the advantage of providing more control over receptor density, thus facilitating well-defined single-molecule experiments.

A large number of different integrin-ligand forces have been measured with AFM-based SMFS, such as $\alpha_5\beta_1$-GRDGSP peptide (a short cell-adhesive peptide sequence derived from the ECM protein fibronectin) [38], $\alpha_4\beta_1$-VCAM-1 [37], and $\alpha_{IIb}\beta_3$-fibrinogen [39]. Similar to SCFS measurements, SMFS measurements also yielded a range of rupture forces (up to ~175 pN) for different integrin-ligand interactions, depending on the loading rate applied (**Table 1**). The main drawback of SMFS is that cell surface receptors are isolated from their natural microenvironment. Considering the complexity of FAs and their dynamic regulation, it appears likely that the isolation of cell surface receptors drastically affects their conformation and function [40].

Even though SCFS and SMFS are highly powerful techniques that allow for quantitatively probing receptor-ligand interactions, several limitations exist for these techniques. Both SCFS and SMFS are time consuming and, as mentioned above, the measurement conditions are highly artificial and do not resemble the natural cellular microenvironment. Even in the case of live cell measurements, only a small area on the cell surface is probed and the cell is exposed to the ligands locally. In reality, cells are exposed to ligands and mechanical stimuli in three dimensions within their natural microenvironment. Also, the possible contact time during the measurements is limited to a few minutes due to the thermal drift of the AFM cantilever. Therefore, only the initial steps of FA formation can be investigated. In addition, AFM-based force spectroscopy techniques lack the possibility of real-time observation of FA structures and stress fibers, so that efforts have been undertaken to combine AFM with fluorescence microscopy for directly observing these dynamic structures during force measurements [28, 29, 41, 42].

1.1.2.3 Traction force microscopy

TFM is a powerful method that fulfils the need of observing cells optically while they mechanically interact with their environment [43]. In TFM, cells are seeded on an elastic substrate that mimics the mechanical properties of the native ECM (**Figure 3A**). Simply, when cells apply forces to their surroundings, the elastic substrate is deformed and the magnitude, localization and direction of the deformation can be monitored as an optical readout. Using a substrate with well-characterized elastic properties, cell-applied forces can be directly calculated. The system can be integrated with fluorescence microscopy techniques, which allow for visualizing FA size, shape and dynamics at the cell-substrate interface in real-time.

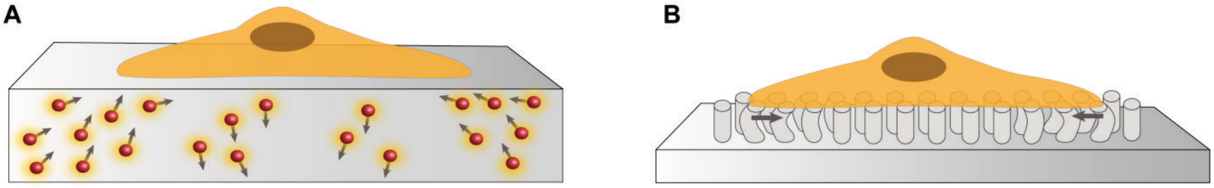

Figure 3. Traction force microscopy. A) Cells are grown on flat elastic substrates that contain fluorescent beads embedded inside the material. Cellular traction forces are measured as a function of bead displacement. B) Micropillar array detectors utilize 3D structures that display micrometer-sized elastic pillars. Cells grown on these 3D structures, form FAs on top of these pillars. Cellular traction forces lead to pillar bending. (Reproduced with permission from ref. [18], copyright © WILEY-VCH Verlag GmbH & Co.)

In the first TFM experiments, keratocytes were cultured on a crosslinked silicone film containing fluorescent latex beads inside, and the bead movement was observed to detect material deformation resulting from cell-applied forces [44, 45]. In later studies, the silicone substrate was replaced with other elastic substrates such as polyacrylamide (PAA) hydrogels, which were also easier to functionalize with cell-adhesive ligands [46]. Bead imaging was combined with the detection of fluorescently tagged FA proteins to allow for correlating cellular structures with the localization of traction forces [47]. Observing the bead displacement in the substrate in 3D, it was possible to determine both in-plane (x,y) and normal (z) forces [48, 49]. The results showed that 3T3 fibroblasts exert forces of ~2000-5000 pN μm^{-2} at FA sites and can apply force in all three dimensions equally [48].

One key advantage of the PAA system is the possibility of tuning the substrate stiffness within the physiologically relevant range (0.1-100 kPa) [50], which allows for investigating mechanotransduction and cell behavior as a function of substrate stiffness [7]. However, it is important to keep in mind that PAA gels with different stiffness do possess different crosslinking density and, consequently, different pore size. It is therefore difficult to discriminate how these local differences affect cell behavior. Also, unlike native ECM, synthetic materials such as silicone and PAA are not cleavable by cellular proteases. Recently, using enzyme (e.g., matrix metalloprotease) cleavable matrices, it has been shown that remodeling of the ECM affects the traction force profile of cells [51]. Enzyme cleavable matrices support high degrees of cell spreading, which in turn results in high traction forces. In contrast, synthetic matrices that restrict cell-mediated remodeling exhibit low degrees of spreading correlated with low traction forces.

Another TFM based technique used for altering the elastic properties of the substrate utilizes micrometer-sized pillars (**Figure 3B**) and is, therefore, termed micropillar array detector (mPAD). The pillars are made from polymethlysiloxane (PDMS) and the pillar height and diameter is altered to vary the mechanical properties [52]. To provide cell attachment, the top of the pillars is generally coated with cell adhesive ligands, such as fibronectin and collagen. mPAD studies, combined with visualizing the fluorescently labeled FA protein vinculin, showed a positive correlation between traction forces and the size of FAs. Further studies demonstrated that traction forces also correlated with the substrate stiffness, depending on the size of an FA (~2-5 μm^2). REF52 fibroblasts generated forces varying from ~3000 up to ~80000 pN within a stiffness range of 4700-80000 pN μm^{-2} [53].

Overall, TFM is a powerful technique that allows for visualizing cellular structures, so that the size of FAs can be determined together with the traction forces applied via these structures. However, it should be considered that the spatial resolution for TFM techniques is limited to a few micrometers and many receptor-ligand interactions contribute to the measured displacement in the visualized area. As a consequence, traction forces measured by TFM are usually in the nanonewton range, which is significantly higher than the receptor ligand forces determined with SCFS and SMFS [35-39]. Attempts have been made to estimate the number of integrins within one FA and the force acting on a single integrin molecule. The calculated forces range from 1 to 30 pN [3, 54], indicating that such estimates are unreliable due to the highly dynamic nature of FAs where only a small fraction of integrins might be actively involved in force transduction. The values obtained from SCFS and SMFS span a range of ~15-175 pN, suggesting that the traction forces exerted by individual integrins are higher than the forces estimated from TFM experiments. These discrepancies between different techniques clearly highlight the need for new tools that allow for measuring single-molecular forces directly at the cell-ECM interface.

1.1.2.4 Molecular force sensors for measuring the cell-ECM forces

The ideal MFS design for measuring cell-ECM forces should combine the advantages of previously mentioned SCFS, SMFS and TFM techniques. Single-molecule force resolution is required and the new design should allow the observation of many individual interactions simultaneously using a fluorescence readout for real-time monitoring. To investigate the feasibility of replacing a macroscopic force sensor with a single molecule, an early prototype of molecular force sensors, a so-called differential force assay (DFA), was developed where two different dsDNA molecules were directly compared with each other in a molecular tug-of-war [55]. In this technique, the AFM cantilever was replaced with a short DNA duplex as a model MFS, as DNA is mechanically well-characterized and the rupture forces of dsDNA molecules can be tuned easily depending on their length, sequence and pulling geometry.

This early prototype has set the stage for the implementation of DNA-based MFSs that are now becoming more and more widely used for materials science and cell biology applications. Different MFS designs have been implemented for measuring molecular forces on the extracellular side, specifically with the goal of investigating the interaction between transmembrane receptors (e.g., integrins) and their ligands. These designs are extremely powerful for determining the forces acting at the cell-ECM interface with single-molecule resolution.

Currently available MFS designs can be divided in two main categories: (i) Two-component MFSs that break once the applied force exceeds a threshold value (**Figure 4A**). (ii) One-component MFSs that utilize a mechanoresponsive probe, such as a DNA hairpin or a polymeric entropic spring, such as poly(ethylene glycol) (PEG). The probe is inserted into a chain of molecules under tension, where it acts as a spring and reports on the force acting along the chain when extended (**Figure 4B**).

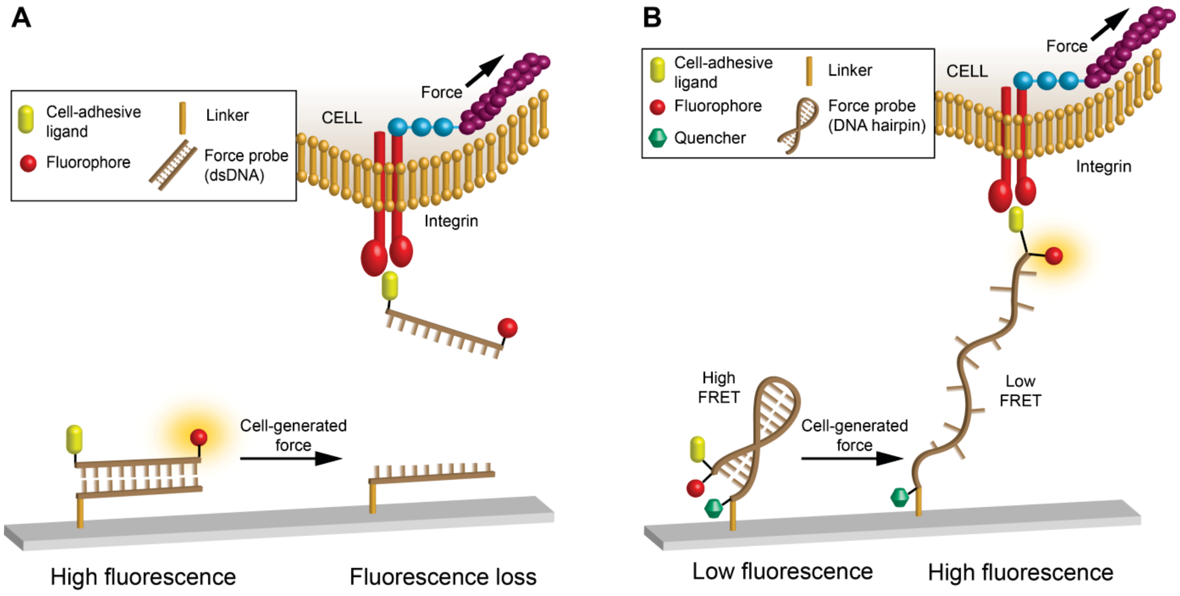

Figure 4. Design principles of molecular force sensors. A) Two-component molecular force sensor utilizing dsDNA oligonucleotides. One oligonucleotide is coupled to the substrate and the second oligonucleotide is functionalized with a cell-adhesive ligand (e.g., a RGD peptide). The DNA duplex ruptures when the cells apply sufficient force via their transmembrane receptors (e.g., integrins). The oligonucleotide that carries the cell-adhesive ligand is further labeled with a fluorophore. Cell-generated forces break the DNA duplex, leading to the detachment of the cells together with the fluorescently labeled probe and causing a loss of fluorescence from the substrate. B) One-component molecular force sensor utilizing a mechanoresponsive probe (e.g., a DNA hairpin). The hairpin is functionalized with a fluorophore and a quencher that undergo FRET. When sufficient force is applied, the DNA hairpin opens, leading to a change in the FRET efficiency and, consequently, an increase in donor fluorescence. (Reproduced with permission from ref. [18], copyright © WILEY-VCH Verlag GmbH & Co.)

1.1.2.4.1 Two-component molecular force sensors for extracellular force measurements

Extracellular MFS designs generally use mechanoresponsive probes that are immobilized on a substrate surface and are equipped with a cell-adhesive ligand to promote the specific interaction of cells with the MFSs (**Figure 4**). When the cells are seeded on top of the MFS-functionalized surface, cell surface receptors (e.g., integrins) get engaged with the cell-adhesive ligands and cells start applying forces on the MFSs. In the case of two-component MFSs, the sensor breaks once the applied force exceeds the stability limit of the MFS (**Figure 4A**). If cells are able to apply forces larger than the stability limit of the two-component MFS, they break the MFS and, thereby, cannot attach to the surface. In contrast, when the mechanical stability of the MFS is sufficiently high, cells are able to adhere to the surface and grow. Using this experimental strategy, the threshold force required for cell attachment can directly be tested.

In the first proof-of-concept experiments, dsDNA-based MFSs were used to determine the threshold force of cell attachment determined by the interaction between $\alpha_V\beta_3$ integrins and cRGDfk ligands. For these experiments, a set of nine different MFSs with varying threshold forces, termed as 'tension gauge tethers' (TGTs), was designed [56]. Making use of the fact that the rupture force of dsDNA depends on the pulling geometry (shear vs. unzip) [55], the rupture force of the TGT sensors was tuned in the range from ~12 to 56 pN. The pulling geometry was determined by simply attaching the dsDNA molecules to the substrate at different positions. The estimated threshold force in the unzip geometry was ~12 pN, while it was ~56 pN in the shear geometry [56, 57]. Intermediate attachment positions were used to cover the force range between these two extremes. Using this strategy, it was shown that the TGTs were required to possess a stability limit of at least ~40 pN to promote the attachment of CHO-K1 cells and 3T3 fibroblasts to the substrate.

In this first design, cell attachment and growth was the only readout parameter for monitoring the interaction between the cells and TGTs. Later on, this MFS design was further equipped with a fluorophore, which was coupled to the sensor component that carries the cell-adhesive ligand [58, 59]. When the cells break the sensor, the component carrying the fluorophore was detached from the surface, consequently resulting in a loss of the fluorescence signal at the sites where the cells interacted with the TGTs. When using TGTs with a low mechanical stability (<40 pN), the TGTs were ruptured everywhere on the surface where cells interacted with the sensor, leading to a complete fluorescence loss. Cell attachment to the substrate was also prohibited, as TGTs with low mechanical stability do not provide the possibility for forming stable FAs. When the TGT with a predicted stability of 56 pN was used, fluorescence loss (rupture of the sensors) was limited to designated areas, which were correlated with the position of FAs and stress fibers. These results suggest that the formation of FAs and stress fibers requires at least 56 pN of tension across the integrin-ligand bonds [58]. Further examinations using the mixture of these two TGTs (12 and 56 pN rupture force), showed that cells did not attach to the substrate functionalized only with "low force" TGT, while they were able to attach if a very small amount of "high force" TGT was co-immobilized on the surface [59]. One or two "high force'' TGT per cell were sufficient to promote cell attachment, indicating that cells are extremely sensitive while probing the mechanical properties of their surroundings.

This two-component MFS design quickly became a highly versatile toolbox for measuring tension acting between cell-surface receptors and their ligands at the cell-ECM interface. The TGT design has now been used in many studies to characterize the mechanics of different cell surface receptors including the Notch receptor [56, 60], B-cell [61] and T-cell receptors [62], as well as E-cadherin and P-selectin [63]. The TGT sensor can also be used for studying mechanotransduction mechanisms in more detail. It is still not fully clear how global material properties (e.g., material stiffness) and local mechanical stimuli (e.g., locally acting forces) contribute to the regulation of cell fate [7, 64, 65]. Due to their design principle, two-component MFSs restrict the maximum force that can be exerted through a single cell-surface receptor so that they can allow for dissecting these different contributions. In addition, they can be used as building blocks to alter the nature of the linkage between the cell-adhesive ligands and the substrate.

A few attempts have been made to utilize the two-component MFS design for obtaining a material platform that allows for investigating the simultaneous effect of global and local material properties on cellular behavior. In a series of elegant studies, TGTs were immobilized on the glass surface via PEG spacers with different lengths [66] or alternatively coupled to PAA [66] or alginate gels [67] of different stiffness. Even though these experiments suggested the involvement of both global and local factors for the regulation of cell behavior, further investigation is still needed for an elaborate understanding of mechanoregulation at the cell-ECM interface.

1.1.2.4.2 One-component molecular force sensors for extracellular force measurements

One-component MFS designs utilize a mechanosensitive module that responds to an applied force in a well-defined way (**Figure 4B**). Similar to two-component designs, the mechanosensitive module is functionalized with a cell-adhesive ligand and immobilized to a substrate surface via a functional group. The module is further functionalized with two chromophores forming a Förster resonance energy transfer (FRET) pair and the FRET efficiency is used as a reporter to read out the mechanically induced extension of the module.

The one-component MFS designs developed to date include synthetic polymers, DNA hairpins or peptide and protein structures as mechanosensitive modules (**Table 2**). PEG is the most frequently used synthetic polymer, as its force-extension behavior can be described with well-known polymer models, such as the worm-like chain (WLC) or freely-jointed chain (FJC) models. This well-characterized force-extension behavior allows for the direct correlation of the FRET efficient with the force acting on the MFS. For PEG chains of different length (PEG_{12}-PEG_{80}), a dynamic force range of ~1-30 pN was predicted, using the WLC model and considering the Förster radius of the FRET pair [68-70].

Table 2. Technical properties of one-component molecular force sensors used for extracellular force measurements. FRET: Förster resonance energy transfer; NSET: nanometal surface energy transfer; WLC: worm-like chain; BFP: biomembrane force probe; AFM: atomic force microscope. (Reproduced with permission from ref. [18], copyright © WILEY-VCH Verlag GmbH & Co.)

Sensor	Mechanism	Force Range	Sensor Calibration	Signal	Readout	References
PEG_n	Entropic spring	~1-30 pN	Calculated from WLC model	FRET	Analog (continuous)	[68, 69, 71]
PEG_n	Entropic spring	~1-30 pN	Calculated from WLC model	NSET	Analog (continuous)	[70, 72]
flagelliform	Linear spring	~1-7 pN	SMFS (optical tweezers)	FRET	Analog (continuous)	[73-75]
DNA hairpin	Unfolding	~6-17 pN	SMFS (optical tweezers)	FRET	Digital (ON-OFF)	[76]
DNA hairpin	Unfolding	~5-16 pN	SMFS (BFP)	FRET	Digital (ON-OFF)	[62, 77]
Titin	Unfolding	~80-200 pN	SMFS (AFM)	NSET	Kinetic	[78]

In a first set of proof-of-principle experiments, the PEG module was functionalized with epidermal growth factor (EGF) and a threshold force of 4 pN was detected for the EGF-receptor interaction [68]. The same design was later used to determine forces acting between $\alpha_V\beta_3$ integrins and several integrin ligands, including the cRGDfk peptide [62, 69-71]. In these experiments, the streptavidin-biotin interaction was used to immobilize the MFS to the substrate surface and it was observed that the tension acting across a single integrin bond can dissociate the streptavidin-biotin interaction over extended periods of time [69]. This result indicated that integrin-ligand interactions can withstand extremely high forces, in agreement with the results obtained with two-component MFSs, and SCFC/SMFS experiments [63]. These results highlight that non-covalent interactions should be avoided for the immobilization of MFSs to the substrate surfaces.

To avoid this stability problem, a new system was developed where PEG-based MFSs were attached to gold nanoparticles (AuNPs), utilizing a strong thiol-gold bond [70, 72]. This design yielded integrin-ligand forces around 1 pN, contradicting the previous results [72]. Later on, the effect of ligand spacing was investigated with the same system by adjusting the distance between AuNPs [70]. When a ligand spacing of 100 nm was used, the formation of FAs and stress fibers was prevented and integrin-ligand forces were limited to a maximum value of 3 pN, while the forces reached up to values of ~6-12 pN along with the formation of FAs and stress fibers for a ligand spacing of 50 nm. However, the values obtained were still relatively small, not agreeing the earlier results. One possible explanation for these contradictory results is that the number of MFSs that are actually mechanically engaged to an integrin receptor is unknown and the fluorescence signal, on the other hand, is obtained from the ensemble of all available sensor molecules (mechanically coupled and non-coupled). In addition, the force distribution across different integrin-ligand bonds might be heterogeneous, so that only a small number of integrins may be applying high forces causing the observed rupture of strong non-covalent bonds, while the other integrin molecules exert smaller forces [59].

One solution to the ensemble averaging problem can be the use of digital one-component MFSs that show only one ON (high FRET) and one OFF (low FRET) state. With this design, the relative fraction of sensors in either state can directly be calculated from the FRET efficiency of the ensemble. DNA hairpins are good candidates for digital MFSs, as the hairpin is short enough and unfolds cooperatively when mechanically stretched [76, 77, 79]. They provide the possibility of tuning the force threshold (~5-16 pN; corresponding to the force where 50% of the hairpins unfolded in a force clamp experiment) in a sequence dependent manner. Even though the results obtained with the DNA hairpin design indicated that the integrin-ligand forces were highly dynamic and heterogeneous and that a significant number of integrin receptors exert forces exceeding the threshold of the sensor, it was not possible to determine the highest possible integrin-ligand forces due to the limited force range of the hairpins. Later on, an alternative digital one-component MFS design based on the mechanically well-characterized titin protein was developed to overcome the force range limitation [78]. AFM-based SMFS measurements showed that titin unfolds under forces ranging from ~150 to 300 pN, thereby covering a high force range [80, 81]. Results obtained with the titin-based MFSs indicated that integrins are indeed able to apply such high forces.

Even though the currently available results appear to be inconsistent, still a number of conclusions can be drawn. Ensemble and time-averaged forces obtained with MFSs and a number of other methods yield integrin-ligand forces ranging from <1 up to ~10 pN [3]. Nevertheless, a small number of integrin in the population might still experience much higher forces. It is also important to keep in mind that the forces experienced by single integrin receptors may vary over time. Considering the knowledge that we have so far, a crucial next step is clearly to investigate these heterogeneities and to unravel the functional relevance of low force and high force integrin-ligand interactions. One should also keep in mind that the inconsistencies between the absolute force values determined with different MFSs may also be a result of the different calibration methods and the lack of knowledge of the biologically relevant loading rates.

1.2 General considerations for the design and application of molecular force sensors

Many different MFS designs have been introduced in recent years. They have evolved into powerful tools for investigating the molecular mechanisms of mechanotransduction and for providing novel information about FA mechanics. Even though several critical principles, including functional, spatial, and temporal FA heterogeneities, have been established, the measurement of absolute force values has remained a challenge. In many cases, the dynamic force range that MFSs can cover is rather small and the sensor molecules have either not been calibrated or different methods have been used for their calibration. Last but not least, most of the available designs lack ECM mimicking properties.

1.2.1 Force range and molecular force sensor calibration

Currently available MFS designs utilize a large variety of different building blocks. However, the majority of MFSs can only report forces up to ~60 pN, except for the recently introduced titin-based MFS with a force range between 150-300 pN [78-80]. Yet, there is no MFS design available, which can fill the gap or span the complete force range accessible to biological systems. Extending the force range of a certain MFS design is not an easy task. For example, the rupture force of dsDNA-based MFSs shows a plateau at ~65 pN, where the DNA molecule undergoes an unfolding transition (B-S transition) [82, 83]. It is not possible to increase the rupture force of DNA above this plateau value when the natural bases A, T, C, and G are used. Possible strategies can be the substitution of individual pyrimidine bases with their propynyl derivatives [84] or the utilization of a peptide nucleic acid (PNA) backbone [85, 86].

The second issue to address is the calibration of the mechanical response of MFSs and correlating it to the fluorescence signal. For many MFS designs, an accurate sensor calibration has not yet been obtained. The mechanical response of some MFS building blocks, including PEG and dsDNA, is well-characterized. The force extension behavior of PEG is described with the WLC model, which allows a straightforward calibration of the optical signal versus the applied force. Also for dsDNA mechanically loaded in the shear geometry, a model treating the dsDNA molecule as a 2D ladder has been proposed [57]. The predictions of this model have later been verified experimentally with magnetic tweezers experiments [87]. The mechanical stability of the two-component dsDNA-based MFSs (i.e., TGTs) is calculated with this model [56]. A more accurate 3D model has later been developed [88]. Even though, the values calculated for shear and unzip geometries were confirmed by the improved 3D model, the results yielded significantly lower values for the intermediate geometries used in the TGT experiments. These discrepancies highlight that an experimental calibration is essential even for mechanically well-characterized molecules. Despite these efforts to obtain a semi-quantitative calibration, it also needs to be considered that the force values given have been determined with different methods. For example, the values calculated for the TGT refer to the minimum force that needs to be applied to rupture the dsDNA sensors within 2 seconds [56, 87], while the forces given for the DNA hairpin sensors represent the equilibrium force [76, 77], i.e. the force where 50% of the MFS molecules are in the unfolded state. These differences in the calibration methods, restrains the possibility to directly compare the obtained force values.

1.2.2 Stability and kinetics of bonds under force

Efforts to use experimentally calibrated MFSs for determining cellular traction forces need to consider that force is not an intrinsic property of a biomolecular interaction. The forces, which determine the stability of the MFSs and the cell surface receptor-ligand interactions, do not only depend on the free energy (ΔG) of the molecular process (**Figure 5**), but also on the temperature (T) and the rate of the applied force (i.e., the loading rate). According to Bell's model [89], an externally applied force (F) lowers the energy barrier (ΔG) (**Equation 1**), thereby speeding up bond rupture.

$$k(F) = v \cdot e^{\frac{-(\Delta G - F \cdot \Delta x)}{k_B T}} \qquad (1)$$

where $k(F)$ is the rate of the mechanically accelerated reaction, v the attempt frequency, Δx the distance between the ground and the transition state (i.e., the potential width), k_B the Boltzmann constant, and T the temperature.

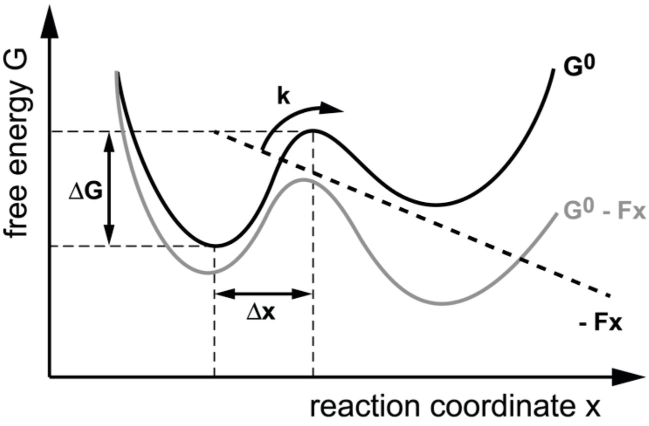

Figure 5. Effect of force on the free energy landscape of a molecular process. Assuming a simple two-state system, the applied force F lowers the energy barrier ΔG of the reaction by the amount $-Fx$ so that the molecular process is accelerated. (Reproduced with permission from ref. [18], copyright © WILEY-VCH Verlag GmbH & Co.)

Since crossing the energy barrier is a thermally assisted process, bond rupture depends on the force loading rate ($\dot{F}$ = dF/dt) [90, 91]. According to the Bell-Evans model, the force (F) depends on the loading rate (**Equation 2**) as follows;

$$F = \frac{k_B T}{\Delta X} \cdot ln\left(\frac{\dot{F}}{k_{off}} \cdot \frac{\Delta x}{k_B T}\right) \qquad (2)$$

where k_{off} represents the rate of the reaction at zero force.

The loading rate, acting on individual integrin receptors in FAs, is not known and it might dynamically change over time. Also, the timescale that individual molecules experience the load may vary. One can assume that the loading rates in biological systems would be far below the experimental loading rate range generally used in SMFS. One possible way of avoiding this issue could be using MFSs that do not show any or a very weak loading rate dependence. To fulfill this situation, the mechanically induced reaction should be reversible within the experimentally accessible timescale or in other terms, the backward rate of the reaction should be faster than the rate of force application. It is possible to observe this kind of near-equilibrium behavior for the extension of PEG and unzipping of dsDNA [92], as these reactions occur at low forces where many small molecular rearrangements occur sequentially.

On the other hand, processes occurring at higher forces usually involve high energy barriers and the reaction is generally not reversible during the experimentally relevant timescale. Considering that most mechanically induced processes show strong loading rate dependence, a full calibration at different loading rates is crucially important for a newly developed MFS. Measuring the rupture forces over a broad loading rate range further allows for the extraction of the kinetic parameters such the rate of the reaction at zero force (k_{off}) and the potential width (Δx) as described by the Bell-Evans model. For a fully calibrated system, the rupture force can then be calculated for any loading rate and temperature relevant for the biological system of interest, using the Bell-Evans equation (**Equation 2**).

Overall, due to the limitations in the force range of currently available MFSs and the lack of knowledge of the loading rate relevant for biological systems, variations in the obtained force values are expected. To overcome these limitations, a new fully calibrated MFS design that can cover a broad force range is required. A new MFS design, fulfilling these criteria, can allow for a more detailed investigation of spatial and temporal heterogeneities in the forces acting on integrin receptors at the single-molecule level.

1.2.3 What makes a good force sensor for biological applications?

Over the past decade, many MFS designs have been introduced for determining cell-applied forces in different biologically relevant systems. The subsequent evolution of their design has made them more versatile and increased their utility in recent years. Yet, the available design strategies still have to integrate several additional considerations. Specific recommendations for adequately helping the development of improved MFSs for determining cell-ECM forces need to include aspects such as

- compatibility with the cellular microenvironment by mimicking native ECM,
- having load bearing properties (i.e., mechanical function) in Nature,
- allowing for the straightforward introduction of cell-adhesive ligands,
- possibility of integration into 3D biomaterials (e.g., hydrogels) for developing advanced mechanosensitive ECM model systems.

Considering currently available designs, DNA-based designs have become the most frequently used MFSs. They have been proven to function well for biological applications where different types of cells were utilized. Even though DNA molecules are responsive to mechanobiochemical regulation within cells, one should consider that DNA is not naturally found in the ECM, therefore lacking ECM mimicking properties. Whereas DNA may not affect cell responses in *in vitro* experiments on 2D surfaces, it remains an open question if cells will respond to extracellular DNA when grown in 3D cultures. On the long term, when mechanoresponsive ECM mimics may be used *in vivo*, the possibility of an immunogenic response against these DNA building blocks needs to be considered. Another issue to address is that the structural, mechanical response of DNA is rather different when compared to mechanosensitive and mechanoregulated ECM proteins.

DNA is well characterized for its sequence-specific deformability and the effect of these local features has been related to its overall polymeric behavior upon force application [93]. An elastic model of the DNA double helix has been developed, which is based on a description of the degrees of freedom between two neighboring base pairs [94]. This deformability model underpins the elastic response of DNA and also describes passive conformational changes in biological processes, e.g. when proteins bind to DNA. In contrast, natural mechanosensing processes involve active force transduction via integrin receptors. Cells are constantly testing the rigidity of the extracellular microenvironment by pulling and pushing on ECM proteins. These ECM proteins frequently possess an α-helical polypeptide backbone (mainly assembled into left-handed superhelices) with rather different torsion angles and side-chain flexibilities than DNA. These structures are characterized by a large extensibility and high toughness, combined with the possibility of forming higher order oligomerization states and hierarchical fibrillar structural assemblies. Cells thus experience a variety of mechanical properties, arising from the different elastic responses of ECM proteins with different structures, assembly states, mechanical properties and regulatory elements.

New MFS designs should consequently utilize building blocks that mimic the molecular structure and mechanical response of natural ECM proteins as closely as possible. Choosing a protein structure that is derived from the native ECM comes with several attractive features. Such structures provide simple strategies for introducing cell-adhesive ligands derived from ECM proteins, such as the short peptide sequence RGD [95]. Short peptides are easily inserted into protein-based molecular building blocks as the polypeptide backbone can simply be extended. On the other hand, attaching cell-adhesive ligands to the nucleotide backbone of DNA-based systems, requires additional coupling and purification steps. Most importantly, ECM-derived MFS building blocks match the mechanical properties of ECM proteins, thereby providing a better mimic of natural mechanosensing and force transduction processes at the cell-ECM interface.

1.3 Coiled coils as molecular force sensors for the extracellular matrix

This work introduces the α-helical coiled coil (CC) protein folding motif as a new MFS building block. The CC structure represents the most abundant oligomerization motif found in the structure of ECM proteins with mechanical function. It is thus proposed that the CC is an ideal candidate for testing its potential as a molecular building block for the development of next-generation protein-based MFSs.

1.3.1 Coiled coils as mechanosensitive elements of the cellular microenvironment

The CC folding motif is a typical structural feature of many different intracellular and extracellular proteins. CCs occur in a wide range of proteins with different functions, such as short leucine zippers that drive the dimerization of transcription factors or longer chains that form fibrous cytoskeleton and ECM proteins [96]. CCs thus mediate highly specific and stable protein-protein interactions and define cellular organization and morphology as well as tissue stability and extensibility. Moreover, CCs play a more active role in a number of molecular motor proteins. CCs are among the most thermodynamically stable protein folding motifs known, owing to the regularity and repetitive nature of packing interactions.

Many dimeric CC domains can be found in cytoskeletal proteins, such as intermediate filaments, molecular motor proteins, filamin and spectrins. In eukaryotic cells, the cytoskeleton is composed of three different filamentous networks: the actin-myosin system, microtubules (with dynein and kinesin molecular motors) and intermediate filaments. The interconnected network formed by these filamentous protein structures provides the mechanical integrity of the cell. Intermediate filaments are composed of different CC-forming proteins, which self-assemble into filaments with a diameter of approximately 10 nm. Intermediate filament proteins are classified into subgroups based on their structure and homology. Keratins form the two largest classes of intermediate filament proteins; type I (acidic) and type II (basic), while vimentin, desmin, glial fibrillary acidic protein and peripherin are classified as type III [97]. Type IV and type V classes are formed by neurofilaments and lamins, respectively [97]. The assembly of intermediate filaments is driven by interactions between specific types of intermediate filament proteins. For example, keratin filaments - where the CC domain was first discovered - are composed of the assemblies of acidic (type I) and basic (type II) polypeptides. At first, the two polypeptides wrap around each other to form the CC dimer. Dimers then associate in a staggered fashion to form tetramers, tetramers form protofilaments and, finally, 8 protofilaments wind around each other in a ropelike structure to form the keratin filament. This unique assembly of CC domains provides high tensile strength and toughness to intermediate filaments, characteristics which are highly essential for maintaining the structural integrity of the cellular structure [98].

The molecular motor proteins myosin, kinesin and dynein directly interact with the cytoskeleton and are responsible for force generation inside cells [99]. The catalytic activity of motor proteins involves a complex mechanism, including different conformational changes mostly driven by ATP hydrolysis. Motion is directly linked to force production and involves conformational changes of CC domains [100-102]. Conventional myosin (myosin II) forms the framework of the muscle thick filament shaft via the specific packing of its CC domains [103]. Whereas myosin II is responsible for muscle contraction, unconventional myosins possess several functions in cells, including the organization of F-actin, transportation of vesicles and organelles along actin fibers, formation of mitotic spindles during cell division, regulation of cell motility via retrograde flow and membrane extrusion, as well as tension sensing [104]. The other motor proteins, kinesin and dynein, also carry CC domains. Kinesin, which moves with a 8.2 nm step size without dissociating, contains a dimeric CC in its neck domain. It has been observed that the CC structure unwinds during the conformational cycle, thereby providing a specific mechanism regulating kinesin motility [103]. The CC domain in dynein is arranged as an antiparallel CC stalk, which functions as a mechanical force transducer from the head domain to the microtubule binding site [102].

In addition to these cytoskeletal proteins, also the ECM is very rich in oligomeric proteins, many of which contain CC domains. These domains associate with high rates to produce very stable structures and form the large ECM network. CC domains found in the structure of ECM proteins are predominantly trimeric. Examples include matrilins [105], tenascins [106], laminins [107] and some types of thrombospondins (TSP-1 and TSP-2) [108]. Even though less frequent, five-stranded CCs are also found in the structure of TSP-3, TSP-4 and TSP-5 (also named as cartilage oligomeric matrix protein) [108-110]. CC-based oligomerization offers many advantages, including multivalency, high binding strength and the combined function of different domains within the ECM network.

The CC-containing ECM proteins are involved in many important biological processes. Matrilins bind to other ECM components, such as collagen fibrils, other non-collagenous proteins and aggrecan, thereby acting as modulators of ECM assembly and providing structural integrity to the ECM [111]. Furthermore, they take part in mechanotransduction and cartilage homeostasis [111]. Tenascins play an important role in the regeneration and remodeling of the ECM during wound healing or inflammation [112]. Thrombospondins take part in cell-ECM and cell-cell interactions important for many complex cellular processes, such as angiogenesis, immune responses, wound healing, synaptogenesis and the organization of connective tissue [112]. Laminins, which are composed of heterotrimeric CC domains, are structural components of the ECM with key regulatory functions in cell adhesion, migration, differentiation and proliferation [113].

1.3.2 Coiled coils as molecular building blocks

Approximately 10% of all eukaryotic proteins contain CC domains [114] and these CC-containing proteins play different fundamental roles in many cellular processes. Their critical functional importance combined with the relative simplicity of their α-helical fold have inspired the use of CCs as model systems for studying protein folding and design, with the goal of understanding sequence-structure-function relationships in peptide/protein structures [115, 116].

1.3.2.1 Design principles for coiled coil assembly and stability

Establishing fundamental rules for the rational design of CC structures requires a chemical level of understanding of the CC structural assembly. The current rules of CC design are thus rationalized in terms of the underlying noncovalent forces that direct CC assembly and stability [117].

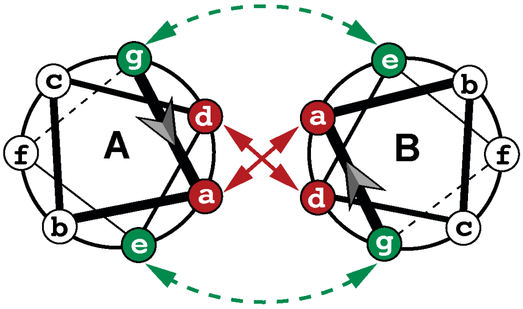

Figure 6. Helical wheel diagram representing the coiled coil structure. Each α-helix is composed of a repetitive pattern of seven amino acids, $(abcdefg)_n$, called a heptad repeat. This specific heptad pattern drives the folding and dimerization of the helices, whereby positions *a* and *d* are often occupied by hydrophobic residues. These residues form the dimer interface, which is key for stabilizing the coiled coil structure. Salt bridges, formed between oppositely charged residues at *e* and *g* positions, contribute additional stability. The solvent-exposed residues *b*, *c* and *f* are more variable, but are crucial for the stability of the individual α-helices. (Reproduced with permission from ref. [118], copyright © Royal Society of Chemistry.)

The key driving force for CC assembly is the formation of hydrophobic interactions. The heptad repeat sequence of CCs is characterized by an alternating pattern of hydrophobic (*h*) and polar (*p*) residues in the order of *hpphppp*. When folded into an α-helix, this primary sequence positions the hydrophobic residues on one face of the α-helix and exposes the polar residues on the other. This simple arrangement drives the helices to associate via their hydrophobic interfaces and to fold into a superhelical structure. The nature of the residues occupying the hydrophobic and polar positions further influences oligomerization state, helix orientation, partner selection and the stability of CC assemblies. The *hpphppp* pattern is usually denoted as *abcdefg*, whereby the *a* and *d* positions are assigned to the hydrophobic residues, as seen in the helical wheel diagram shown in **Figure 6**. In the case of natural CCs, the *a* and *d* positions are often occupied by aliphatic hydrophobic residues (Ala, Ile, Leu, Met and Val), rather than amino acids with aromatic hydrophobic side chains (Phe, Trp and Tyr) [119, 120]. The type and combination of the amino acids occupying the *a* and *d* positions play a critical role in determining the oligomerization state of the CC structure. In particular, the combination of Leu at *d* positions with Ile or Val at *a* positions favors dimers, while Ile or Val occupying the *d* positions favors tetramer formation. On the other hand, the occurrence of Ile or Leu both at *a* and *d* position triggers trimer formation.

In addition to these hydrophobic residues, also polar residues can be found at *a* and *d* positions in natural CCs in a highly conserved form [121, 122]. For example, in the GCN4-p1 Leu zipper sequence, position 16 is occupied by a polar Asn residue, which is buried within the hydrophobic core. It forms a hydrogen bond with the corresponding Asn residue of the neighboring helix. Studies based on the GCN4-p1 model and its Asn16Val mutant revealed that the polar Asn pair may play a number of different roles [123]. Replacement of the Asn residue with a hydrophobic Val resulted in a significant increase of CC stability, accompanied by a loss in oligomerization specificity. The Asn16Val mutant formed mixtures of different oligomers, while the initial sequence only formed dimers. These results suggested that the local hydrophilic region created by polar residues in the hydrophobic interface does not only destabilize the target structure. More importantly, it also prevents the formation of alternative structures, such as out-of-register helical arrangements or thermodynamically weak homodimers. The incorporation of polar residues to the hydrophobic interface can therefore be utilized as a simple design strategy to tune the stability of the CC resulting structure and specify dimer formation.

Even though the hydrophobic core interactions are sufficient to stabilize and maintain the CC assembly, the residues occupying the *e* and *g* positions also contribute to CC assembly, stability and partner selection. As first demonstrated for the natural tropomyosin CC, forming a parallel heterodimer, attractive or repulsive ionic interactions may occur between the amino acid residues found at *e* and *g* positions [124]. In the structure of a parallel CC dimer, the *g* position of one helix is brought into close proximity with the *e* position of a successive heptad repeat of the second helix. This facilitates electrostatic interactions between oppositely charged residues (**Figure 6**). Studies performed on the Fos-Jun oncoprotein heterodimer provided a possible explanation for the partner selection based on these electrostatic interactions [125, 126]. The Fos α-helix is very acidic due to the presence of acidic amino acids at *e* and *g* positions with a negative net charge of -5, while the Jun α-helix has a positive net charge of +2 at neutral pH. Repulsive interactions between residues of the same charge destabilize the formation of Fos and Jun homodimers, while attractive ionic forces favor the formation of a Fos-Jun heterodimer. Based on this knowledge, the second basic rule of CC design is placing oppositely charged residues, such as positively charged Lys and negatively charged Glu, at the *e* and *g* positions for defining the dimer specificity and for providing further stability via the formation of ionic interactions.

As summarized above, the specificity and stability of CC structures are mainly determined by hydrophobic and electrostatic interactions between the residues occupying the *a*, *d*, *e* and *g* positions. However, the thermodynamic stability can also be affected by the residues occupying the *b*, *c* and *f* positions, which face away from the CC interface and generally do not form interchain interactions. Usually, small, helix-favoring residues such as Ala at *b* and *c* positions are preferred, along with Gln, Tyr or Trp residues at *f* positions for increasing solubility or to add UV-active chromophores for further analysis/characterization purposes [115]. Recent studies have shown that it is possible to introduce additional stability into CC structures when redesigning the surface residues at the *b*, *c*, and *f* positions [127, 128]. Engineering intrachain electrostatic interactions (salt bridges) between *b*, *c* and *f* positions, the local helical propensity can be increased, which in turn results in the stabilization of the entire CC [129].

A large variety of different aspects of CC design have been addressed; however, the majority of these studies focused on elucidating the sequence-structure relationship and the thermodynamic stability of CC structures. As mentioned earlier, many structural and mechanically active proteins found in the cytoskeleton and the ECM possess CC structures [130, 131] and these structures play a fundamental role in a variety of mechanobiochemical processes [130, 132]. CC-based proteins constantly experience force in the cellular microenvironment and can undergo structural changes in response to mechanical tension, which in turn results in the regulation of their function. The widespread occurrence of CC domains in structural and mechanically active proteins is clear evidence that the molecular function of these proteins is crucially dependent not only on the thermodynamic stability of the CC building block, but also on its mechanical stability. Understanding the CC sequence-structure-mechanics relationship is therefore the critical next step to shed light on the role of CCs as mechanoresponsive elements, which will in turn facilitate their use as mechanical building blocks in applications, e.g. for the development of CC-based MFSs.

1.3.2.2 Understanding coiled coil mechanical stability

With the goal of determining the mechanical stability of CCs and shedding light on the molecular response of CC structures to an externally applied force, SMFS and molecular dynamics (MD) simulations were used to investigate a small number of natural proteins containing CC domains such as myosin [133-135], vimentin [136-139] and fibrin [140-142]. When a force is applied parallel to the helical axis, these natural CC structures show a universal, 3-phase response to the external force. Upon stretching, a linear increase in the force is observed (phase I) as a response to the extension of the CC structure against entropic forces and the mechanical loading of the intrahelical hydrogen bonds. Following phase I, a long force plateau (phase II) is observed. The plateau starts at 10-25% strain and arises from the continuous breaking of intrahelical hydrogen bonds and the uncoiling of individual helices at an almost constant force. For the experimentally tested CCs, this plateau region yields forces between 20-60 pN [133-135, 141]. At the end of the plateau phase, the fully uncoiled structure gets stabilized by interstrand hydrogen bonds and a β-sheet structure is formed (α-β transition) in many cases [143]. When the strain exceeds 80%, the force shows a steep rise again (phase III) due to the stretching of the β-sheet structures [144, 145]. As the natural CCs investigated differ in sequence and oligomerization state, this universal behavior suggests that the uncoiling of helices represents a fundamental mechanistic response of CCs to an externally applied force. Full-length proteins were generally used in these experiments, however, and the anchoring point of the protein to the force transducer was not defined. As a result of this non-specific attachment, it is not clear which portions of the CC structure were stretched under the externally applied force. Furthermore, the exact force application geometry is unknown due to the random attachment sites on the CC superhelix [146].

To overcome these limitations, site-specific coupling strategies were used in more recent studies and the mechanical coordinate for the force application was precisely defined. The force was applied to the same terminus of the individual helices of CC dimers, so that the CC structure was mechanically loaded in a so-called ‘unzip’ geometry [138, 147]. Mechanical unzipping of CCs, such as the GCN4 Leu zipper [147, 148] and vimentin [138], revealed that the CC structures unfold at forces between 8-15 pN. Experiments carried out on CCs with different length showed that CC unzipping is characterized by the sequential uncoiling of helical turns and that the unzipping force weakly depends on CC sequence, but not on CC length [147]. When the force was applied at a slow pulling speed, the uncoiling of helical turns was fully reversible, suggesting that CC unfolding and refolding occurs at equilibrium. For the faster pulling speeds, hysteresis was observed at the initial stages of CC refolding, which was assigned to the formation of a helical seed, required before the propagation of helix formation at a high rate [149].

These findings obtained from the stretching of CC structures parallel to the helical axis as well as CC unzipping, can be compared with the well-known overstretching transition and unzipping behavior of dsDNA. The universal 3-phase behavior of CCs upon stretching is highly similar to the overstretching transition of DNA, which is characterized by a plateau force at approximately 65 pN [82, 83]. Furthermore, the unzipping behavior and the unzipping forces (8-15 pN) are highly similar to what has been observed for DNA (~12 pN for a 21-base pair DNA [56]). These similarities in the molecular response of CCs to an externally applied force strongly suggests that CCs may serve as equally powerful and fully characterized nanomechanical building blocks for a variety of applications, including MFSs, where protein-based nanostructures are desired.

1.4 Aims of this work

Cells sense the mechanical properties of their ECM and use this information for regulating a wide range of cellular functions. Mechanical forces are generated in the cytoskeleton and transmitted to the ECM through membrane receptors that specifically bind to ECM proteins. Even though it is well understood that mechanical signals play a crucial role in directing cell fate, surprisingly little is known about the range of forces that define cell-ECM interactions at the molecular level. To fill this critical gap in the mechanobiology field, the development of next-generation molecular force sensors (MFSs) is required.

Within the scope of this work, the potential of heterodimeric CCs to be used as MFSs will be tested. For this purpose, a small library of CCs will be developed and their response to an externally applied shear force will be characterized and compared to known properties of dsDNA-based MFSs. Based on the obtained knowledge, these CC building blocks will be used for the development of a novel, protein-based MFS prototype with the goal of using this next-generation MFS design for the detection of cell-applied forces with single-molecule resolution. Specifically, the goals of this work are:

- The molecular mechanical properties of CCs are poorly understood. To fill this gap, a small library of synthetic heterodimeric CCs will be designed and mechanically characterized in a shear loading geometry. To compare to CC unzipping and the mechanical response of short dsDNA, CC length will be used as the key design parameter. The shortest CC will have a length of 3 heptads, which is close to the thermodynamic stability limit. The CC sequence will be consecutively extended up to 6 heptads, which is the longest CC that can be obtained with solid-phase peptide synthesis. A specific focus will be placed on obtaining a molecular understanding of the sequence-structure-mechanics relationship of CC structures. Furthermore, it will be tested if CC length can be used as a design parameter to obtain tunable mechanical properties, as required for MFS development.

- First data about CC mechanics have been obtained in SMFS studies performed with long, natural CCs (e.g., myosin, fibrin). These studies have shown that CCs possess a similar force extension behavior as DNA; however, a detailed analysis of short, sequence-controlled CCs stretched in a well-defined force application geometry is required before CCs can be used as MFS. For understanding the molecular response of these CCs to an externally applied shear force and for obtaining calibrated MFSs, AFM-based SMFS measurements will be performed to determine the rupture forces of the CCs over a broad range of loading rates. The SMFS measurements will particularly focus on the shear loading geometry. This force application geometry has not yet been used for the experimental characterization of CC structures and is the most attractive geometry for the implementation of MFSs.

- The SMFS experiments will be complemented with steered molecular dynamics (SMD) simulations to obtain insights into the structural response of the CCs studied. Using identical sequences and force application points, these simulations are expected to allow a direct comparison with the experimentally obtained results and allow for unraveling the molecular mechanism leading to CC rupture. The SMD simulations are conducted in collaboration with the Soft Matter Simulations Group of Dr. Ana Vila Verde (Department of Theory & Bio-systems) at the Max Planck Institute of Colloids and Interfaces.

- Using this small library of mechanically fully characterized CC heterodimers, a novel CC-based MFS design will be developed. The application potential of CC structures as molecular building blocks for MFSs will be tested in 2D cell culture applications. For the initial proof-of-concept experiments, 3T3 fibroblasts will be used as a model system with the goal of determining the threshold force for cell adhesion. Additional experiments will be performed with an endothelial cell line as a medically relevant model system. The wild type cell line will be compared to two mutant cell lines, which carry mutations in a signaling pathway with essential function for cell adhesion and mechanotransduction. These mutations are relevant to a vascular disease and mutant cells possess a different cytoskeletal architecture, accompanied by altered adhesion behavior and traction forces. The CC-based MFS design will be used to investigate alterations in the cellular adhesion process and to detect cell-applied forces for this medically-relevant model system. The endothelial cell line used as a model system is obtained from the Group of Prof. Dr. Petra Knaus, Freie Universität Berlin. The targeted proteins and the disease occurring as a result of these mutations are kept confidential, as this part of the work has not been published yet.

Using this novel CC-based MFS design for investigating cell-ECM interactions will yield important new input toward fully understanding cellular mechanosensing processes at the molecular level. In the future, the CC-based MFS prototype established within the scope of this work can be equipped with a fluorescence readout to observe the cell-MFS interaction in real-time. The MFSs can further be incorporated into 3D materials to obtain a full understanding of the crosstalk between altered mechanotransduction pathways and mechanical material (ECM) properties. Ultimately, this novel approach will provide important new insights into molecular mechanisms of disease progression.

2 Results

2.1 Design of heterodimeric coiled coils and experimental setup

The CC library used in this work is based on a set of *de novo* designed parallel heterodimeric CCs, recently introduced by the Woolfson group [115]. The sequences that have been chosen are composed of a highly regular $(IAALXXX)_n$ heptad repeat (**Figure 7A, 21A, S12A**), which has been shown to provide a high thermodynamic stability. The originally designed 4-heptad coiled coil (CC-A_4B_4) has been shown to possess a dissociation constant K_D smaller than 10^{-10} M and a melting temperature T_m above 80ºC. To investigate the effect of sequence length on CC stability, CCs with a length of 3-4 heptad repeats were used. 1 or 2 hydrophobic contacts were consecutively deleted at the C-terminus of the B_4 helix and, subsequently, CC-$A_4B_{3.5}$ and CC-A_4B_3 heterodimers were obtained (**Figure 7A**).

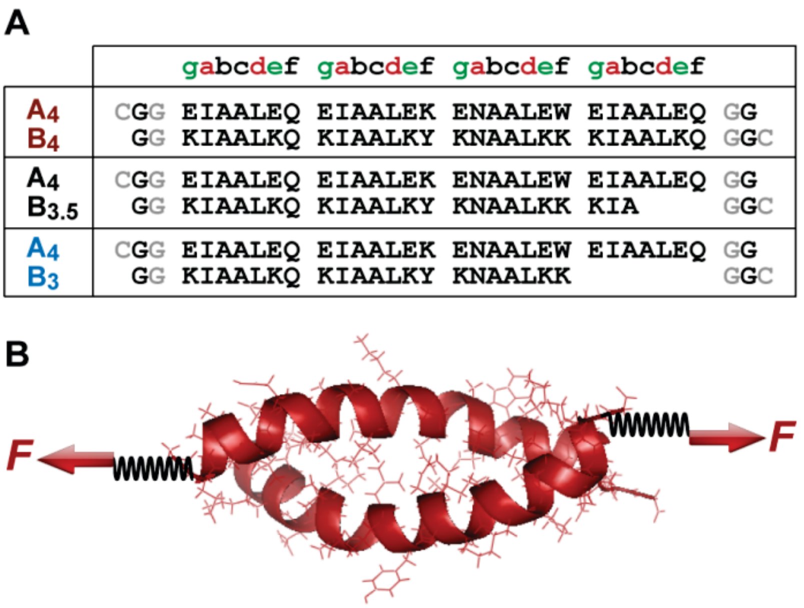

	gabcdef gabcdef gabcdef gabcdef
A4 B4	CGG EIAALEQ EIAALEK ENAALEW EIAALEQ GG GG KIAALKQ KIAALKY KNAALKK KIAALKQ GGC
A4 B3.5	CGG EIAALEQ EIAALEK ENAALEW EIAALEQ GG GG KIAALKQ KIAALKY KNAALKK KIA GGC
A4 B3	CGG EIAALEQ EIAALEK ENAALEW EIAALEQ GG GG KIAALKQ KIAALKY KNAALKK GGC

Figure 7. Setup for SMFS experiments and SMD simulations. A) Sequences of the CC heterodimers used. The sequences used in the SMFS experiments contained two glycine residues at each terminus as well as a cysteine residue for site-specific immobilization. Only one glycine and no cysteine were present in the sequences used for the simulations. B) Geometry of force application for studying the mechanical stability of CCs under shear loading. The force was applied at the N-terminus of peptide A_4 and at the C-termini of peptides B_4, $B_{3.5}$ and B_3, utilizing cysteine residues introduced at the respective termini. In the SMFS experiments, the spring represents a poly(ethylene glycol) linker, which was used to couple the individual peptides to the surface and the AFM cantilever. In the simulations, two virtual harmonic springs were introduced. The distal end of the spring present at the N-terminus of A_4 was fixed, whereas the distal end of the spring attached at the C-terminus of the B peptides was displaced parallel to the helical axis at a constant speed. The initial structure of each CC was produced using Avogadro [150] and equilibrated before the simulations. (Reproduced with permission from ref. [118], copyright © Royal Society of Chemistry.)

This set of sequences has originally been optimized to increase the specificity for heterodimer assembly. Heterospecificity and helix orientation were mostly guided by oppositely charged Lys and Glu residues occupying the *e* and *g* positions of the heptad register. In addition, Ile in the third heptad was replaced by an Asn residue in each helix [117]. Polar Asn residues create a local hydrophilic region in the hydrophobic dimer interface and destabilize undesired structures, such as out-of-register assemblies and thermodynamically weak homodimers. Both CC-forming peptides were handled and immobilized independently, which was essential for setting up the SMFS experiments (**Figure 8**).

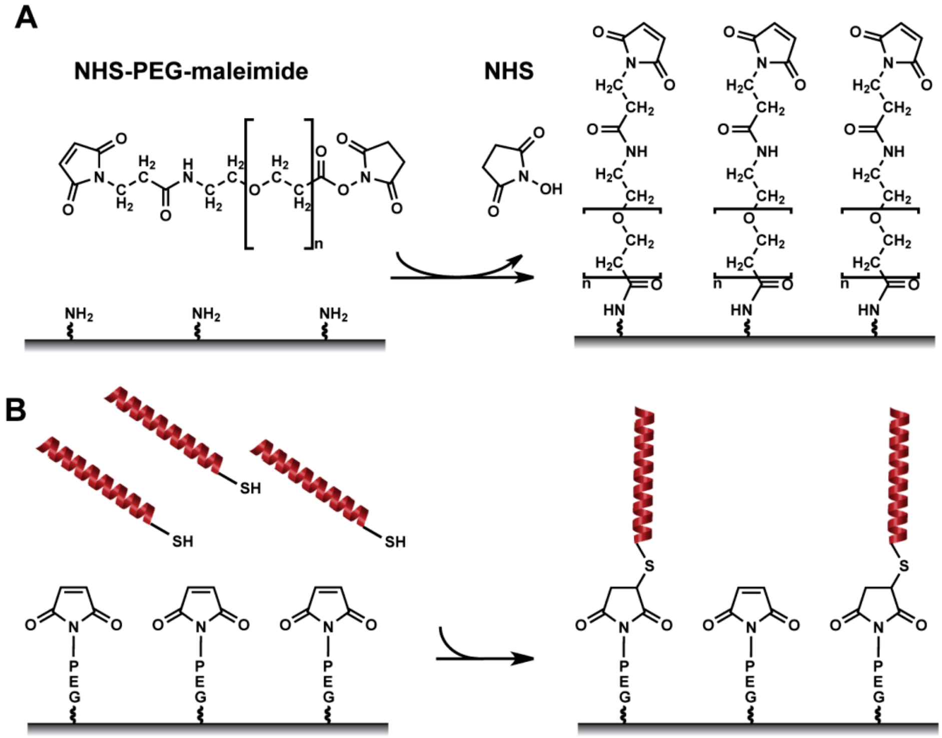

Figure 8. Overview of the immobilization procedure. A) A heterobifunctional NHS-PEG-maleimide spacer was coupled to the amino-modified surfaces through the reaction between amino-groups and *N*-hydroxysuccinimide. B) Then, the peptides were immobilized to the surfaces through the reaction between thiol and maleimide groups.

For mechanically loading the CCs in the shear geometry, the attachment points were located at the opposite termini of the CC-forming peptides (**Figure 7A, B**). The N-terminus of A_4 and the C-termini of the B_4, $B_{3.5}$ and B_3 peptides were chosen as attachment points. CC-$A_4B_{3.5}$ and CC-A_4B_3 possess a C-terminal overhang of the A_4 peptide, which does not fold into a helical structure as it lacks stabilizing interactions with the B peptides. The specific attachment points were chosen to make sure that the applied force directly acts on the folded helical parts of the CC and does not travel through the overhanging part of the A_4 peptide. Cys residues were introduced at the respective termini for the site-specific coupling of each peptide to the AFM cantilever and the glass surface using a previously established protocol (**Figure 8**) [151]. Identical attachment sites were used for the SMD simulations to mimic the experimental setup. The only difference was that only one glycine and no cysteine was present in the sequences used for the SMD simulations (**Figure 7A**).

2.2 Fluorescence analysis to verify the site-specific immobilization of coiled coil heterodimers

Site-specific immobilization and heterospecificity of the designed sequences were verified using a fluorescently labelled A_4 peptide to bind to and detect the surface-immobilized B_4 peptide. For this purpose, the individual peptides were sequentially spotted onto maleimide-functionalized glass slides and the fluorescence signal on the surface was measured (**Figure 9**). Fluorescence is only detected in areas where the B_4 peptide was immobilized, indicating a specific interaction between the two peptides (Rho-A_4/B_4; **Figure 9B**). No significant fluorescence signal was observed for the negative controls: Rho-A_4/A_4 does not show any homodimerization and the addition of excess Cys during the coupling reaction blocked the surface attachment of the Cys-carrying peptides very efficiently (**Figure 9B**). These results show that the interaction between the A_4 and B_4 peptides is indeed heterospecific and that the individual peptides were immobilized to the glass surface site-specifically at their respective Cys-functionalized termini.

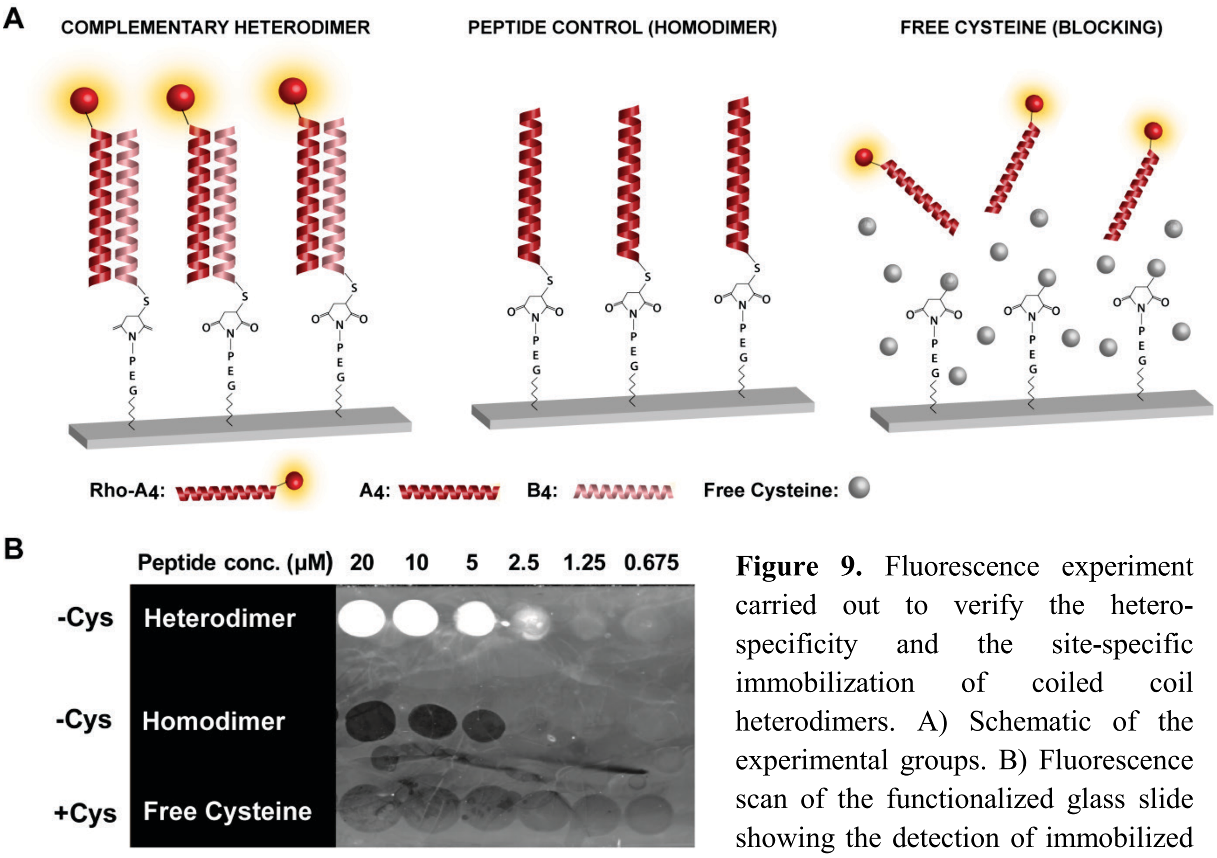

Figure 9. Fluorescence experiment carried out to verify the hetero-specificity and the site-specific immobilization of coiled coil heterodimers. A) Schematic of the experimental groups. B) Fluorescence scan of the functionalized glass slide showing the detection of immobilized coiled coils.

2.3 Secondary structure characterization and thermal stability of coiled coils

The designed CCs and their PEG conjugates were characterized using CD spectroscopy to determine their secondary structure and thermal stability. For all three heterodimers, the CD spectra showed the characteristic minima at 208 nm and 222 nm, indicating α-helical secondary structure (**Figure 10A**). Thermal denaturation experiments revealed a melting temperature above 80ºC for the longest heterodimer, CC-A_4B_4 (**Figure 11A, Table 3**). Truncated sequences, where 1 or 2 hydrophobic contacts were deleted at the C-terminus of the B-helix, possess melting temperatures of 61ºC (CC-$A_4B_{3.5}$) and 39ºC (CC-A_4B_3) (**Figure 11A, Table 3**), showing the expected correlation between the sequence length and thermal stability of the CCs. **Table 3** summarizes the results obtained from the thermal denaturation experiment. In the case of the PEG conjugates, the α-helical secondary structure was preserved (**Figure 10B**) and no significant difference in the thermal stability was observed (**Figure 11B, Table 3**).

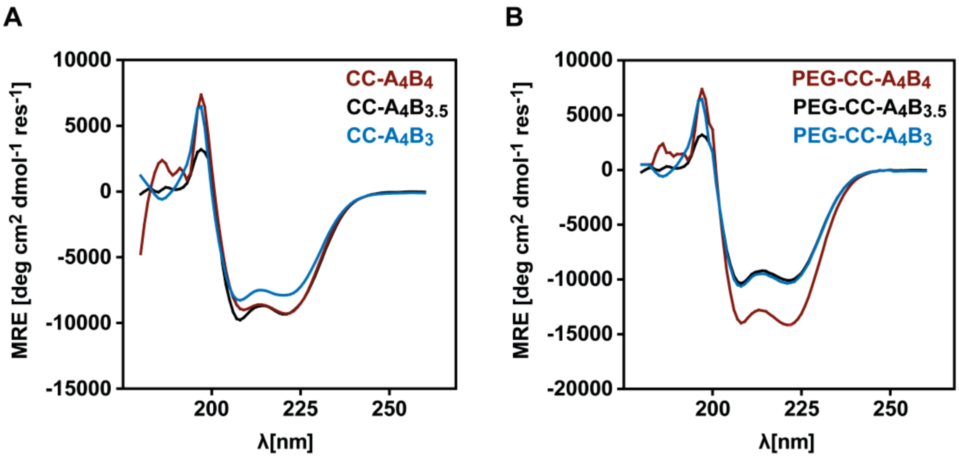

Figure 10. CD spectra of the coiled coils and the corresponding PEG-coiled coil conjugates (20°C). A) Comparison of the CD spectra of the CCs (Cys-free peptides). B) Comparison of the CD spectra of PEG-CC conjugates (10000 g mol^{-1} PEG coupled to the N-terminal Cys of A_4 and the C-terminal Cys of B_4, $B_{3.5}$ and B_3, respectively). All measurements were performed in PBS, using a total peptide concentration of 100 µM.

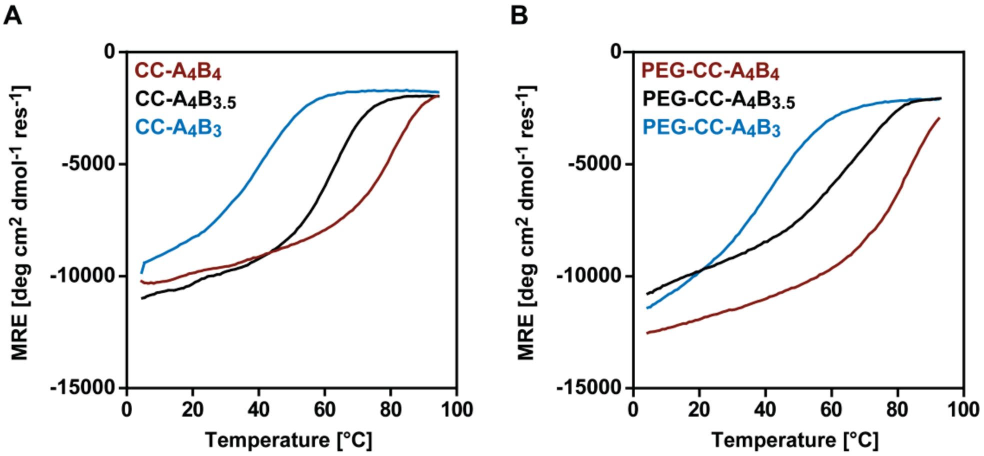

Figure 11. Thermal denaturation curves of the coiled coils and the corresponding PEG-coiled coil conjugates (222 nm). A) Thermal stability of all CCs without terminal Cys residues. B) Thermal stability of the PEG-CC conjugates (10000 g mol^{-1} PEG coupled to the N-terminal Cys of A_4 and the C-terminal Cys of the respective B peptide). All measurements were performed in PBS, using a total peptide concentration of 100 µM.

Table 3. Summary of the melting temperatures for the three different coiled coils (T_{m_CC}) and the corresponding PEG-coiled coil conjugates ($T_{m\_PEG\text{-}CC}$). The data represents the mean ± SEM of 3 independent measurements.

Heterodimer	T_{m_CC} [°C]	$T_{m\_PEG\text{-}CC}$ [°C]
CC-A_4B_4	80.5 ± 0.8	79.9 ± 0.1
CC-$A_4B_{3.5}$	61.0 ± 0.1	64.9 ± 0.3
CC-A_4B_3	39.0 ± 0.1	39.4± 0.3

2.4 Length dependence of coiled coil rupture determined with dynamic single-molecule force spectroscopy

To test the length dependence of CC mechanical stability, AFM-based SMFS was used. The A_4 peptide was immobilized onto an amino-functionalized glass slide via a hetero-bifunctional NHS-PEG-maleimide (MW = 10000 g mol^{-1}) spacer. The B_4, $B_{3.5}$ and B_3 peptides were immobilized to amino-functionalized cantilevers via the same PEG spacer. The surface, functionalized with the A_4 peptide, was then approached with the tip of the cantilever, carrying one of the B peptides, to allow for CC formation (**Figure 12A**). Then, the cantilever was retracted from the surface at a constant speed, thereby loading the CC structure with an increasing force until it ruptured and the cantilever relaxed back to its equilibrium position.

Representative force-extension curves are shown in **Figure 12B**. Clear differences in the rupture force values are observed for the three different CCs, when the rupture force histograms measured at a retract speed of 400 nm s^{-1} are compared (**Figure 13**). Using a Gaussian fit, the most probable rupture force values of 44 pN (CC-A_4B_4), 27 pN (CC-$A_4B_{3.5}$) and 37 pN (CC-A_4B_3) are obtained. These results indicate that the rupture forces for CCs are length-dependent in the shear geometry and are higher than for the unzip geometry, which typically shows rupture forces values around 8-15 pN [138, 147-149].

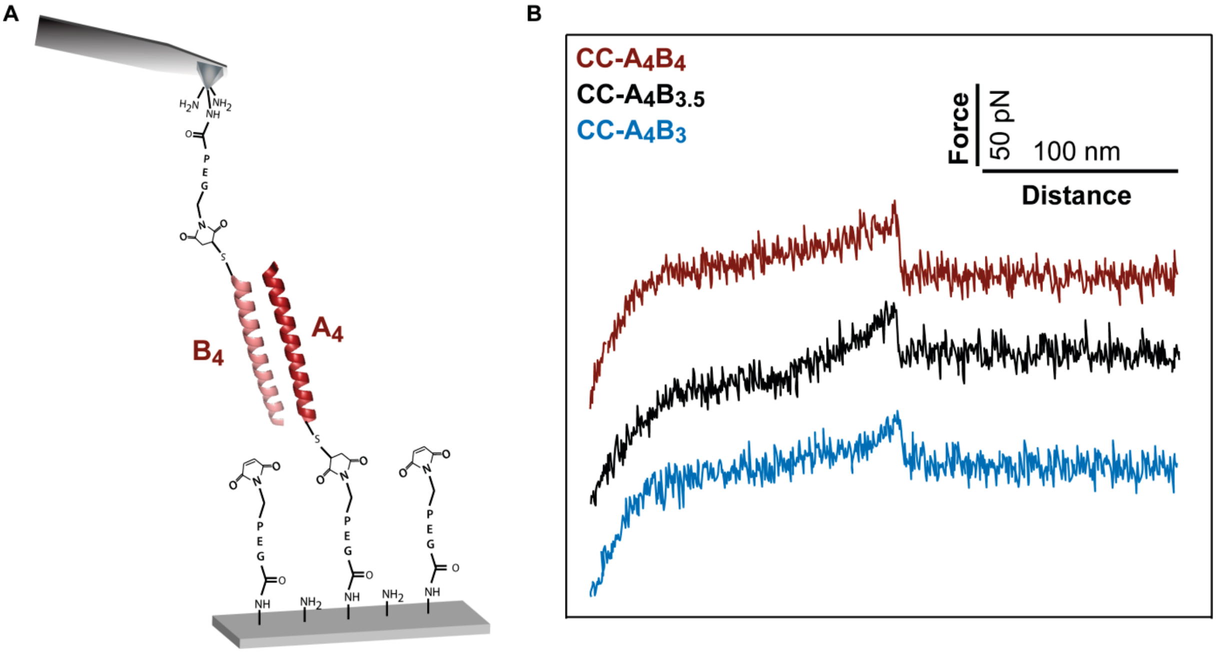

Figure 12. Experimental setup and representative force-extension curves obtained from SMFS measurements. A) The peptide possessing a C-terminal Cys (A_4) was covalently immobilized onto an amino-functionalized glass slide using a heterobifunctional PEG spacer. The same coupling chemistry was used for the immobilization of the peptides possessing N-terminal Cys (B_4, $B_{3.5}$ or B_3) to the cantilever. B) Representative force-extension curves of the different CCs measured with AFM-based SMFS. The force-extension curves show CC rupture recorded at a retract speed of 400 nm s^{-1}. (Reproduced with permission from ref. [118], copyright © Royal Society of Chemistry.)

For each individual CC, dynamic SMFS was performed at six different retract speeds, recording several hundreds of force-extension curves with three different cantilevers (**Figure 14-16, S4-S9**). The most probable rupture forces, obtained at different retract speeds, were plotted against the corresponding most probable loading rates (**Figure 17, Table S2**). Loading rates, $\dot{F} = \mathrm{d}F/\mathrm{d}t$, were determined for every individual force-extension curve (slope k_s of the force-extension curve at the point of rupture, multiplied by the retract speed). The most probable loading rate values were then obtained from the Gaussian fits to their corresponding histograms (**Figure 14-16, S4-S9, Table S2**) and range from ~20 pN s^{-1} to 7500 pN s^{-1}. When plotting the most probable rupture force values, F, against the corresponding ln $\dot{F}$ values, the results demonstrate that the CC rupture forces increase linearly with the logarithm of the loading rates (**Figure 17**), as predicted by the Bell-Evans model [91]. Fitting the data points with the Bell-Evans equation (**Equation 2**), the force-free dissociation rates, $k_{\mathrm{off\_SMFS}}$, and the corresponding potential widths, Δx_{SMFS}, were obtained (**Table 4, S3**). The obtained values show that the longest heterodimer (CC-A_4B_4) possesses the slowest dissociation rate, $k_{\mathrm{off\_SMFS}}$

$= 3.2 \times 10^{-4}$ s^{-1}, and the largest potential width, $\Delta x_{SMFS} = 1.29$ nm, while the shortest CC (CC-A_4B_3) shows a faster dissociation rate, $k_{off\_SMFS} = 6.5 \times 10^{-3}$ s^{-1}, and a smaller potential width, $\Delta x_{SMFS} = 1.03$ nm (**Table 4**).

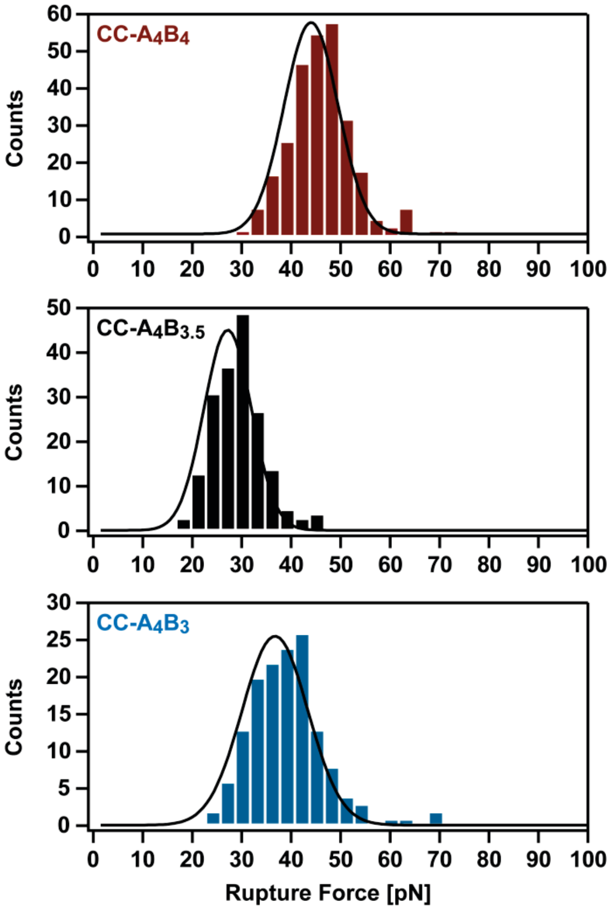

Figure 13. Representative rupture force histograms of the different coiled coils recorded at a retract speed of 400 nm s^{-1}. The rupture force histograms contain 285 rupture events for CC-A_4B_4, 187 rupture events for CC-$A_4B_{3.5}$ and 145 rupture events for CC-A_4B_3, respectively. The black lines represent Gaussian fits to the data. (Reproduced with permission from ref. [118], copyright © Royal Society of Chemistry.)

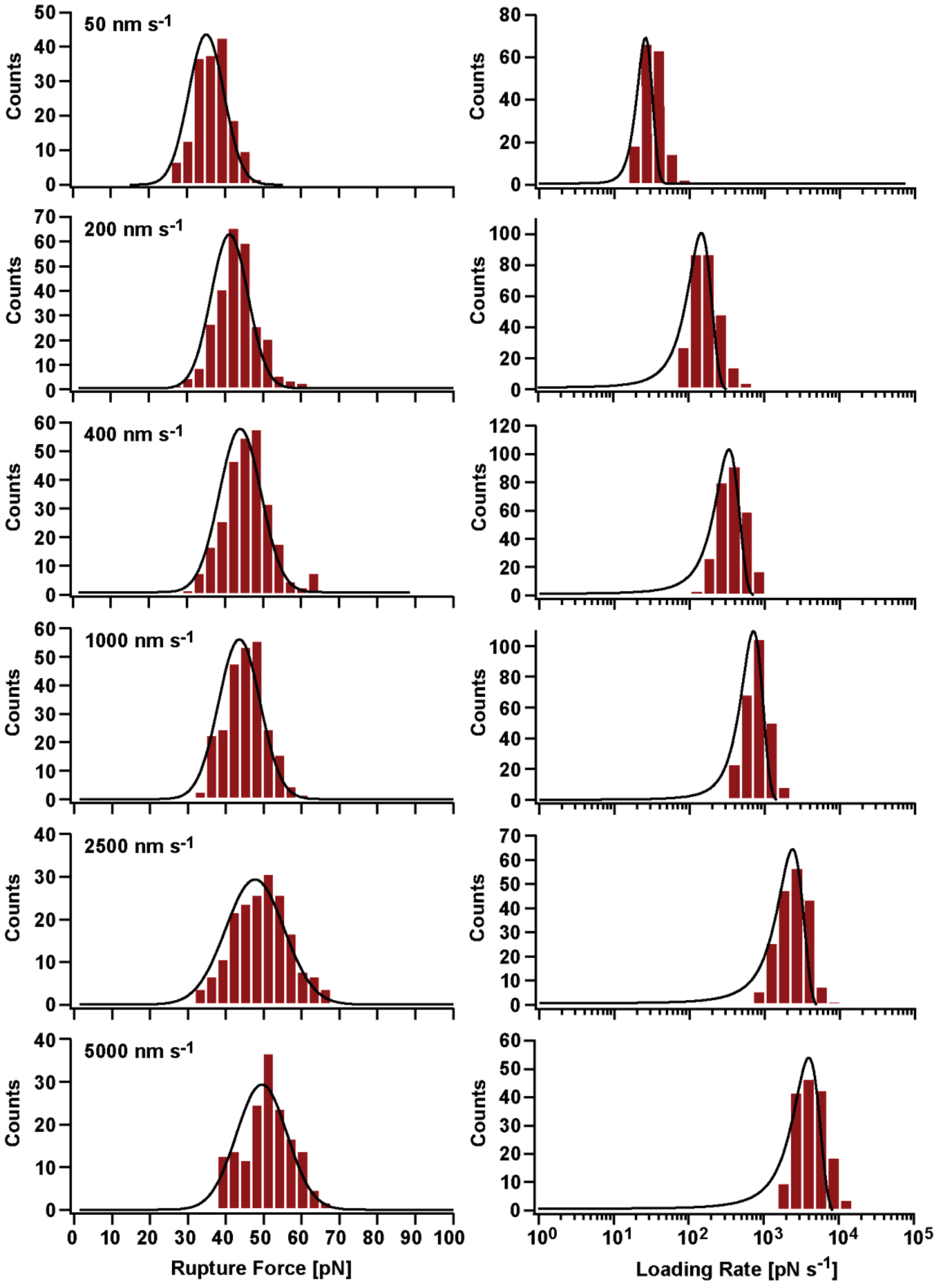

Figure 14. Example data set (Cantilever 1) of CC-A_4B_4 measured at 6 different retract speeds. The black lines represent Gaussian fits to the data. The number of rupture events included in each histogram is listed in table S2. (Reproduced with permission from ref. [118], copyright © Royal Society of Chemistry.)

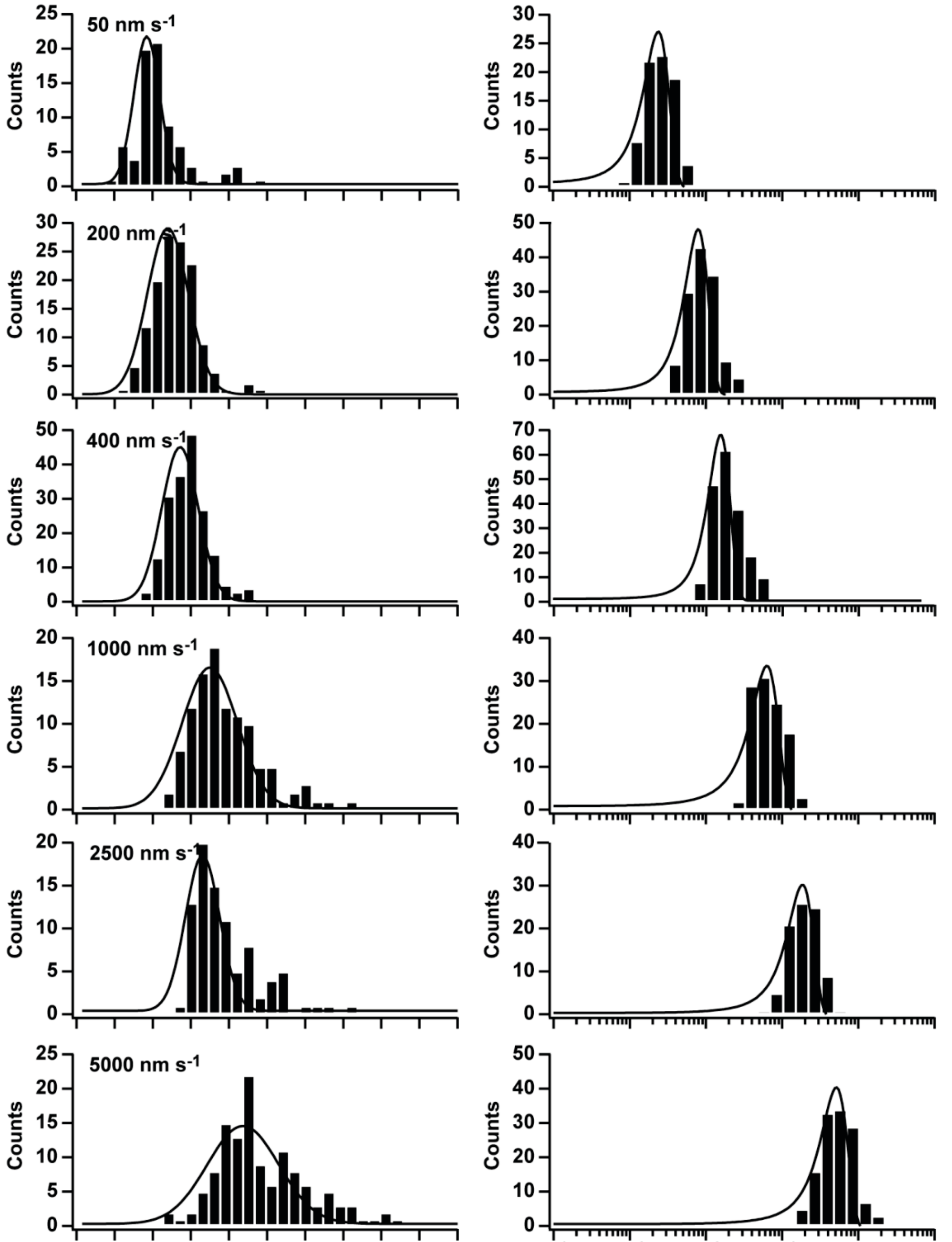

Figure 15. Example data set (Cantilever 1) of CC-$A_4B_{3.5}$ measured at 6 different retract speeds. The black lines represent Gaussian fits to the data. The number of rupture events included in each histogram is listed in table S2. (Reproduced with permission from ref. [118], copyright © Royal Society of Chemistry.)

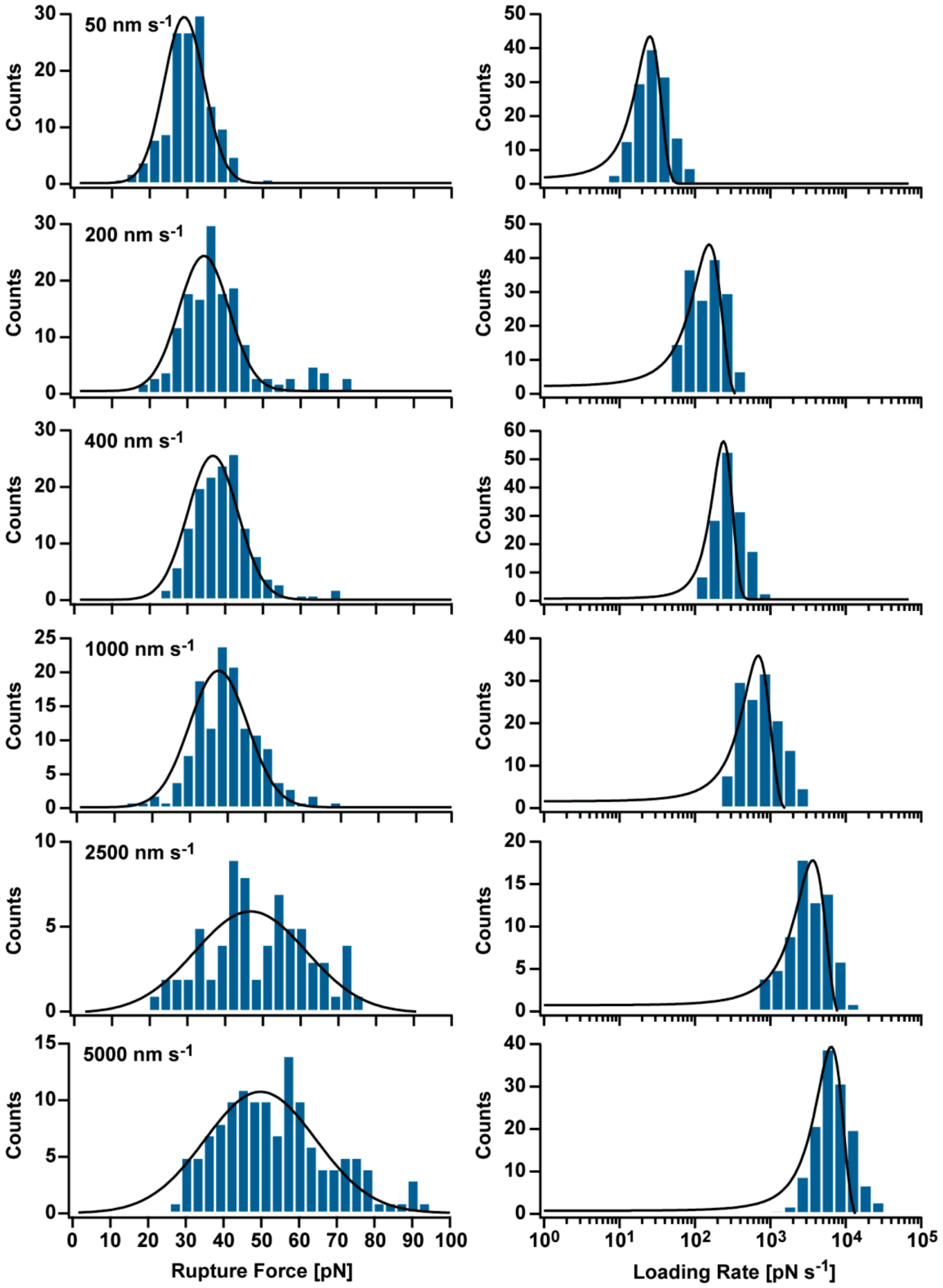

Figure 16. Example data set (Cantilever 1) of CC-A_4B_3 measured at 6 different retract speeds. The black lines represent Gaussian fits to the data. The number of rupture events included in each histogram is listed in table S2. (Reproduced with permission from ref. [118], copyright © Royal Society of Chemistry.)

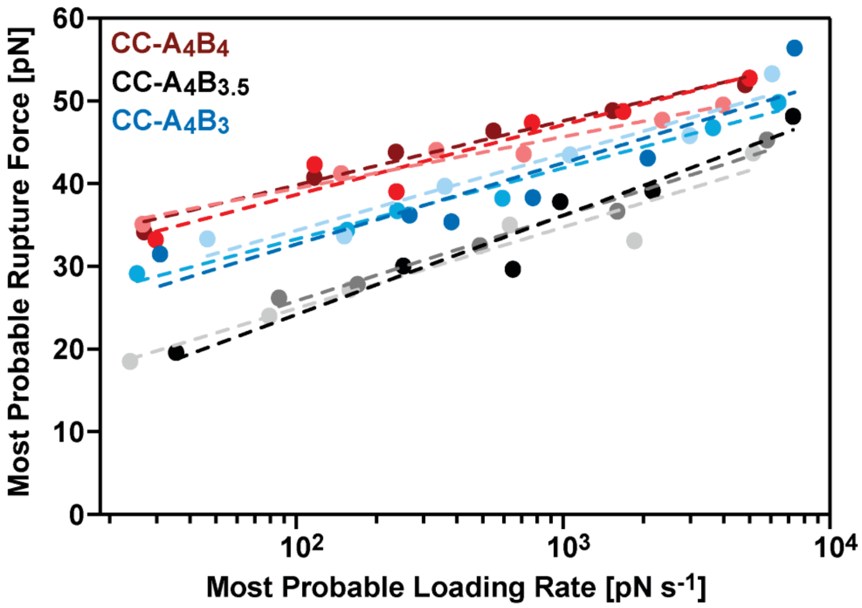

Figure 17. Bell-Evans plot showing a linear relationship between the most probable rupture forces and the logarithm of the corresponding loading rates. The dashed lines represent fits to the Bell-Evans model to extract $k_{\text{off\_SMFS}}$ and Δx_{SMFS} values. For each individual CC three different measurements with different cantilevers and surfaces were performed and analyzed independently; the corresponding data are shown as different shades of the same color. (Reproduced with permission from ref. [118], copyright © Royal Society of Chemistry.)

Table 4. Summary of the $k_{\text{off\_SMFS}}$ and Δx_{SMFS} values for CC-A_4B_4, CC-$A_4B_{3.5}$ and CC-A_4B_3 obtained from the Bell-Evans fits to the SMFS data. The values are the mean of three experiments performed with three different cantilevers and surfaces. The error represents the standard error of the mean (SEM).

Heterodimer	$k_{\text{off\_SMFS}}$ [s^{-1}]	Δx_{SMFS} [nm]
CC-A_4B_4	$(3.2 \pm 2.1) \times 10^{-4}$	1.29 ± 0.12
CC-$A_4B_{3.5}$	$(1.1 \pm 0.4) \times 10^{-1}$	0.89 ± 0.05
CC-A_4B_3	$(6.5 \pm 2.4) \times 10^{-3}$	1.03 ± 0.04

Considering the differences in the thermodynamic stability of these CCs, this trend in the dissociation rates is expected. The observed trend can be interpreted in the following way: the CC is deformed in the direction of the externally applied force, whereby the amount of stably folded CC structure is reduced. A minimum CC length is required for maintaining a thermodynamically and kinetically stable structure [147, 152]. Once the CC has been deformed beyond a critical point, the remaining structure possesses a lower binding free energy and the probability for thermally-assisted dissociation perpendicular to the force axis increases. For shorter heterodimers this critical point, where the remaining folded structure becomes thermodynamically unstable, is reached at smaller extensions, thereby also explaining the correlation between the potential width and CC length. CC-$A_4B_{3.5,}$ containing the overhang of an incomplete heptad repeat, possesses the lowest mechanical stability, even though its thermodynamic stability was determined to be higher than CC-A_4B_3 (**Figure 11, Table 3**). CC-$A_4B_{3.5}$ showed the highest dissociation rate, $k_{\mathrm{off\_SMFS}} = 1.1 \times 10^{-1}$ s^{-1} and the smallest potential width, $\Delta x_{\mathrm{SMFS}} = 0.89$ nm (**Table 4**), suggesting that the presence of the incomplete heptad repeat results in a mechanical destabilization of the CC structure.

2.5 Steered molecular dynamics simulations at different retract speeds

To understand the molecular mechanism of CC shearing, SMD simulations were carried out for the CC-A_4B_4 and CC-A_4B_3 heterodimers with complete heptad repeats. The sequences and the pulling geometry were kept the same as for the SMFS experiments. The only difference was that only one Gly and no Cys residue were used at the N- and C- termini of the sequences (**Figure 7A**). In the SMD simulations, two virtual harmonic springs were used to replace the PEG linkers (**Figure 7B**). The distal end of the N-terminal spring attached to the A_4 peptide was fixed, while the B peptides were stretched parallel to the helical axis via pulling at the distal end of the C-terminal spring.

Simulations were carried out at different retract speeds, ranging from $v = 10^6$ nm s^{-1} to $v = 10^9$ nm s^{-1}. A very similar force-extension behavior was observed for CC-A_4B_4 and CC-A_4B_3 at all retract speeds. The force extension-curves show an initial rise in the force (phase I) followed by a transition to a force plateau at a strain of 15-25% (**Figure 18**). The force-extension behavior of these short, synthetic CCs is therefore highly similar to what was observed in experimental and simulation results for long, natural CCs stretched in a tensile geometry [133, 134, 136, 137, 141, 142, 153-156], except for the absence of phase III. The absence of phase III is a direct result of the CC length and the attachment geometry, as the shear geometry allows the individual short strands to separate before phase III is reached.

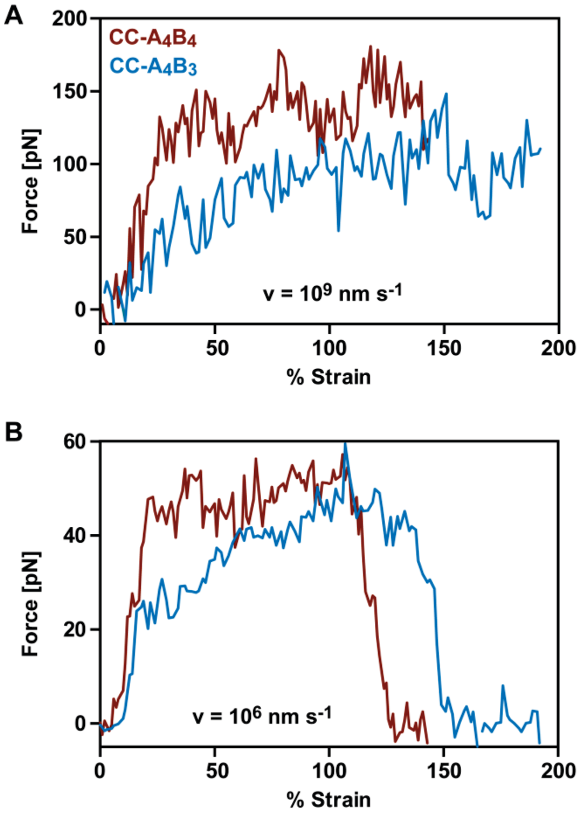

Figure 18. Averaged force-strain curves of the different coiled coils obtained from SMD simulations (T = 300 K, implicit solvent). The graph shows the forces as a function of strain ($\Delta L/L_0$). A) Force-strain behavior at the fastest retract speed (v = 10^9 nm s^{-1}). The results are averaged from 20 (CC-A_4B_3) and 40 (CC-A_4B_4) independent runs. B) Force-strain behavior at the slowest retract speed (v = 10^6 nm s^{-1}). The results are averaged from 5 (CC-A_4B_3) and 6 (CC-A_4B_4) independent runs. (Reproduced with permission from ref. [118], copyright © Royal Society of Chemistry.)

Following the evolution of the helical secondary structure in the simulation trajectories for CC-A_4B_4, reveals that the strand separation mechanism differs at the fastest and slowest retract speeds used (**Figure 19**). At the fastest retract speed used (v = 10^9 nm s^{-1}), the helices begin to uncoil at the points of the force application and the uncoiling propagates along the helices when extended further, until all the helical structure is lost and the strands separate (**Figure 19A**). The propagation of helix uncoiling from the points of the force application has also been observed in the simulations of other dimeric and trimeric CCs that are mechanically loaded parallel to the helical axis [134, 136, 156-158]. In case of the slowest retract speed used ($v = 10^6$ nm s^{-1}), the helices seem to slide against each other. When inspected carefully, the trajectories show that the helices do actually uncoil when mechanically loaded, however, they are able to recoil during the timescale of the simulation, resulting in a relative displacement of the helices against each other (**Figure 19B**). In the following, this mechanism is termed uncoiling-assisted sliding. At intermediate retract speeds, strand separation involves a combination of both mechanisms.

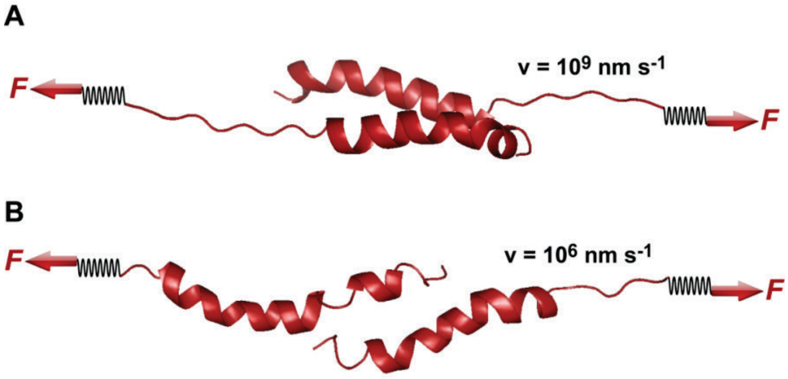

Figure 19. Coiled coil response to an applied shear force in SMD simulations. A) Simulation snapshots of CC-A_4B_4 obtained at the fastest ($v = 10^9$ nm s^{-1}) retract speed. The helices begin to uncoil at the points of force application. B) Simulation snapshots of CC-A_4B_4 obtained at the slowest ($v = 10^6$ nm s^{-1}) retract speed. The helices dynamically uncoil and recoil as a response to the applied force, resulting in a relative displacement of the helices against each other. (Reproduced with permission from ref. [118], copyright © Royal Society of Chemistry.)

Helix recoiling has also been observed in constant-force simulations of dimeric CCs loaded in a tensile geometry, i.e. where all termini were loaded simultaneously. In these simulations, helix recoiling occurred with a much higher probability at lower loads [159]. Extrapolating from simulation data obtained at retract speeds faster than 10^{-9} nm s^{-1}, Buehler et al. [136, 137] predicted that stretching of the vimentin CC in a tensile geometry involves a change in mechanism at a retract speed of approximately 10^8 nm s^{-1}. This speed falls into the range used in the simulations represented in this work. For fast retract speeds, Buehler et al. [136, 137] observe that only hydrogen bonds next to the point of force application feel the force and that helix uncoiling is highly localized, as also observed in the simulations represented here at the fastest retract speed of 10^9 nm s^{-1} (**Figure 19A**). For retract speeds slower than 10^8 nm s^{-1}, it is proposed that the force is distributed more homogeneously throughout the structure so that uncoiling can initiate anywhere in the helices. This regime matches the timescales observed for the formation of helical structure in individual helices [160, 161] and is reproduced in the simulations performed here, which show that the helices dynamically uncoil and recoil in response to the applied force. Overall, these results indicate that the molecular mechanism of CC shearing shows a retract speed dependent behavior, with an increasing contribution of helix recoiling and uncoiling-assisted sliding at slower retract speeds.

2.6 Comparison of single-molecule force spectroscopy experiments and steered molecular dynamics simulations: Can the plateau phase be observed experimentally for short heterodimeric coiled coils under shear load?

Following this mechanistic interpretation of CC shearing in the SMD simulations, the next goal of this work was to quantitatively compare the force range seen in the SMD simulations with the data obtained from the SMFS experiments.

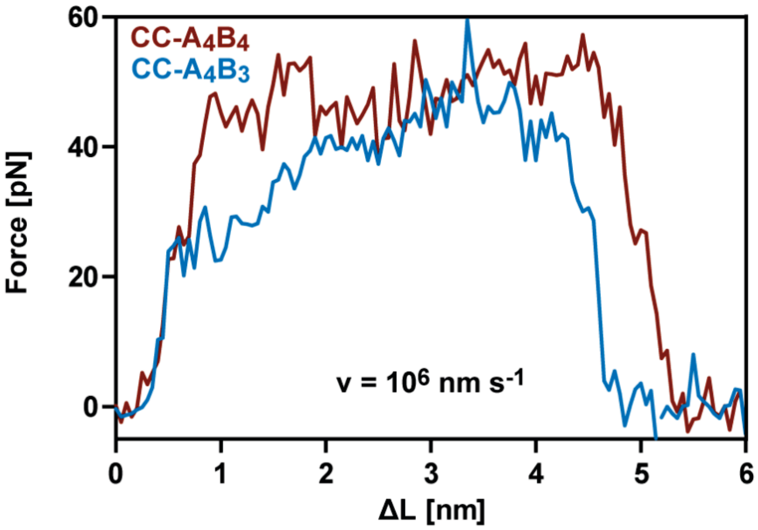

Figure 20. Averaged force-extension curves of the different coiled coils obtained from SMD simulations ($T = 300$ K; implicit solvent). The graph shows the forces as a function of extension ($\Delta L = v \times t$, where v is the retract speed and t is time). Force-extension behavior at the slowest retract speed ($v = 10^6$ nm s^{-1}). The results represent averages over 5 (CC-A_4B_3) or 6 (CC-A_4B_4) independent runs. (Reproduced with permission from ref. [118], copyright © Royal Society of Chemistry.)

The SMD force-extension curves of CC-A_4B_4 and CC-A_4B_3 show that the transition from phase I to phase II occurs at different forces and that the plateau forces are larger for CC-A_4B_4 than for CC-A_4B_3 at the slowest retract speed ($v = 10^6$ nm s^{-1}), indicating a dependence on CC length (**Figure 20**). The average plateau force for each CC was calculated by averaging the force values over an extension interval of $2 < \Delta L < 4$ nm at the retract speed of 10^6 nm s^{-1} and it was around 50 pN for the longest heterodimer, CC-A_4B_4, and 35 pN for the shortest heterodimer, CC-A_4B_3. It should be considered that the slowest retract speed applied in the SMD simulations ($v = 10^6$ nm s^{-1}) was still 200 times higher than the fastest retract speed that was applicable for SMFS experiments ($v = 5 \times 10^3$ nm s^{-1}). This would correspond to a loading rate two to three orders of magnitude larger than experimentally accessible values. Despite this difference in loading rates, the average plateau forces (CC-A_4B_4: 50 pN, CC-A_4B_3: 35 pN) observed at the slowest retract speed for SMD simulations (**Figure 20**) were in the same range with the experimental values (CC-A_4B_4: ~35-50 pN, CC-A_4B_3: ~30-50 pN determined over a broad loading rate regime (**Figure 17**).

In the SMD simulations, the phase I to phase II transition occurs at $\Delta L = 1$ nm. The force plateau (phase II) shows a maximum length of 4 nm for the longest heterodimer, CC-A_4B_4 (**Figure 20**), at the slowest retract speed ($v = 10^6$ nm $s^{-}1$) where dynamic helix uncoiling and recoiling was observed (**Figure 19B**). However, in case of the experimental force-extension curves for the 3-4 heptad long CC heterodimers, it was not possible to observe this plateau phase before the rupture event occurs (**Figure 12B**). Previously shown potential width (Δx_{SMFS}) values (**Table 4**) obtained from the Bell-Evans fits to the experimental data also indicated relatively small transition state distances for the 3-4 heptad long CCs ($\Delta x_{CC\text{-}A4B4}$: 1.29 nm and $\Delta x_{CC\text{-}A4B3}$: 1.03 nm). Even though a direct comparison to the experimental Δx_{SMFS} values cannot be done, SMD data showed that the transition to the plateau phase occurs at an extension of $\Delta L = 1$ nm for the longest heterodimer tested (CC-A_4B_4), which was close to the experimental potential width value ($\Delta x_{CC\text{-}A4B4}$: 1.29 nm). These results suggest that the rupture event (i.e., strand separation) of the CCs under shear geometry in the SMFS experiments might occur shortly after the transition to the plateau phase, where parts of the helical structure are already uncoiled and the CC heterodimer becomes thermodynamically unstable. Considering the thermal noise level present in the experimental force-extension curves, the possible occurrence of a short force plateau directly before the rupture event was most likely not resolved for CC-A_4B_4 (**Figure 21B**). However, the correlation between the

CC length and Δx_{SMFS} values (**Table 4**) discussed earlier confirms that longer CCs can tolerate larger deformations before the strands separate under experimental conditions.

Previous experimental studies [133, 134, 141, 154] also showed that long, natural CCs loaded under tensile geometry can exhibit an unfolding transition (α-helix to β-sheet), which results in a force plateau (phase II) and is followed by a step increase in the force (phase III). Considering this knowledge and the findings regarding the length dependence for short heterodimeric CCs tested here, it can be hypothesized that the plateau phase could experimentally be resolved for CCs longer than 4 heptads under shear geometry. To test this hypothesis, a longer heterodimeric CC sequence with 5 heptad repeats (CC-A_5B_5) was designed (**Figure 21A**)

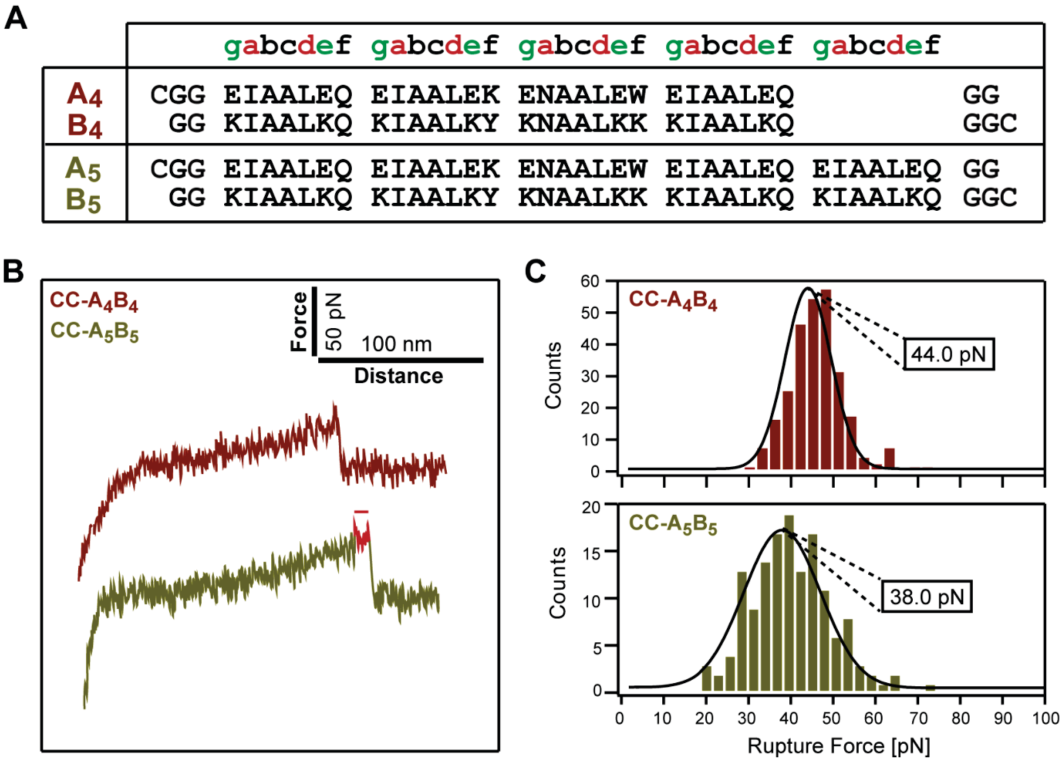

Figure 21. Single-molecule force spectroscopy results comparing the CC-A_4B_4 and CC-A_5B_5 systems. A) Sequences of the CC heterodimers used for resolving the force plateau in SMFS experiments. B) Representative force-extension curves of CC-A_4B_4 and CC-A_5B_5 obtained from SMFS measurements. The red line represents the plateau region (~7.2 nm) for CC-A_5B_5. C) Representative rupture force histograms of CC-A_4B_4 and CC-A_5B_5 recorded at a retract speed of 400 nm s^{-1}. The rupture force histograms contain 285 rupture events for CC-A_4B_4 and 196 rupture events for CC-A_5B_5, respectively. The black lines represent Gaussian fits to the data.

The same experimental setup was used for the SMFS measurements, as described earlier. The A_5 peptide was immobilized to glass surfaces while the cantilevers were functionalized with the B_5 peptide. For CC-A_5B_5, a small number (<5%) of force-extension curves showed a small force plateau right before the rupture event, which was not experimentally observed for the CC-A_4B_4 heterodimer (**Figure 21B, 22**). Previous measurements performed with natural CCs showed that the CC structure can be overstretched up to 2.5 times of its original length during the plateau phase where the unfolding transition occurs [133]. This number is very close to the expected length difference between a folded CC structure (1.4 Å per residue) and the completely unfolded polypeptide chain (3.6 Å per residue) [133]. According to these numbers, a maximum plateau length of 7.7 nm ((3.6 – 1.4 Å) × (7 × 5 residues) = 77 Å) can be observed for a 5-heptad long CC motif when the CC structure is completely unfolded under a tensile geometry. For CC-A_5B_5, the length of the observed plateau region obtained from the experimental force-extension curves was in the expected range, but generally smaller (~5-7 nm) than the maximum value for a fully unfolded 5 heptad-long CC chain (**Figure 22**). Due to the additional degrees of freedom in the shear geometry, strand separation will most likely occur perpendicular to the helical axis, before the CC structure is fully unfolded. When the remaining folded structure becomes thermodynamically unstable, the CC heterodimer dissociates, which results in the observation of the rupture event either before or right after the plateau phase is reached. For the short CCs used (3-5 heptad repeats), this explains the low frequency of observing the plateau phase, as well as the length of the observed plateau region.

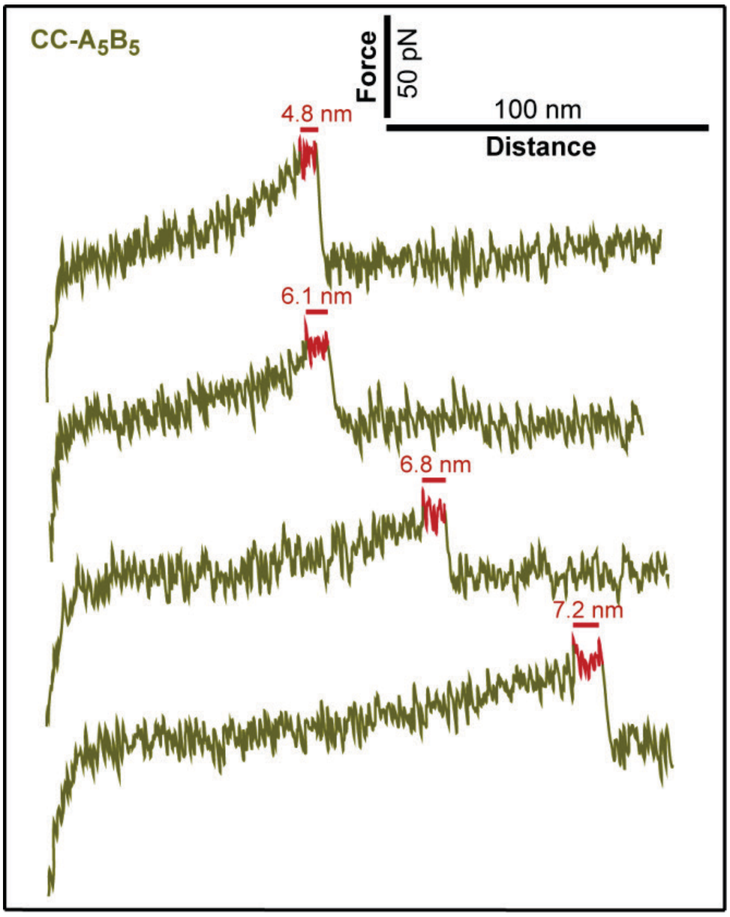

Figure 22. Representative force-extension curves for CC-A_5B_5 obtained from SMFS measurements at a retract speed of 400 nm s^{-1}. Red lines represent the plateau phase.

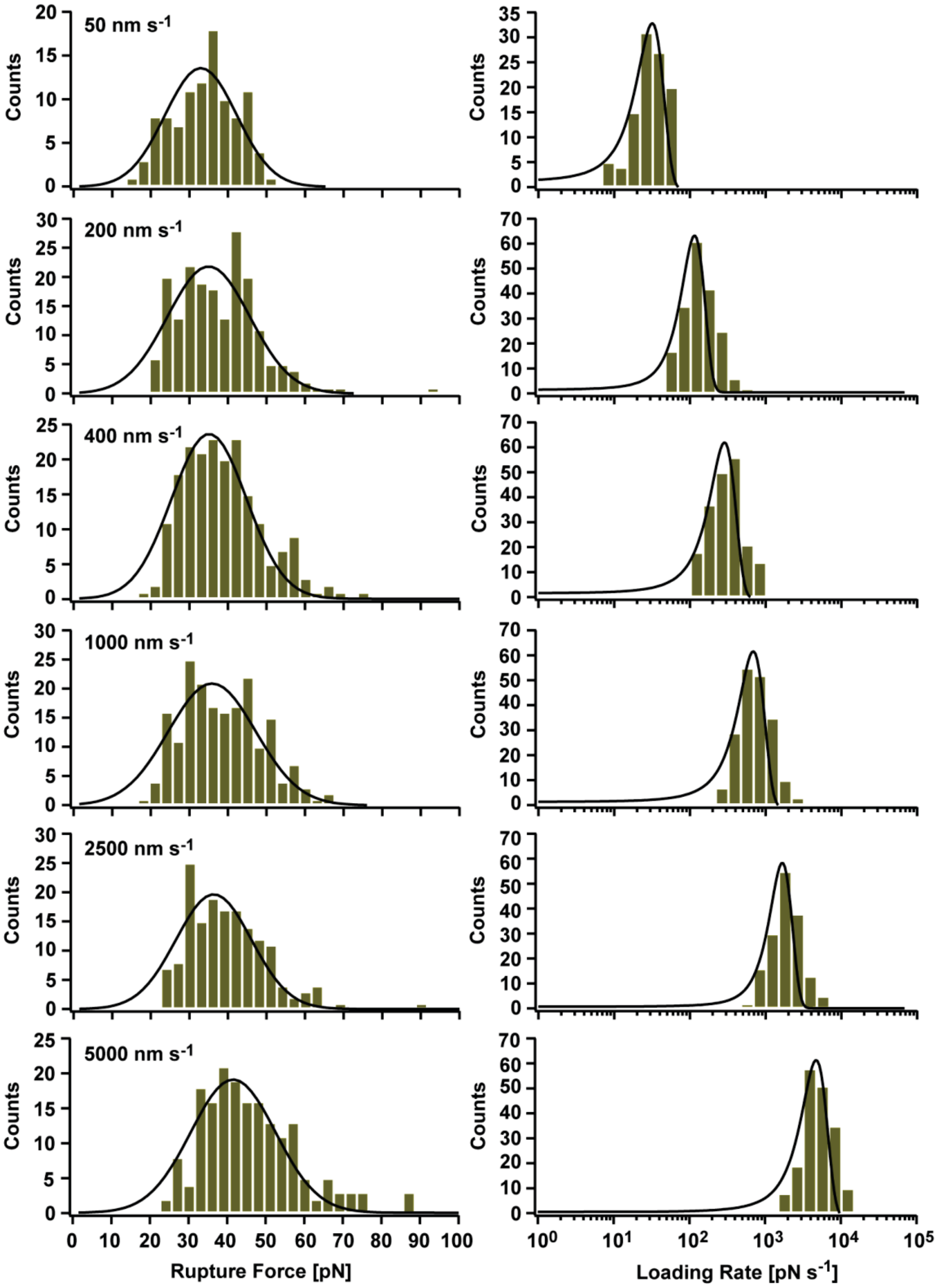

Figure 23. Example data set (Cantilever 1) of CC-A_5B_5 measured at 6 different retract speeds. The black lines represent Gaussian fits to the data. The number of rupture events included in each histogram is listed in table S2.

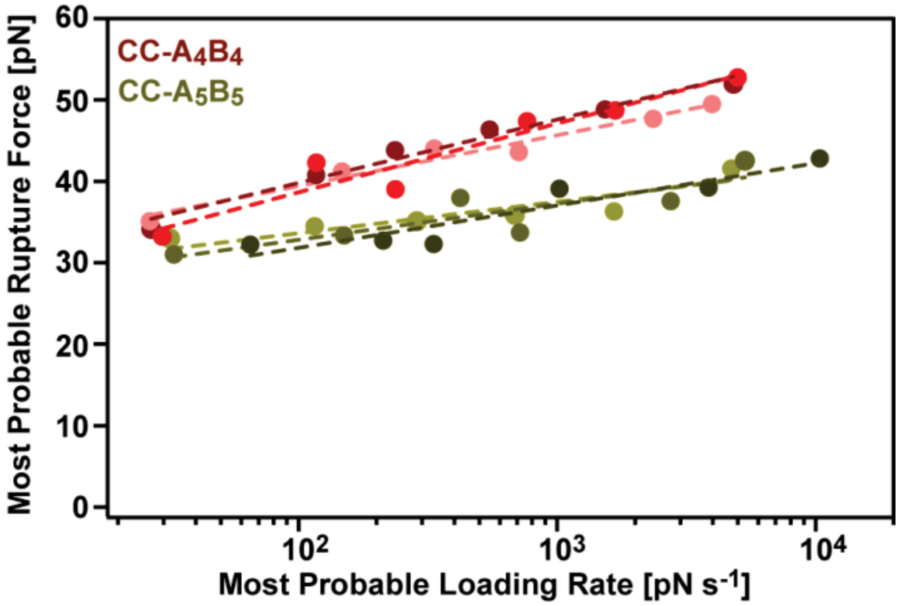

Figure 24. Bell-Evans plot showing a linear relationship between the most probable rupture forces and the logarithm of the corresponding loading rates for CC-A_4B_4 and CC-A_5B_5. The dashed lines represent fits to the Bell-Evans model to extract $k_{\mathrm{off\_SMFS}}$ and Δx_{SMFS} values. For each individual CC three different measurements with different cantilevers and surfaces were performed and analyzed independently; the corresponding data are shown as different shades of the same color.

In addition to the appearance of a short force plateau, also the dynamic force range differs for CC-A_5B_5. **Figure 21C** shows representative rupture force distributions for CC-A_4B_4 and CC-A_5B_5 recorded at a retract speed of 400 nm s^{-1}, where the most probable rupture forces were determined as 38 pN for CC-A_5B_5 and 44 pN for CC-A_4B_4. The most probable rupture force values obtained at different retract speed were always lower for CC-A_5B_5 than for CC-A_4B_4 (**Figure 14, 23, 24, S4-5, S10-11, Table S2**), which is in contradiction to previous findings showing a positive correlation between CC length and mechanical stability. When the most probable rupture force values, F, were plotted against the corresponding ln $\dot{F}$ values, the results indicated that the CC-A_5B_5 still follows the general trend where the rupture forces increase linearly with the logarithm of the loading rates, as predicted by the Bell-Evans model (**Figure 24**). However, the slope of this linear increase is much lower for CC-A_5B_5 than for CC-A_4B_4. The force-free dissociation rates, $k_{\mathrm{off\_SMFS}}$ and the corresponding potential width values, Δx_{SMFS} obtained from the Bell-Evans fits, on the other hand, were in agreement with the previous results. The longer heterodimer, CC-A_5B_5, possessed a slower dissociation rate ($k_{\mathrm{off\_SMFS}}$= 1.2 × 10^{-5} s^{-1}) and a larger potential width (Δx_{SMFS}= 2.14 nm) when compared to the shorter CC-A_4B_4 ($k_{\mathrm{off\_SMFS}}$= 3.2 × 10^{-4} s^{-1}; Δx_{SMFS}= 1.29 nm) (**Table 5**). This trend indicates again that the longer CCs can maintain a thermodynamically and kinetically more stable structure under a larger deformation. CD results further supported the higher thermal stability of CC-A_5B_5 (T_m > 90ºC) (**Figure S2, Table S1**).

Table 5. Summary of the k_{off_SMFS} and Δx_{SMFS} values for CC-A_4B_4 and CC-A_5B_5 obtained from the Bell-Evans fits to the SMFS data. The values are the mean of three experiments performed with three different cantilevers and surfaces. The error represents the standard error of the mean (SEM).

Heterodimer	k_{off_SMFS} [s^{-1}]	Δx_{SMFS} [nm]
CC-A_4B_4	$(3.2 \pm 2.1) \times 10^{-4}$	1.29 ± 0.12
CC-A_5B_5	$(1.2 \pm 1.1) \times 10^{-5}$	2.14 ± 0.18

One possible explanation for the observed decrease in the mechanical stability (i.e. rupture forces) for CC-A_5B_5 in the investigated loading rate range might be as follows: the CC-A_5B_5 sequence was designed in a way that the N and C-terminus heptad repeats were kept the same as for CC-A_4B_4 to eliminate the possible effect of altered helical stability of different heptad sequences at the points where the force was first applied during the experiments (**Figure 21A**). Yet, during the shearing of the individual helices, uncoiling-assisted sliding may lead to the formation of intermediate structures with different heptad registers displaying an altered mechanical stability for CC-A_5B_5. The alternative heptad registers for CC-A_5B_5 might exhibit lower rupture forces, while the longer structure still maintains its thermal stability and tolerates larger amounts of deformation, resulting in a lower dissociation rate, k_{off} and a larger potential width, Δx.

Overall, these results indicate that short CC heterodimers (3-5 heptad repeats) rupture at forces below or just at the plateau force at experimentally relevant loading rates. The obtained plateau forces (~20-40 pN) (**Figure 22**) are in good agreement with the values recorded for experimentally tested natural CCs (~20-60 pN) [133, 134, 141, 154]. In previous experimental studies performed on long, natural CC sequences, an α-helix to β-sheet transition has frequently been observed during the plateau phase (phase II) and SMD simulations of short CC sequences predicted that this transition can also occur for CCs with a critical minimum length of 4-6 heptads, depending on the loading rate. To fill the gap of experimental model systems to investigate this α-β transition for short synthetic CCs, a 6 heptad-long heterodimer

(CC-A_6B_6) was further designed (**Figure S12A**) and experimentally tested in this study. Preliminary results show evidence for the occurrence of a 3-phase structural response to the mechanical shear load with a possible plateau force of ~20-40 pN over a plateau length of ~6-11 nm (**Figure S12B, S12C**). Due to the thermal noise level in the experimental force-extension curves, it was hard to designate the borders between phase transitions with high precision. This might explain the measured plateau length values exceeding the expected maximum length for a 6-heptad CC ((3.6 – 1.4 Å) × (7 × 6 residues) = 92 .4 Å = 9.24 nm). The preliminary results for CC-A_6B_6 can be found in the Appendix, Section A4.

Even though these preliminary results provide the first evidence that the α-β transition (phase III) can be experimentally resolved for CCs with a critical minimum length of 5-6 heptads under shear geometry, further investigation is still required to fully demonstrate the molecular structural changes during the transition between different phases. The possible contribution of helix uncoiling and uncoiling-assisted sliding to CC deformation and strand separation cannot be determined from the experimental force-extension curves for these 5-6 heptad-long CCs possessing mechanical phase transitions. SMD simulations can potentially contribute to the further investigation of the molecular details of the α-β transition for 5-6 heptad-long heterodimeric CCs mechanically loaded under shear geometry.

2.7 Time-dependent cell adhesion experiments with 3T3 fibroblasts

To test the application potential of short heterodimeric CCs as building blocks for MFSs, 2D cell culture experiments with 3T3 fibroblasts were performed as a proof-of-concept. For this purpose, the 4- and 5 heptad-long CCs were equipped with the cell adhesive ligand RGDS and assembled on a glass cover slip in a two-step procedure. The A_4 and A_5 peptides were covalently coupled to the glass surface via a PEG linker, and a solution of the RGDS-functionalized B_4 and B_5 peptides was subsequently incubated on the functionalized areas. This strategy facilitates the non-covalent self-assembly of the CC heterodimer on the surface to yield the MFS constructs, termed A_4B_4-MFS and A_5B_5-MFS, respectively (**Figure 25, 26**).

MFS	gabcdef gabcdef gabcdef gabcdef gabcdef
A_4 B_4-RGDS	CGG EIAALEQ EIAALEK ENAALEW EIAALEQ GG GG KIAALKQ KIAALKY KNAALKK KIAALKQ GGGRGDS
A_5 B_5-RGDS	CGG EIAALEQ EIAALEK ENAALEW EIAALEQ EIAALEQ GG GG KIAALKQ KIAALKY KNAALKK KIAALKQ KIAALKQ GGGRGDS

Figure 25. Sequences of the RGDS-functionalized coiled coil heterodimers used as molecular force sensors.

Utilization of a PEG linker has a number of advantages for setting up the MFS proof-of-concept experiments. PEG is known to be a biocompatible molecule, which is suitable for cell biology applications. It possesses anti-fouling properties, i.e. surfaces sufficiently coated with PEG become resistant to protein adsorption [162, 163]. In the MFS experiment, the dense PEG layer yields a well-passivated surface for preventing the non-specific adhesion of cells to the glass surface. Cell attachment is only possible via the RGDS-functionalized MFSs, where the RGDS sequence was incorporated at the C-termini of the original B_4 and B_5 peptide sequences during solid-phase synthesis (**Figure 25).** RGDS is a well-known adhesive ligand found in the structure of several ECM proteins, such as fibronectin, vitronectin, fibrinogen, etc. It serves as a recognition motif for several integrin receptors, including all five α_V integrins, $\alpha_{IIb}\beta_3$ and two β_1 integrins (α_5, α_8) [16, 164]. The 3T3 fibroblasts used in this study are known to express $\alpha_5\beta_1$ integrins, which show a high affinity to the linear RGDS ligand used in the MFS design.

Here, the application potential of CC-based MFSs was tested with the goal of probing the threshold force required for cell adhesion via single integrin-ECM ligand bonds (specifically, integrin $\alpha_5\beta_1$ and its ligand, the linear RGDS peptide). In this two-component design, MFS constructs are held together via the non-covalent interaction of individual α-helices (**Figure 26**). Therefore, once the MFS construct is immobilized to the glass surface, the CC heterodimer acts as a force probe, which ruptures at a critical, pre-calibrated threshold force. When cells are seeded on the MFS-functionalized surface, integrin receptors engage with the cell-adhesive RGDS ligand and the cells start applying force to the CC-based MFS. The CC heterodimer ruptures when the cell applied force exceeds the pre-calibrated force, leading to the detachment of the cells together with the RGDS-functionalized B-peptide. In order words, if the CC-based MFS cannot withstand cell-applied forces, the system cannot promote cell adhesion to the surfaces. In contrast, if the cell-applied forces do not exceed the threshold force for CC rupture; the MFS can endure the integrin-ligand forces and further support cell adhesion to the surfaces.

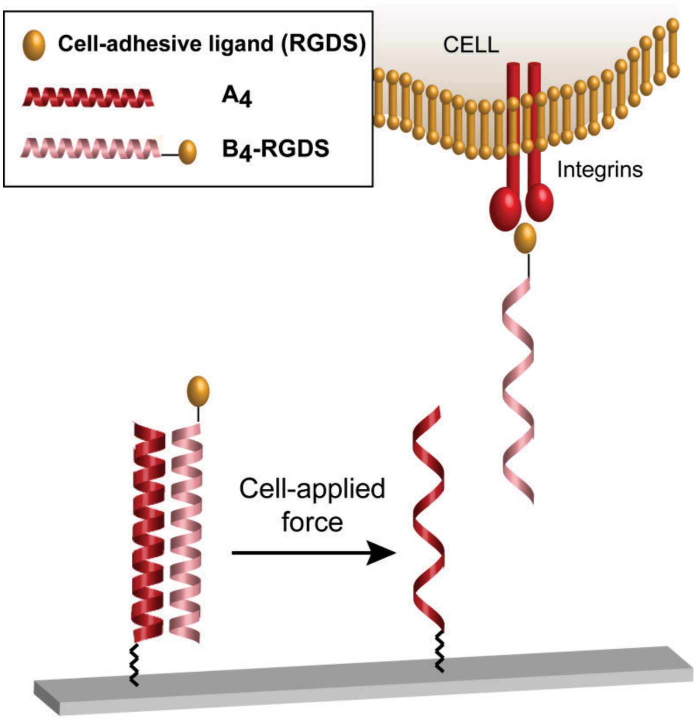

Figure 26. Experimental setup for 2D cell culture experiments. The A_4 peptide is covalently coupled to glass coverslips via the NHS-PEG-maleimide linker, while the complementary B_4-RGDS peptide is non-covalently self-assembled with the A_4 peptide to form A_4B_4-MFS. The same immobilization strategy was used for A_5B_5-MFS. If the MFS is strong enough to withstand cell-applied forces, cell adhesion to the surfaces is observed. If cell-applied forces exceed the rupture force of the MFS, cell attachment to the surfaces is not supported.

Initially, to show that cellular adhesion was specific to the RGDS ligand, control experiments were performed with 3T3 fibroblasts. Observing cell adhesion and growth for 120 min after seeding, different controls were performed to prove that the cells did not adhere to the surface or the CC non-specifically (**Figure 27**). As a negative control, the glass surface functionalized only with the PEG linker and the A_4 peptide were both tested separately. To observe the general morphology of the cells during early cell adhesion, the polystyrene tissue culture plate (TCP) was used as a positive control. An additional positive control was also included as a 'high-force control', where the short CGGGRGDS peptide was covalently coupled to the PEG linker. The mechanical stability of this covalent bond should withstand forces exceeding 100 pN.

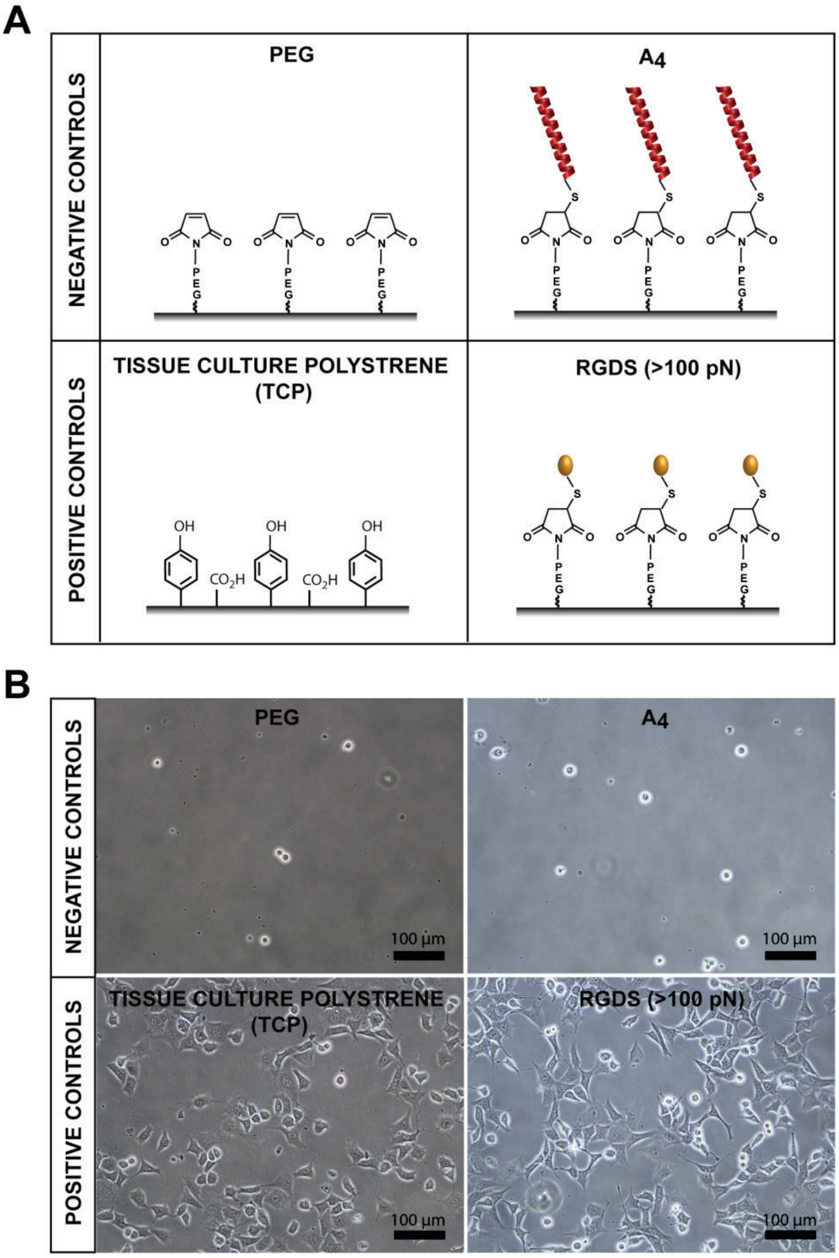

Figure 27. Control groups used in 2D cell culture experiments. A) Schematic representation of the surface chemistry used for the negative and positive controls. B) Phase-contrast images showing the adhesion behavior of 3T3 fibroblasts on the control surfaces after 120 min of incubation. Scale bars: 100 µm.

Phase-contrast images of 3T3 fibroblasts on control surfaces (**Figure 27B**) revealed that the PEG passivation (PEG control) efficiently prevented the non-specific adhesion of cells to the glass surface. Similarly, no cell adhesion was observed in the absence of the cell-adhesive RGDS ligand (A_4 control). The positive control (RGDS control) showed that cell attachment was only promoted when the surface presented the cell-adhesive RGDS ligand. The general morphology of adherent cells was highly similar for the RGDS and TCP controls, indicating that the RGDS density was sufficient to overcome the passivating properties of the PEG layer.

After proving that cell adhesion to the functionalized surfaces was specific to the RGDS ligand, A_4B_4-MFS and A_5B_5-MFS were used in time-dependent adhesion experiments to test the application potential of the CC-based MFS design for monitoring cell-applied forces. These two CCs were initially chosen for the proof-of-concept experiments, as they are the mechanically and thermodynamically most stable heterodimers. The dynamic force range was determined to be ~35-50 pN for CC-A_4B_4, while it was around ~30-40 pN for CC-A_5B_5 (**Figure 24**). The thermal denaturation experiments showed a melting temperature of ~80.5ºC for CC-A_4B_4 and >90.0ºC for CC-A_5B_5 (**Figure S2**, **Table S1**).

During the time-dependent adhesion experiments, it was observed that a portion of 3T3 fibroblasts adhered to both RGDS (positive control, rupture force >100 pN) and A_4B_4-MFS (rupture force ~35-50 pN) surfaces within the first 30 min of incubation (**Figure 28**). For the longer time periods (60 min and 120 min), the RGDS surfaces were able to maintain cell adhesion and spreading, while cell detachment was observed on the A_4B_4-MFS surfaces (**Figure 28, S15**). On the other hand, A_5B_5-MFS (rupture force ~30-40 pN) was able to maintain cell attachment for 120 min (**Figure 28, S15)**. The density of the adhered cells was similar to the RGDS control, indicating that the concentration of available cell-adhesive ligands was equally sufficient for supporting cell attachment. As the concentration of the CGGGRGDS and B_5-RGDS (500 µM) peptides was the same in both experiments, this suggests that the density of immobilized RGDS remained almost constant over the time scale of the experiment. This observation may seem surprising considering the calibrated force range of the two different MFS systems tested here. For the experimentally accessible loading rates (SMFS), the dynamic force range of A_4B_4-MFS (~35-50 pN) was determined to be higher than the A_5B_5-MFS (~30-40 pN) system. Obviously, not only the force range, but also the thermodynamic stability and the kinetics of the bond rupture are crucial parameters to define the overall stability of a two-component CC-based MFS in the cell culture system. In particular, the thermodynamic stability defines the intrinsic half-life of the surface bound CC-based MFS and this parameter may increasingly contribute for maintaining long-term cell attachment.

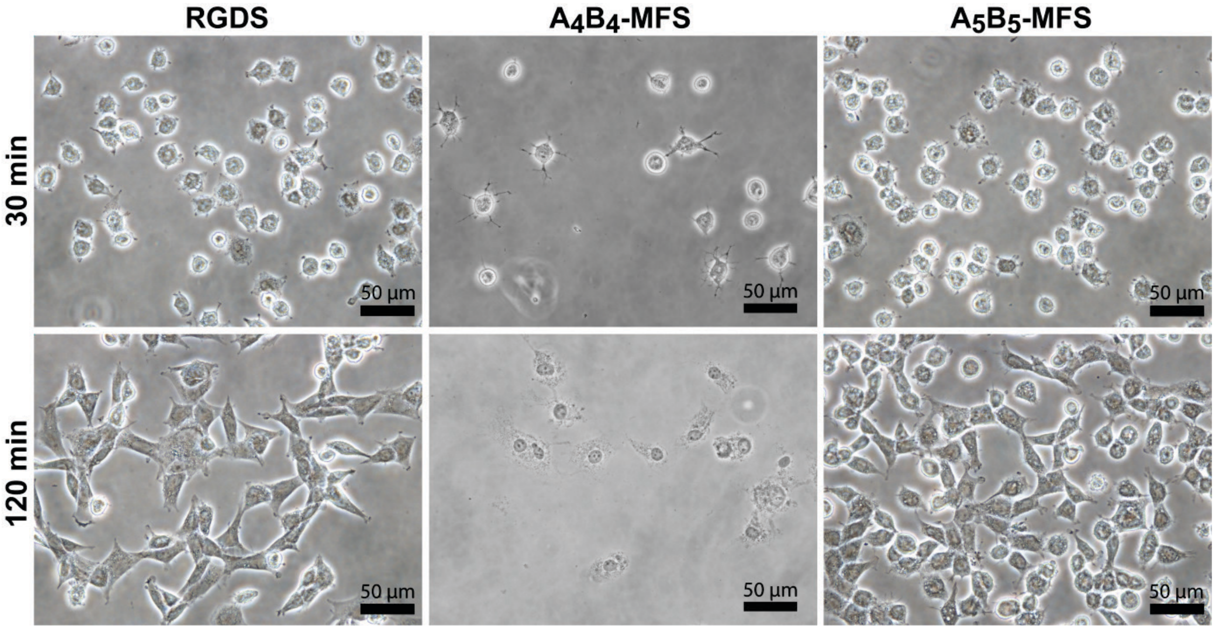

Figure 28. Phase-contrast images of 3T3 fibroblasts grown on glass surfaces functionalized with RGDS, A_4B_4-MFS and A_5B_5-MFS. The images were taken after 30 min and 120 min of incubation. Scale bars: 50 µm.

2.8 Testing the application potential of coiled coil based molecular force sensors with a medically-relevant model system

The proof-of-concept experiments performed with 3T3 fibroblasts showed that the CCs can be used as mechanosensitive building blocks and that CC-based MFSs with different stability can be utilized for determining the threshold force required for cell-adhesion. To further test the application potential of CC-based MFSs for different cell types, additional experiments have been performed with an endothelial cell line. Wild type (WT) endothelial cells were compared with cells that carry mutations in a signaling pathway with essential function for cell adhesion and mechanotransduction. These mutations are relevant to a vascular disease and the mutant cells possess a different cytoskeletal architecture, accompanied by altered adhesion behavior. Here, the CC-based MFS design was used to investigate this medically relevant model system with a focus on determining how these alterations in the cellular adhesion process affect cell-applied forces (i.e., traction forces) and how mutations in this signaling pathway determine regulation of mechanotransduction at the cell-ECM interface.

2.8.1 Characterization of the morphology and cytoskeletal organization of endothelial cells carrying mutations linked to cell-adhesion and mechanotransduction

AFM-based quantitative imaging (QI) was used to visualize alterations in the morphology and cytoskeletal organization of WT and mutant endothelial cells. The mutant cells possess altered mechanobiochemical signaling, which affects cell-adhesion and mechanotransduction at the cell-ECM interface. Fully confluent endothelial cell monolayers were used for the characterization to allow the cells to establish cell-cell junctions. For this particular cell type, fully formed junctions are known to be relevant for a balanced mechanical interdependence of cadherin-mediated cell-cell and integrin-mediated cell-ECM interactions.

To investigate the adhesion behavior and general morphology of WT and mutant endothelial cells (M1 and M2), AFM height images were compared. The height profiles of confluent monolayers with fully formed cell-cell contacts show distinct morphological differences between WT and mutant cells (**Figure 29**). The WT cells generally adapted a more globular morphology, while the M1 and M2 cells tend to spread more (**Figure 29**). To quantify these differences, cross-sectional height profiles (**Figure 29A, B**) were generated for each cell type and the height difference between the highest point of the cell body (peak) and the cell-cell junctions (valley) was calculated (**Figure 29C**). The mean peak-to-valley heights show a significant difference between WT and mutant cells, indicating a flattened cell body and increased spreading for mutant cells. The averaged peak-to-valley height was ~4.4 µm for WT cells, while it was approx. 2.8 µm for M1 and 3.1 µm for M2 cells (**Figure 29C, D**).

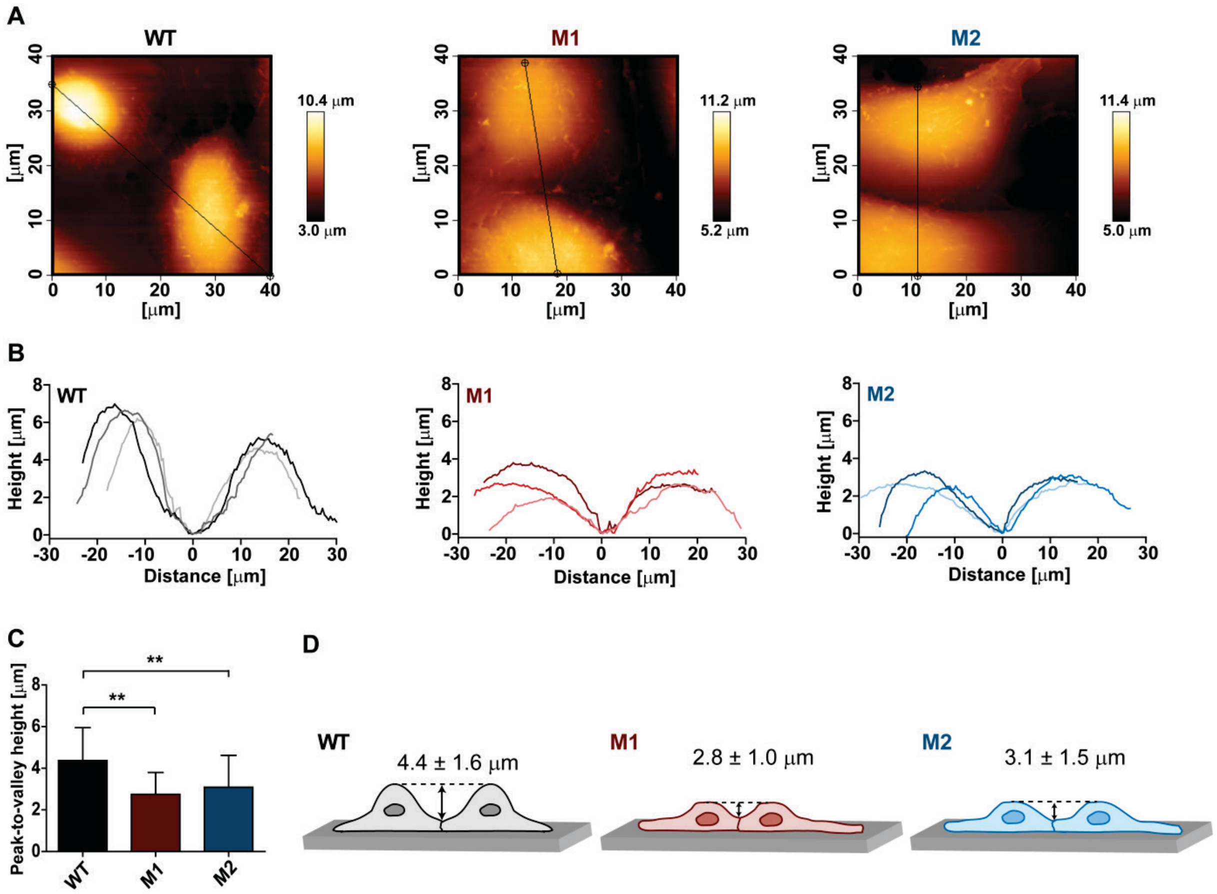

Figure 29. AFM height images of WT endothelial cells and endothelial cells carrying different mutations (M1 and M2). A) Representative height images. B) Representative height profiles obtained for the cross-sectional lines shown in the height images. C) Bar graph showing the peak-to-valley heights extracted from the height profiles. The values were averaged from 18-33 cells. The data are shown as mean ± SD (one-way ANOVA with post-hoc Bonferroni test, n = 18-33); $^{**}P < 0.01$. D) Scheme showing the typical morphology and spreading behavior of cells. The values given represent the calculated peak-to-valley heights (mean ± SD).

In addition to these morphological features, AFM-based, high-resolution QI also yielded stiffness (Young's Modulus) maps, which revealed alterations in the cytoskeletal organization of mutant cells (**Figure 30, S14**). In the case of M1 and M2 cells, highly aligned actin fibers were observed. These fibers are oriented parallel to the cell-cell junctions and display an increased stiffness compared to other regions of the cell body (**Figure 30**). Combined with the more pronounced spreading behavior, this alteration of the cytoskeletal organization might be considered as an indication for the formation of stronger cell-ECM contacts. The alignment of actin fibers may refer to an increased actomyosin contractility, which can lead to higher traction forces at the cell-ECM interface in the case of the mutant cells.

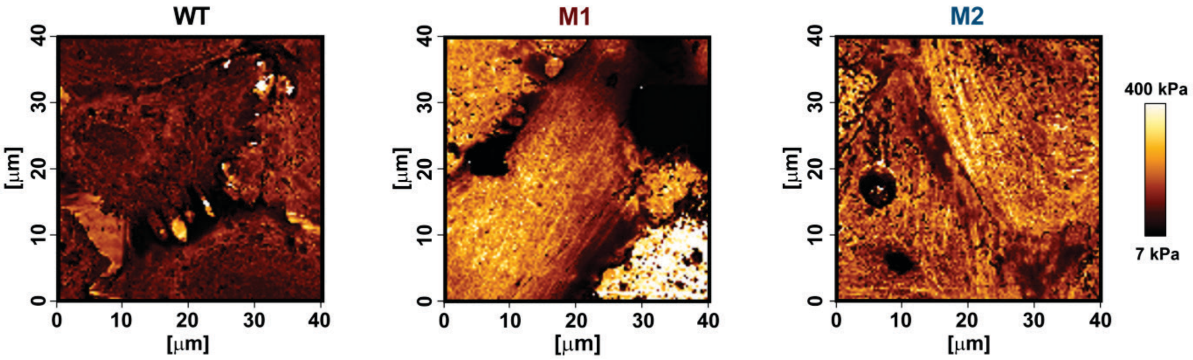

Figure 30. Representative stiffness (Young's Modulus) maps, showing the general features of the cytoskeletal organization for WT, M1 and M2 cells.

2.8.2 Time-dependent cell-adhesion experiments with endothelial cells carrying mutations linked to cell-adhesion and mechanotransduction

AFM-based QI measurements indicated changes in the morphology and the cytoskeletal architecture of endothelial cells carrying mutations linked to mechanotransduction pathways. The mutant cells were characterized by the formation of aligned actin fibers and showed enhanced spreading when compared to WT cells. To test the effect of these alterations on cell-ECM interactions and traction forces of endothelial cells, CC-based MFSs have been used with the purpose of observing cell adhesion behavior on surfaces functionalized with MFS of different stability. Furthermore, the adhesion behavior of WT endothelial cells was compared with the previously tested 3T3 fibroblasts.

The A_4B_4-MFS and A_5B_5-MFS designs were used to compare the magnitude of cell-ECM forces applied by the different cell types. The adhesion behavior of WT endothelial cells and 3T3 fibroblasts showed distinct differences. Both A_4B_4-MFS and A_5B_5-MFS were able to efficiently support cell attachment for WT endothelial cells during the first 120 min of cell adhesion (**Figure 31**). In contrast, A_4B_4-MFS failed to maintain the attachment of 3T3 fibroblasts after the first 30 min of adhesion, as shown in **Figure 28**. This simple comparison suggests that the magnitude of cell-ECM forces might vary depending on the cell type. This observation might be explained with existing knowledge about the cross-talk between cell-cell and cell-ECM adhesion in cells with endothelial lineage [165, 166]. Endothelial cells are known to generate strong cell-cell contacts via cadherin receptors, while cell-ECM interactions via integrin receptors are weakened when compared to other cell types. The strong endogenous tension exerted at cell-cell junctions has been shown to alter the distribution of traction forces at cell-cell and cell-ECM interfaces, and results in a decrease in cell-ECM forces. Therefore, the lower traction forces applied by the WT endothelial cells render both MFS systems durable enough for providing endothelial cell attachment during 120 min. At the same time, the stability of A_4B_4-MFS is insufficient to withstand higher cell-ECM forces as applied by 3T3 fibroblasts after the 30 min of initial cell adhesion.

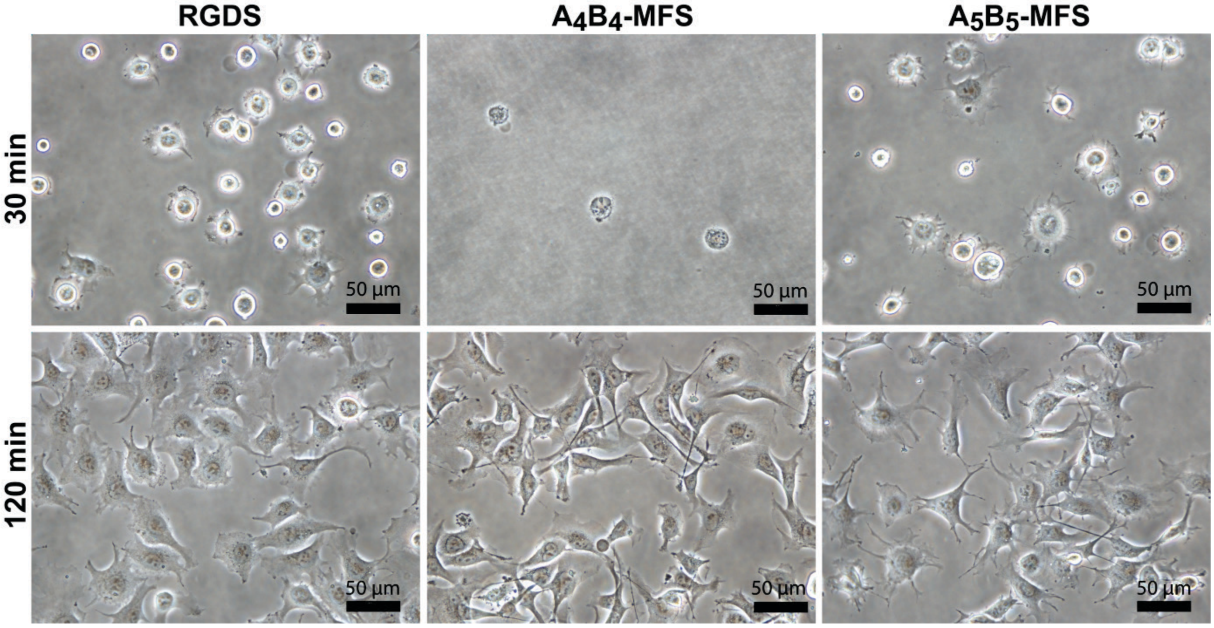

Figure 31. Phase-contrast images of WT endothelial cells on glass surfaces functionalized with RGDS, A_4B_4-MFS and A_5B_5-MFS. The images were taken after 30 min and 120 min of incubation. Scale bars: 50 µm.

This clear difference observed for 3T3 fibroblasts and WT endothelial cells demonstrates that the two different CC-based MFS prototypes tested are functional and allow for distinguishing alterations in cell-ECM forces. To test the adhesion behavior of M1 and M2 endothelial cells and to obtain insight into the effect of the mutations on cell-ECM interactions, they were grown on A_5B_5-MFS functionalized surfaces and compared to WT cells (**Figure 32, S17, S18**). In addition to the AFM height images, also the phase-contrast images show similar differences in the morphology and adhesion/spreading behavior of WT and mutant cells. Spindle like spreading behavior and long protrusions were observed for WT cells, while adhered M1 and M2 cells exhibited more of an isotropic spreading behavior with increased spreading areas. This comparison was only done for the mutant cells that were able to fully adhere on the functionalized surfaces without rupturing the force sensors. Adhesion of M1 cells was supported by the A_5B_5-MFS to a large extent. After 120 min, the density of attached cells was in the same range as for the WT cells. Yet, in case of the M1 cells, a mixture of fully adhered cells and detaching cells were observed at the 120 min time point, indicating that some of the cells were able to rupture the A_5B_5-MFS constructs. Furthermore, a significant decrease in the density of adhered cell was observed for M2 cells. These observations might be an evidence for the direct correlation between the altered cytoskeleton organization and the regulation of cell-ECM interactions. The formation of aligned actin fibers observed in mutant cells (**Figure 30, S14**) might indicate increased traction forces at FA sites.

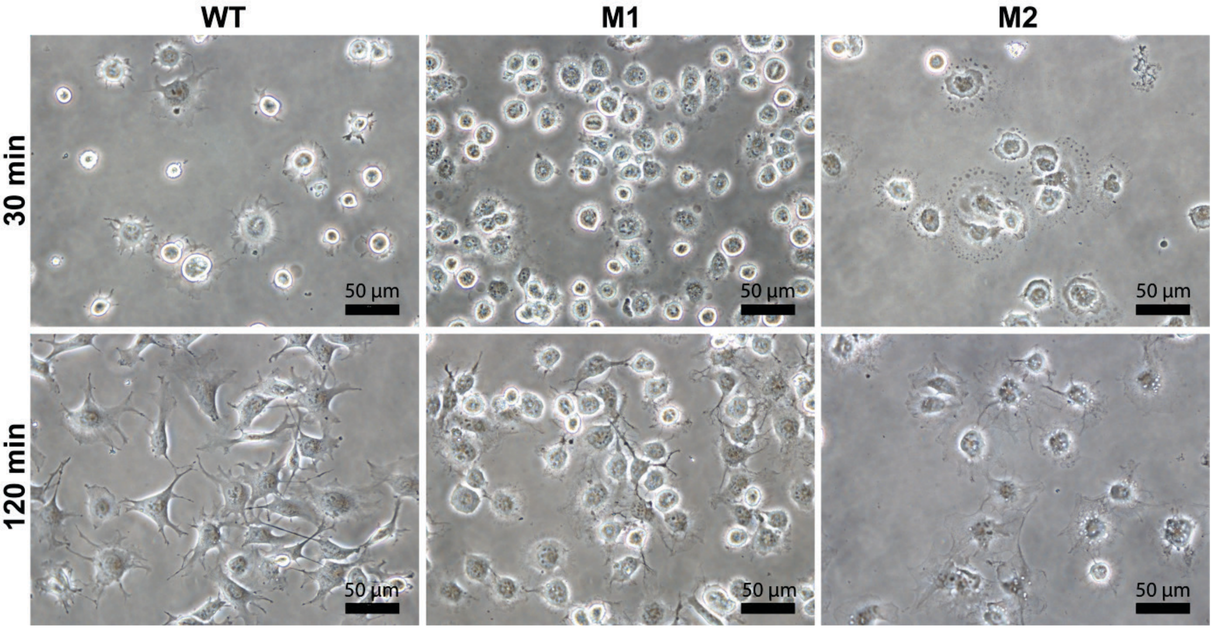

Figure 32. Phase-contrast images of WT and mutant endothelial cells (M1 and M2) on glass surfaces functionalized with A_5B_5-MFS. The images were taken after 30 min and 120 min of incubation. Scale bars: 50 μm.

3 Discussion

3.1 Length dependence and molecular mechanism of coiled coil rupture in the shear geometry

Considering the important role of CCs as structural building blocks in natural and synthetic molecular architectures, it is of fundamental importance to mechanistically understand the response of CCs to an externally applied force. Whereas a number of experimental and simulation studies have been performed where CCs were stretched parallel to the helical axis, this is the first report where the mechanical response of CCs to a defined shear force is observed experimentally. Making use of structurally related CCs of different length, this study shows that CC shearing is mechanistically complex, involving a dependence on both the applied strain and the loading rate. Just as for the tensile geometry, the initiation of helix uncoiling is observed at 15–25% strain (phase I → II transition; **Figure 18**). Even though this fundamental strain-dependent response appears to be present in both tensile and shear pulling geometries, crucial differences between the two geometries are also observed.

In the tensile geometry, all termini are fixed and the CC can only extend in the direction of the applied force. In contrast, the shear geometry allows a relative displacement of the coiled coil strands parallel to the helical axis. These additional degrees of freedom allow uncoiling-assisted sliding as well as uncoiling-assisted dissociation. These two strand-separation mechanisms compete with each other, with uncoiling-assisted dissociation being the dominant mechanism for short CCs (3-5 heptads) at experimentally relevant loading rates (**Figure 33**). It should be noted that structures with a different heptad register, as generated during sliding, are not stable for the CCs investigated here. The resulting structures would contain two asparagine–isoleucine pairings, which would destabilize the CC structure thermodynamically and kinetically. In this context, this work proposes that strand separation arising from uncoiling-assisted sliding requires longer CC sequences to contribute to strand separation at experimentally relevant timescales.

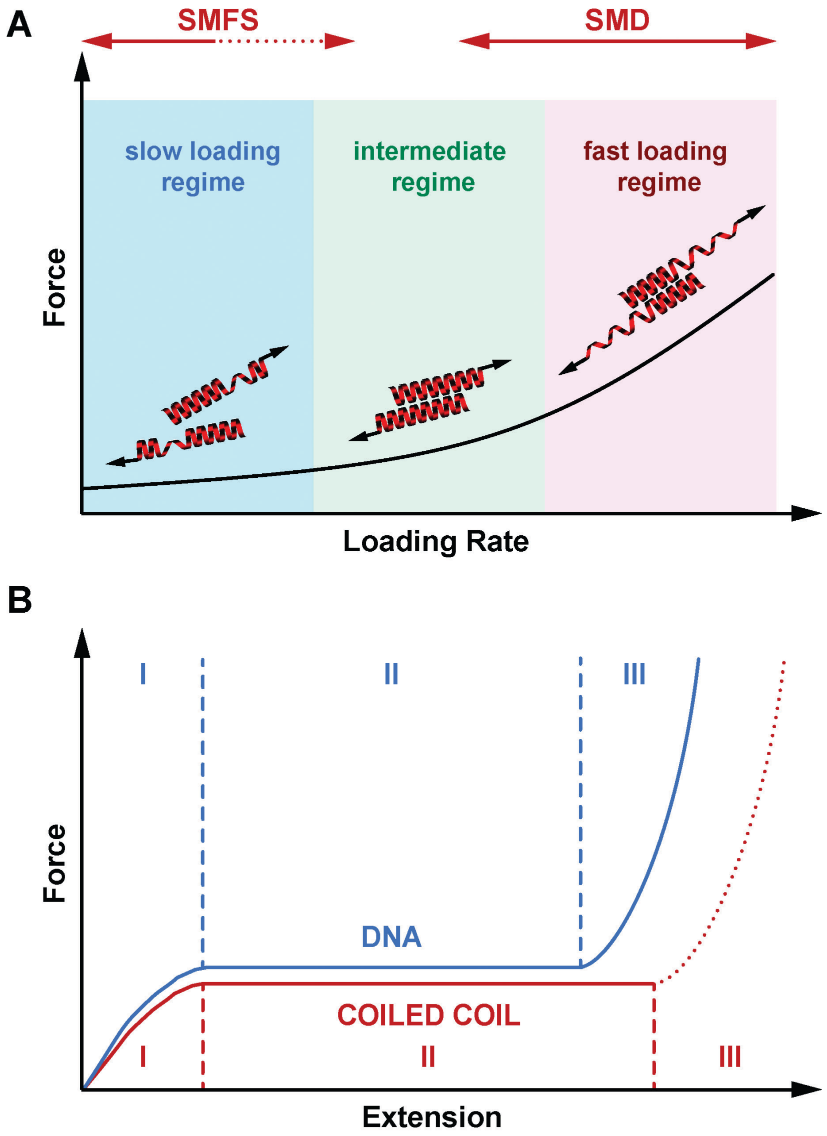

Figure 33. Mechanical response of coiled coils to shear forces. A) Loading rate-dependent response of CCs mechanically loaded in shear geometry. In the fast loading regime, accessible only in SMD simulations, helix uncoiling is initiated at the point of force application. Strand separation occurs via the propagation of helix uncoiling along the helical axis until all helical structure is lost. In the intermediate regime, where helix recoiling is possible, uncoiling-assisted sliding becomes the dominant mechanism. In the slow loading regime, uncoiling-assisted dissociation perpendicular to the force axis is facilitated once deformation has reached a critical magnitude. B) Comparison of mechanical DNA and CC unfolding as a function of extension. When stretched parallel to the helical axis, CCs show a universal, 3-phase response similar to the DNA overstretching transition. Phase III is always expected to occur for tensile geometries, where strand separation is prohibited. For the shear geometry, the existence of phase III is expected to depend on the thermodynamic stability of the molecule, as dissociation perpendicular to the force axis is always possible at any extension. For the CCs investigated here, phase III is not reached and strand separation occurs in phase I or II. (Reproduced with permission from ref. [118], copyright © Royal Society of Chemistry.)

In general, it can be assumed that the relative probability of these two strand separation mechanisms does not only depend on the loading rate, but is also affected by the CC length and sequence. CCs with a highly repetitive sequence may more easily undergo uncoiling-assisted sliding as also different heptad registers are possible. In natural CCs, which have a less defined hydrophobic core and charge pattern, alternative heptad registers may lead to highly unstable structures so that uncoiling-assisted sliding may not be observable. As mentioned above, the short CCs studied here dissociate after the uncoiling of a relatively small amount of helical structure. Longer CCs can tolerate larger amounts of uncoiling, while still being thermodynamically stable. This will increase the probability of uncoiling-assisted sliding, provided that the sequence of the CC allows alternative stable structures to exist. Interestingly, sliding has been proposed to be directly involved in the force transmission mechanism in the molecular motor protein dynein, which possesses a long dimeric CC [167-169], and may also be involved in allosteric signal propagation in other CC proteins [170]. It appears likely, that the sequence of natural CCs is fine-tuned to balance these possible response mechanisms to an applied shear force.

Besides understanding the fundamental mechanism of CC shearing, another key goal of this work was to compare the shear response to mechanical strand separation in the unzip geometry, as reported earlier for a number of natural CC sequences of different length. Unzipping also shows a force plateau (8–15 pN) [138, 147-149], which appears to be almost independent of CC length and overall sequence. The length independence suggests that the structure is unfolded in a turn-by-turn fashion and that strand separation occurs in equilibrium. Our results demonstrate that this is clearly not the case when the CCs are loaded in the shear geometry. In addition to the clear length dependence, the forces required for strand separation increase with the loading rate as predicted by the Bell–Evans model. This observed difference between the shear and unzip geometries is highly similar to the behavior of short, double stranded DNA mechanically loaded in either the shear [171, 172] or unzip geometry, even though a direct comparison is difficult. DNA consists of two tightly bound, linear strands wound into a helix. In contrast, the individual CC strands are helical and wrap around each other, forming a superhelix. Whereas DNA shearing proceeds via the rupture of interstrand base pairing interactions, CCs respond to the applied force by unfolding of individual helices, most likely before the first interstrand hydrophobic contacts and salt bridges are finally broken.

For DNA strand separation in equilibrium, it has been shown that the required work ($F \times x$) does not depend on the pulling geometry. On this basis, it can be directly explained why higher forces are required for strand separation in the shear geometry, where the length increase during strand separation is smaller [173-175]. For all CCs measured here, higher forces (~20–50 pN) in the shear geometry were detected than what was previously measured for the unzip geometry. An inverse dependence between the length increase and the magnitude of the force plateau could therefore also hold for CCs. Thus, a direct comparison with published unzipping forces cannot be performed. Considering the superhelical structure of the CC, however, we predict that this simple relationship may not be valid for CCs. When mechanically loaded in the unzip geometry, the individual helices are uncoiled at the same terminus. In contrast, in the shear geometry, each mechanically loaded terminus interacts with intact helical structure, experiencing a stabilizing effect. This hypothesis is supported by simulation results of higher order CC oligomers [141, 156], which show higher phase II plateau forces, even though the fundamental helix uncoiling mechanism was observed to be the same. It has further been shown that single helices are stabilized against mechanical uncoiling when interacting with a binding partner [159, 176].

Overall, this work has established that shearing occurs out of equilibrium and that the CC length can be used as a parameter for tuning the rupture force of CCs. With this new piece of information, it can be concluded that the mechanical response of CCs reproduces many of the essential features of DNA. When loaded in a shear or tensile geometry, CCs exhibit an unfolding transition (phase II), highly similar to the overstretching transition in DNA (**Figure 33B**) [133]. For short sequences (3–5 heptads), which rupture at forces below or just at the plateau force, dissociation is the dominant strand separation mechanism, so that length can be used as a parameter to tune the rupture force in experiments.

For long, natural CC sequences an α-helix to β-sheet transition has frequently been observed in phases II and III [155] and SMD simulations predict that this α–β transition should also occur in short CCs with a critical minimum length of 4-6 heptads, depending on the loading rate [145]. For the experimentally tested CCs, only a very small portion of force-extension curves obtained for the 5- and 6-heptad CCs showed an indication of a plateau region. For the 6-heptad long CC, preliminary evidence for the occurrence of a plateau phase and the α–β transition was found (increasing force in phase III). However, the noise level present in the experimental force-extension curves makes it difficult to distinguish the transition points between different phases and to analyze the obtained data with accuracy. At this point, further investigations into the structural details of the force plateau and the α–β transition are required. Considering the complexity of the overstretching transition of DNA, where strand separation at loose ends co-exists with melting bubble and S-DNA formation [173, 177-180], it will be highly interesting to determine the molecular parameters influencing the α–β transition in CCs. The CC model system introduced here represents an important starting point towards investigating the sequence–structure–mechanics relationship of coiled coils in a sequence-resolved fashion. This understanding is highly crucial for the further development of the CC-based MFS platform.

3.2 Coiled coil-based molecular force sensors for observing and quantifying mechanical processes at the cell-ECM interface

Integrins are the key force-sensing transmembrane proteins that build the primary molecular bridge between the ECM and intracellular mechanoresponsive proteins, including the cytoskeleton. Integrins bind to ECM ligands on the extracellular side while their intracellular domain is attached to actin filaments via several direct and indirect interactions, which involve adaptor proteins. As integrin-mediated FAs build up, mechanical signals are transmitted from the ECM to the intracellular site. This signal transmission includes a number of conformational changes that alter the biochemical signaling of the hierarchical FA assembly. The complex molecular architecture of FAs is held together by noncovalent interactions. Even though the strength of these interactions is either unknown or poorly characterized, it appears likely that their mechanical strength is higher than the strength of integrin-ECM bonds. These interactions must transmit mechanical forces without dissociating defining the integrin-ECM interaction as the weakest link in the chain [181].

Many efforts have been undertaken to determine the strength of integrin-ECM bonds and the magnitude of cell-applied forces acting at this interface. Early *in vitro* SCFS and SMFS measurements indicated a bond strength between ~13-109 pN for integrin-ECM interactions [36, 38, 182, 183], while DNA-based MFSs used for measuring the threshold force for cell-adhesion report forces in the range of ~33-56 pN [56]; however, the forces may exceed 56 pN, as no MFS with a higher rupture force was used in this experiment. Yet, no two-component MFS design is available, which allows for measuring higher forces and which spans the complete force range relevant for living cells. The most frequently used DNA-based

MFSs fail to cover this range and the DNA does not offer any flexibility to further extend the force range, as the dsDNA molecule undergoes an unfolding transition at ~65 pN.

In this work, CC-based MFSs were specifically designed and functionalized with a RGDS cell-adhesive ligand derived from the ECM protein fibronectin. This short sequence allows for measuring the threshold force of cell adhesion mediated through $\alpha_5\beta_1$ integrins. The CC-based MFSs tested here possess a dynamic force range of ~35-50 pN (A_4B_4-MFS) and ~30-40 pN (A_5B_5-MFS). They were able to support early cell adhesion of 3T3 fibroblasts, suggesting that the threshold force for initial adhesion is similar as determined with DNA-based force sensors. The CC-based MFSs used here do not extend the force range beyond of what is possible with the currently available DNA-based MFSs; however, they provide a number of possibilities for extending this range, such as the introduction of helix stabilizing non-natural modifications or the use of higher order oligomers.

One striking result is the observation that the CC-based MFS with the lower mechanical stability (A_5B_5-MFS) was able to promote a reasonable amount of cell attachment over 120 min. In contrast, the mechanically more, yet thermally less stable A_4B_4-MFS, failed to support cell attachment after the first 30 min of early adhesion. This key finding reveals that the thermodynamic stability needs to be considered when designing new MFS building blocks. The thermodynamic stability determines the lifetime of CC-based MFSs in the absence of force, i.e. its dissociation rate from the surface. MFSs with a low overall thermomechanical stability will therefore dissociate from the surface at a higher rate. As a result, the density of cell adhesive ligands will decrease faster than for MFSs with a high thermomechanical stability. When designing a series of MFSs, they should be designed such that all MFSs have a similar (or extremely high) thermodynamic stability. Only in this configuration will it be possible to assign the cell adhesion behavior to a purely mechanical effect.

Besides the effect of a combined thermomechanical stability, another crucially important point to keep in mind is that the mechanical calibration of the CC-based MFSs was performed within the loading rate limits accessible with the AFM. As explained before, the bond strength is a dynamic property that depends on the loading rate of the applied force. When using the CC-based MFSs, cell retraction thus determines the rate at which the CC heterodimer is mechanically loaded. Considering that little is known about the range of physiological loading rates, one must consider that the mechanical strength of the CC could be different from the calibrated values. Most likely the cell-applied loading rates are lower than the range tested in AFM-based SMFS, so that also the CC rupture forces are below the calibrated regime. This is a common problem for all available techniques used for determining cell-ECM forces at the single-molecule level. Yet, the CC-based MFSs presented here is the only system that is experimentally calibrated over a range of loading rates. This offers the possibility to estimate the bond strength at different loading rates.

Based on the measured k_{off} and Δx values, the Bell-Evans equation can be used to calculate the most probable rupture forces of the different CC-based MFSs for different loading rates and temperatures. It should be noted that the dynamic force range measured for the CCs in this work was determined at room temperature and within the experimentally accessible loading rate range from ~20-7500 pN s^{-1} (SMFS). A simple calculation can then be done for the cell culture temperature (37ºC) and the loading rates relevant for individual integrin-ECM bonds. This requires knowledge of the physiological loading rates acting on individual integrins; however, this information is not available and the magnitude of cell-generated loading rates has remained an open question. A crude estimate of the loading rates acting on a single integrin receptor has been done by Moore et al. [3]. This estimate is based on results obtained from traction force microscopy where time-dependent tractions forces were measured to be ~2-1250 pN $(s\cdot\mu m^2)^{-1}$ [52, 184, 185]. This value was then divided by the density of engaged integrins per area, which was considered to be 300 integrins per μm^2 [186-188]. Using these values, the loading rate that a single integrin experiences is predicted to lie in the range from ~0.007-4 pN s^{-1} [3].

When this regime of loading rates is considered for the estimation of the mechanical strength of CC-based MFSs at 37ºC, the range of most probable rupture forces spans from ~6-27 pN for A_4B_4-MFS and from ~11-24 pN for A_5B_5-MFS, indicating that A_5B_5-MFS may become more mechanically stable under cell culture conditions. Assuming that the ligand density is still sufficiently high at the 120 min time point, this simple calculation suggests that cell applied loading rates are in a regime where A_5B_5-MFS is more mechanically stable than A_4B_4-MFS. The crossover point for the mechanical stabilities of both MFSs lies at a loading rate of 0.334 pN s^{-1}, indicating that the cell applied loading rates are below this value. Unfortunately, it is not possible at this moment to distinguish the effects of the thermodynamic (ligand density after 120 min) and mechanical (MFS rupture) stability on cell adhesion. A fluorescent reporter system needs to be introduced in future experiments to monitor the ligand density during the experiment.

Altogether these results provide a viable means to address some crucial design principles for the development of protein-based MFSs, including the synergetic contribution of the thermal and mechanical stability (i.e. overall thermomechanical stability) of the molecular building blocks. Once the system is set up to account for the thermodynamic stability and to monitor the ligand density, the MFS system can be used to determine the loading rate range that cells employ to probe ECM mechanics. The CC heterodimers tested here represent the only fully mechanically calibrated building blocks among all MFS designs currently available. The first test of only two MFS candidates has shown that not only the calibrated force range, but also the k_{off} and Δx values are important additional design parameters that need to be considered when designing a CC-based MFS for a specific application where information about the loading rates is not available.

3.3 Using molecular force sensors for investigating integrin regulation and ECM interactions

Considering that all requirements for an ideal MFS platform are fulfilled, another important aspect to consider is the nature of integrin-ECM bonds. During the mechanosensing process, the force is detected and transmitted via conformational changes that may affect the binding affinity or the availability of ligand binding sites. As explained in Section 1.2.2., two interacting proteins possess a bound and an unbound state, separated by an energy barrier. The force required to break the interaction is considered as an energy input, which tilts the energy landscape, thereby reducing the activation energy required to switch to the unbound state. Considering a two-state system, interactions that show this behavior are defined as “slip bonds”. For a slip bond, the lifetime of the interaction is shortened under an externally applied force. Some interactions (e.g., selectin-ligand [189], actin-myosin [190] and glycoprotein-von Willebrand factor [191]), however, show a different behavior where the interaction strengthens when experiencing a certain magnitude of force. This type of an interaction is called a “catch bond” and recent studies have shown that integrin-ligand interactions may also comprise catch bond behavior. A possible occurrence of catch bond behavior between $\alpha_5\beta_1$ integrin and the ECM protein fibronectin has been detected and the bond life time is shown to be highest at forces between 10-30 pN [22]. This behavior is most likely involved in the regulation of mechanosensing during integrin-mediated adhesion and the force range overlaps with the mechanical strength of the MFSs used here.

It has been suggested that the $\alpha_5\beta_1$ integrin binds to fibronectin through two different sites: the RGD sequence and a so-called "synergy" site. The RGD sequence, found in the fibronectin III domain 10, is considered to be the key binding site for $\alpha_5\beta_1$ integrins [192]; however, a second binding site, composed of the PHSRN sequence in the fibronectin III domain 9, has also been found to contribute to $\alpha_5\beta_1$ integrin-adhesion [193, 194]. Although this site has no adhesive activity itself, its co-presence with the RGD sequence causes a 100-fold increase in cell adhesion to fibronectin [194, 195]. Based on obtained crystal structures, the RGD sequence interacts both with the α_5 and β_1 subunits, while the synergy site only binds to the head domain of the α_5 subunit [196]. Further protein and cell-based studies suggested different hypotheses for the possible contribution of this integrin-affinity regulation via the synergy site. One hypothesis is that the $\alpha_5\beta_1$ integrin-fibronectin bond can switch from a relaxed state to a tensed state when experiencing mechanical tension through the engagement of the synergy site [21]. The engagement of the synergy site increases the resistance of the $\alpha_5\beta_1$ integrin-fibronectin bond to shear forces, resulting in an increase in the integrin-ligand bond lifetime and adhesion strengthening. This hypothesis suggests an allosteric regulation of integrin-ligand affinity in the co-existence of the RGD and synergy sites, promoting catch bond behavior. Considering the specific interaction of the synergy site with the head domain of the α_1 subunit, it might be possible that upon binding to the synergy site the integrin heterodimer might experience the tension resulting in conformational changes to align the binding interface of the α and β subunits for the RGD motif, thereby increasing the ligand affinity and the lifetime of this specific bond. In the low affinity state, characterized by slip bond behavior, integrin legs are observed to have bent knees that are straightened upon activation. Thus, the tensile force generated upon the binding of the synergy site to the head domain of α_1 subunit might result in the straightening of integrin knees and trigger the switch from low to high affinity with long bond lifetimes [22]. In addition to this hypothesis, metal coordination is also considered to have an additional effect on the affinity regulation of integrin-ECM bonds. The α_5 subunit has been shown to bind to the RGD motif of fibronectin via the carboxylate group of the aspartate through intermolecular metal coordination [197]. In tension-free studies, Mn^{2+} alone has been shown to activate the high affinity state for RGD ligand binding [198, 199]. Thus, a second hypothesis suggests an initial activation of the high affinity state via metal coordination at low forces, which is then further strengthening upon synergy site binding due to the increased tension on integrin legs [21].

Considering these available models suggested for integrin affinity regulation and the recent discovery of a catch bond behavior for integrin-ligand interactions, the nature of the targeted cell-ECM bonds must be considered as an important criterion when designing a MFS system that aims at the detection of the threshold force for a certain type of integrin-ligand interaction. The CC-based MFS system tested here was designed for detecting the threshold force for the adhesion of 3T3 fibroblasts and endothelial cells via targeting the specific interaction between the $\alpha_5\beta_1$ integrin and the RGDS ligand derived from fibronectin. At this point, co-targeting the synergy site along with the RGDS ligand presented on the CC-based MFS unit may be of great importance for fully understanding the mechanical regulation of cell adhesion. For this purpose, the short PHSRN peptide could be added in solution or be co-immobilized on the surface. The system can be further tested in the presence and absence of metal ions. Such a system will be able to fully mimic the nature of $\alpha_5\beta_1$ integrin-mediated adhesion and force transduction. It can further be used for providing new insights into the physical mechanism of catch bond activation on mechanosensing at different forces and time-points. A protein based-MFS system capable of obtaining such an allosteric regulation mechanism would be an ideal system to study mechanosensing process at the single-molecule level, and might be used for regulating cellular behavior in a controlled manner when and where different adhesion strengths or threshold forces are desired for biological applications, such as in tissue engineering or regenerative medicine.

4 Conclusions

Using a combination of AFM-based SMFS and SMD simulations, this study investigated the mechanical response of CCs of different lengths to an applied shear force. The SMD simulations show that the force first rises almost linearly with extension, before reaching a plateau. The onset of this plateau phase correlates with the uncoiling of helical turns. Combining the SMFS and SMD results suggests that CC strand separation in shear geometry is non-cooperative and follows a hierarchy of timescales: helix uncoiling events are more frequent than sliding events, and sliding events are more frequent than dissociation events. In the simulations, strand separation occurred via uncoiling-assisted sliding in the direction of the applied external force. Dissociation perpendicular to the force axis was not observed, suggesting that its intrinsic timescale is much longer than the simulation timescale. Even though strand separation via sliding cannot be fully excluded in the experiments, it appears unlikely for the relatively short CCs investigated here. For longer CCs, uncoiling-assisted sliding and dissociation most likely coexist and compete with each other, with a different relative contribution of both mechanisms at different loading rates.

From an application point of view, it has been shown that the rupture forces of short dimeric CCs are sensitive to the CC length, when mechanically loaded in the shear geometry. The results presented in this work serve as an important starting point for future experiments aimed at tuning the mechanical stability of CCs. Strand separation via sliding or dissociation is initiated by helix uncoiling, which implies that altering helix stability will directly affect the structural response of CCs to shear forces. This may be achieved by introducing helix (de)stabilizing mutations or when using higher order oligomers. With these strategies, a CC library that covers a broader force range can be designed and used to extend MFS applications.

Together with the SMFS results, the proof-of-concept cell culture experiments highlight the application potential of CCs as molecular building blocks for protein-based MFSs. The simple design of CCs, along with the capability of mimicking natural ECM proteins with mechanical function, makes CC-based MFSs an ideal platform. This platform provides the possibility of introducing different cell-adhesive ligands in a straightforward synthetic procedure and of tuning the mechanical stability. Combined with different pulling geometries and higher oligomerization states, such as trimeric or tetrameric CC structures, a large range of rupture forces can possibly be obtained so that CCs have the potential to replace DNA oligonucleotides as nanomechanical building blocks in applications where protein-based structures are desired. Their application range is not limited to MFSs [18, 55, 56] and may, for example, be extended to mechanoresponsive material crosslinks [18, 132, 200]. The incorporation of a Förster resonance energy transfer (FRET) reporter system into the prototype presented here, will make CC-based MFSs equally powerful optical reporters as DNA-based tension probes.

Despite recent advances in the development of MFSs for detecting cell-ECM forces with an optical readout at the single-molecule level, many pieces of the puzzle are still missing. The possibility of integrating FRET-coupled CC-based MFSs into a polymeric hydrogel (e.g., PEG, PAA, etc.) or ideally a fully protein-based ECM mimic with controllable stiffness will yield a new generation single-molecule force-sensing technique with the capability of substituting available techniques that fail to mimic the natural extracellular environment. Tunable protein-based MFSs, such as the design introduced in this work, will clearly aid in reaching closer to a full understanding of the molecular pathways for force transmission and rigidity sensing in FAs and reveal the details of the concerted signaling that links intracellular and extracellular mechanosensing processes.

5 Materials and Methods

5.1 Peptides

All CC-forming peptides used in this work were synthesized using standard solid phase peptide synthesis (SPPS) protocols and obtained from commercial suppliers (Centic Biotec, Germany; Pepscan, The Netherlands; Proteogenix, France). The peptides were dissolved in coupling buffer (50 mM sodium phosphate pH 7.2 @ 4ºC, 50 mM NaCl, 10 mM EDTA) at a concentration of 2 mM. The peptide stock solutions were aliquoted and stored at −20ºC. For the SMFS experiments, a cysteine was introduced during SPPS at the respective terminus. Peptides without cysteine were used for CD spectroscopy to determine the secondary structure and the thermal stability of the CCs. For the cell culture experiments, a cell-adhesive peptide sequence (RGDS) was introduced after a short linker sequence (GGG) to the C-termini of the B_4 and B_5 peptides.

5.2 CD spectroscopy of the coiled coils and the corresponding PEG conjugates

The individual cysteine-free peptides were diluted to a concentration of 100 µM in phosphate buffered saline (PBS; 10 mM Na_2HPO_4, 1.8 mM KH_2PO_4, 137 mM NaCl, 2.7 mM KCl, pH 7.4) and subsequently mixed in a 1:1 ratio to form the heterodimers. To determine a possible effect of the PEG linker on the secondary structure and the thermal stability of the CCs, PEG conjugates were investigated in addition. For this purpose, methoxy-PEG-maleimide (MW = 10000 g mol^{-1}; Rapp Polymere, Germany) was reacted with the individual cysteine-containing peptides in an 1:1 ratio (20ºC, 300 rpm, 15 min) prior to mixing of the two peptides.

CD spectra and thermal denaturation curves were recorded in 1 mm quartz cuvettes (Hellma Analytics, Germany) using a Chirascan CD spectrometer (Applied Photophysics, UK) equipped with a Peltier temperature controller. For the CD spectra, the samples were measured at 20ºC, using the following settings: 0.7 s time-per-point, 1 nm step size and 1 nm bandwidth. Thermal denaturation experiments were performed under the same conditions, heating the samples from 5 to 90ºC at a rate of 1ºC min^{-1}. The CD signal at 222 nm was recorded using the same settings. The melting temperature T_m was determined from the second derivative (i.e., the change point) of the thermal denaturation curves. Each measurement was performed in triplicate unless stated differently. The errors given represent the standard error of the mean (SEM).

5.3 Preparation of glass slides and cantilevers for the AFM measurements

The cysteine-terminated peptides were immobilized to glass slides and AFM cantilevers via PEG spacers, using a previously established protocol [151]. The A peptide was immobilized to the glass slide, whereas the B peptide was immobilized to the cantilever. In detail, commercially available, amino-functionalized glass slides (Slide A, Nexterion, Germany) were used as amino-functionalized substrates. The cantilevers (MLCT, Bruker, Germany) were activated via 10 min UV-ozone cleaning and amino-modified using 3-aminopropyl dimethylethoxy silane (ABCR, Germany). For the following steps, both glass slides and cantilevers were treated in parallel. Both surfaces were incubated in 50 mM sodium borate (pH 8.5) to increase the fraction of deprotonated amino groups for the subsequent coupling of the heterobifunctional NHS-PEG-maleimide spacer (MW = 10000 g mol^{-1}; Rapp Polymere). NHS-PEG-maleimide was dissolved in a concentration of 50 mM in sodium borate and incubated on the surfaces for 1 h. Following incubation, the surfaces were washed with ultrapure water and dried under nitrogen flow. The B peptide (300 µM in coupling buffer) was pipetted onto the cantilevers and incubated on the surface for 1 h at 4ºC. In parallel, a 1 mM solution of the A peptide was incubated on the glass slides. After incubation, the surfaces were rinsed with PBS to remove non-covalently bound peptides and stored in PBS until use.

5.4 Fluorescence analysis to verify the site-specific immobilization of coiled coil heterodimers

A fluorescence experiment was carried out to verify the site-specific immobilization of CC peptides. For the coupling of the peptides to the glass surface, the same immobilization chemistry was used. A concentration series (from 0.675 to 20 µM) of the B_4 peptide was spotted on the maleimide-functionalized glass slide and incubated for 1 h at 4ºC in a humid chamber. The spots were then removed by aspiration and the slide was washed with PBS 3 times. Subsequently, the slide was incubated in a solution containing the fluorescently labelled A_4 peptide (tetramethylrhodamine coupled to the N-terminus of A_4; Rho-A_4). For this purpose, Rho-A_4 was dissolved at a concentration of 10 µM in PBS containing 0.5% w/v bovine serum albumin (BSA). Incubation was performed under shaking for 1 h at room temperature. To prove the heterospecificity of the complementary peptide couple, peptide A_4 was also immobilized on the same surface. In addition, peptide B_4 was mixed with an excess of free cysteine (45 mM) to block the reaction of this peptide with the maleimide-functionalized surface. After the incubation, the slide was washed 3 times with PBS + 0.5% BSA and dried under N_2. A Spot Scout-Pro micro-array scanner (Ditabis AG, Germany) was used to visualize the fluorescence signal.

5.5 Single-molecule force spectroscopy

All SMFS measurements were performed with a ForceRobot® 300 instrument (JPK Instruments, Germany) at room temperature in PBS. Cantilever C with a nominal spring constant of 0.01 N m^{-1} was used for all measurements. Each cantilever was calibrated using the thermal noise method and the spring constants determined varied between 0.016–0.023 N m^{-1}. During each experiment, the approach and retract speeds were held constant, and the applied force was adjusted by changing the distance between the tip and the surface. For each sample, several hundreds of approach–retract cycles were carried out on a 10 × 10 μm^2 grid. To obtain measurements over a broad range of different loading rates, several experiments were performed, each at a different retract speed ranging from 50 to 5000 nm s^{-1}. For all three CCs, these dynamic SMFS measurements were carried out in three independent experiments, using different cantilevers and glass slides for every experiment.

The obtained data was converted into force–extension curves using the JPK data analysis program. The CCs were coupled to the surface and the cantilever via PEG spacers with a length of approx. 80 nm each (MW = 10000 g mol^{-1}). PEG represents an ideal spacer for SMFS measurements. It prevents non-specific binding and possesses a characteristic force–extension behavior, which can be described with the worm-like chain model (WLC; **Equation 3**) at forces below 100 pN [201].

$$f(z) = \left(\frac{k_\mathrm{B}T}{p}\right)\left[\frac{1}{4\,(1-z/L)^2} - \frac{1}{4} + \frac{z}{L}\right] \qquad (3)$$

where $f(z)$ is the force at an end-to-end distance of z, p is the persistence length, k_B is the Boltzmann constant, T is the absolute temperature, and L is the contour length of the polymer (PEG) being stretched.

All force extension curves were fitted with the WLC model. Only force–extension curves that were fitted well (visual inspection) and possessed a contour length >100 nm were used for further analysis. For the selected force–extension curves the rupture forces and the corresponding loading rates were determined using the JPK data analysis program. For each retract speed, the rupture forces and the corresponding loading rates were plotted into histograms. All rupture force and loading rate (plotted logarithmically) histograms were fitted with a Gaussian distribution to determine the maxima, which represent the most probable rupture force F and the most probable loading rate, respectively. The most probable rupture forces were plotted against the most probable loading rates and the data was fitted with the Bell–Evans model (**Equation 2**).

$$F = \frac{k_BT}{\Delta X} \cdot ln\left(\frac{\dot{F}}{k_{off}} \cdot \frac{\Delta x}{k_BT}\right) \qquad (2)$$

where k_B is the Boltzmann constant, T the temperature, Δx the potential width, k_off the force-free dissociation rate at zero force, and $\dot{F}$, equal to $\mathrm{d}F/\mathrm{d}t$, is the loading rate.

Fitting the F vs. ln $\dot{F}$ plot to **Equation 2**, yields k_off and Δx of the CC interaction. Each data set obtained from one cantilever was fitted separately. For every CC, 3 independent experiments were performed using different cantilevers and surfaces. Each data set was fitted independently with the Bell-Evans model to obtain the corresponding $k_\mathrm{off\_SMFS}$ and Δx_SMFS values. Using these values, the mean ± SEM were determined.

5.6 Preparation of glass coverslips functionalized with coiled coil-based molecular force sensors

To functionalize glass coverslips with CC-based MFSs, the same coupling chemistry was used as described for the SMFS experiments. Briefly, glass coverslips were first amino-functionalized with monoreactive 3-aminopropyl dimethyl ethoxysilane. Thereafter, the hetero-bifunctional NHS-PEG-maleimide was coupled to the surface through the amino-reactive NHS groups. Subsequently, the peptide carrying a Cys residue (A_4 or A_5 peptide) was coupled to the PEG surface displaying the thiol-reactive maleimide groups. Spots of A peptides (500 µM) were created on the surface with a volume of 5 µL per spot and incubated for 1 h at 4ºC. The drops were removed from the surface via aspiration and the coverslips were washed with PBS twice. Following the washing step, the coverslips were dried under N_2. Drops of the complementary Cys-free B peptides, carrying the cell-adhesive RGDS ligand (B_4-RGDS or B_5-RGDS; 500 µM), were created in the A peptide-functionalized areas and incubated for 20 min at 4ºC. The coverslips were then gently washed with PBS and dried by tilting the coverslip and allowing the PBS solution to roll off the surface. The MFS-functionalized coverslips were immediately used for cell culture experiments.

5.7 Cell culture

NIH/3T3 fibroblasts were maintained and expanded in Dulbecco's Modified Eagle Medium (DMEM) (ThermoFisher, Germany) supplemented with 5% fetal calf serum (FCS) (Biochrom GmbH, Germany), 2 mM L-glutamine (PAN-Biotech GmbH, Germany) and 100 units mL^{-1} penicillin, 10 µg mL^{-1} streptomycin (PAA-laboratories GmbH, Germany), at 37ºC and 5% CO_2 atmosphere. The endothelial cells were maintained and expanded in M199 medium (Sigma-Aldrich, Germany) supplemented with 20% FCS (Biochrom GmbH, Germany), 2 mM L-glutamine (PAN-Biotech GmbH), 100 units mL^{-1} penicillin, 10 µg mL^{-1} streptomycin (PAA-laboratories), 25 µg mL^{-1} Heparin (Sigma-Aldrich) and 50 µg mL^{-1} endothelial cell growth supplement (Corning, NY, USA) herein referred to as M199 basal growth medium, at 37ºC and 5% CO_2 atmosphere. For maintenance and expansion, cells were seeded on polystyrene petri dishes (VWR International GmbH, Germany) and the cells reaching to confluency were splitted using Trypsin (PAN-Biotech GmbH) in 4 day intervals after seeding.

5.8 Quantitative imaging via atomic force microscopy

Quantitative imaging (QI) was performed using a NanoWizard® 3 AFM (JPK Instruments), mounted on an IX71 inverted phase-contrast microscope (Olympus, Germany). Silicon cantilevers (qp-BioAC, Nanosensors^{TM}, Switzerland) were used for QI. Imaging was performed with the longest probe (CB3: 80 µm), possessing a nominal spring constant of 0.06 N m^{-1}. Prior to imaging, calibration was performed using the thermal noise method, after obtaining the deflection sensitivity of the cantilever by pressing the AFM tip against a hard reference substrate (glass). The actual spring constants ranged from 0.06-0.09 N m^{-1}.

All measurements were conducted on cell monolayers cultured on glass-bottom petri dishes (MatTek Corporation, USA). The cells were cultured for 48 hours after seeding to reach the desired confluency. Prior to imaging, cells were fixed in 1.25% glutaraldehyde solution for 2 min. During imaging, the samples were kept hydrated in PBS and all measurements were performed at room temperature. Arrays of force-extension curves were automatically collected in QI mode with an applied load of 2 nN at a constant velocity of 50 µm s^{-1}. Data was collected on a selected grid size of 128 × 128 pixels, distributed over an area of 40 × 40 µm^2 scan size. JPK SPM data processing software (JPK Instruments) was used for obtaining the height profiles and for fitting each individual force-extension curve. The resulting data was used for constructing stiffness maps, which display the Young's modulus at each point of the grid. For fitting, the retract segments of the collected force-extension curves were batch-analyzed, using the Hertz/Sneddon fit function (conical indenter) and a Poisson ratio of 0.5.

5.9 Time-dependent cell adhesion experiments

For cell adhesion experiments, the Cys-free B peptide sequences were extended with a cell-adhesive ligand to allow cell attachment to the MFSs. The short, cell-adhesive peptide sequence RGDS, derived from the ECM protein fibronectin, was incorporated at the C-termini of the B_4 and B_5 peptide sequences. Cell adhesion experiments were performed with NIH/3T3 fibroblasts and endothelial cells for different incubation times. During the adhesion experiments, FCS-free DMEM (ThermoFisher) supplemented with 2 mM L-glutamine (PAN-Biotech GmbH), 100 units mL^{-1} penicillin, 10 µg mL^{-1} streptomycin (PAA-laboratories) and

FCS-free M199 (PAN Biotech GmbH) medium supplemented with 2 mM L-glutamine (PAN-Biotech GmbH), 100 units mL^{-1} penicillin, 10 µg mL^{-1} streptomycin (PAA-laboratories) were used for 3T3 fibroblasts and endothelial cells, respectively. Suspended fibroblasts and endothelial cells were plated on surfaces (5×10^5 cells mL^{-1}) functionalized with A_4B_4-MFS and A_5B_5-MFS and were incubated for 15 min, 30 min, 60 min and 120 min before gentle washing with PBS and fixed with 4% paraformaldehyde for 10 min. Phase contrast imaging (Nikon Eclipse TS100, Nikon GmbH, Germany) was used to observe the adhesion behavior of the cells after different time points of incubation on the functionalized surface.

References

1. Dufrene, Y.F., E. Evans, A. Engel, J. Helenius, H.E. Gaub, and D.J. Muller, *Five challenges to bringing single-molecule force spectroscopy into living cells.* Nat Methods, 2011. **8**: 123-127.
2. Brown, A.E. and D.E. Discher, *Conformational changes and signaling in cell and matrix physics.* Curr Biol, 2009. **19**: R781-789.
3. Moore, S.W., P. Roca-Cusachs, and M.P. Sheetz, *Stretchy proteins on stretchy substrates: the important elements of integrin-mediated rigidity sensing.* Dev Cell, 2010. **19**: 194-206.
4. Evans, E.A. and D.A. Calderwood, *Forces and bond dynamics in cell adhesion.* Science, 2007. **316**: 1148-1153.
5. Sheetz, M.P., D.P. Felsenfeld, and C.G. Galbraith, *Cell migration: regulation of force on extracellular-matrix-integrin complexes.* Trends Cell Biol, 1998. **8**: 51-54.
6. Garcia, A.J., M.D. Vega, and D. Boettiger, *Modulation of cell proliferation and differentiation through substrate-dependent changes in fibronectin conformation.* Mol Biol Cell, 1999. **10**: 785-798.
7. Engler, A.J., S. Sen, H.L. Sweeney, and D.E. Discher, *Matrix elasticity directs stem cell lineage specification.* Cell, 2006. **126**: 677-689.
8. Humphries, J.D., N.R. Paul, M.J. Humphries, and M.R. Morgan, *Emerging properties of adhesion complexes: what are they and what do they do?* Trends Cell Biol, 2015. **25**: 388-397.
9. LaCroix, A.S., K.E. Rothenberg, and B.D. Hoffman, *Molecular-Scale Tools for Studying Mechanotransduction.* Annu Rev Biomed Eng, 2015. **17**: 287-316.
10. Jaalouk, D.E. and J. Lammerding, *Mechanotransduction gone awry.* Nat Rev Mol Cell Biol, 2009. **10**: 63-73.
11. Hynes, R.O., *Integrins: bidirectional, allosteric signaling machines.* Cell, 2002. **110**: 673-687.
12. Geiger, B., J.P. Spatz, and A.D. Bershadsky, *Environmental sensing through focal adhesions.* Nat Rev Mol Cell Biol, 2009. **10**: 21-33.
13. Case, L.B. and C.M. Waterman, *Integration of actin dynamics and cell adhesion by a three-dimensional, mechanosensitive molecular clutch.* Nat Cell Biol, 2015. **17**: 955-963.
14. Takada, Y., X. Ye, and S. Simon, *The integrins.* Genome Biol, 2007. **8**: 215.
15. Vicente-Manzanares, M., C.K. Choi, and A.R. Horwitz, *Integrins in cell migration--the actin connection.* J Cell Sci, 2009. **122**: 199-206.
16. Humphries, J.D., A. Byron, and M.J. Humphries, *Integrin ligands at a glance.* J Cell Sci, 2006. **119**: 3901-3903.
17. Barczyk, M., S. Carracedo, and D. Gullberg, *Integrins.* Cell Tissue Res, 2010. **339**: 269-280.
18. Goktas, M. and K.G. Blank, *Molecular Force Sensors: From Fundamental Concepts toward Applications in Cell Biology.* Adv Mater Interfaces, 2017. **4**: 1600441.

19. del Rio, A., R. Perez-Jimenez, R. Liu, P. Roca-Cusachs, J.M. Fernandez, and M.P. Sheetz, *Stretching single talin rod molecules activates vinculin binding.* Science, 2009. **323**: 638-641.
20. Livne, A. and B. Geiger, *The inner workings of stress fibers - from contractile machinery to focal adhesions and back.* J Cell Sci, 2016. **129**: 1293-1304.
21. Friedland, J.C., M.H. Lee, and D. Boettiger, *Mechanically activated integrin switch controls alpha5beta1 function.* Science, 2009. **323**: 642-644.
22. Kong, F., A.J. Garcia, A.P. Mould, M.J. Humphries, and C. Zhu, *Demonstration of catch bonds between an integrin and its ligand.* J Cell Biol, 2009. **185**: 1275-1284.
23. Evans, E.A., R. Waugh, and L. Melnik, *Elastic area compressibility modulus of red cell membrane.* Biophys J, 1976. **16**: 585-595.
24. Evans, E., K. Ritchie, and R. Merkel, *Sensitive force technique to probe molecular adhesion and structural linkages at biological interfaces.* Biophys J, 1995. **68**: 2580-2587.
25. Wang, N., J.P. Butler, and D.E. Ingber, *Mechanotransduction across the cell surface and through the cytoskeleton.* Science, 1993. **260**: 1124-1127.
26. Walter, N., C. Selhuber, H. Kessler, and J.P. Spatz, *Cellular unbinding forces of initial adhesion processes on nanopatterned surfaces probed with magnetic tweezers.* Nano Lett, 2006. **6**: 398-402.
27. Tanase, M., N. Biais, and M. Sheetz, *Magnetic tweezers in cell biology.* Methods Cell Biol, 2007. **83**: 473-493.
28. Honarmandi, P., H. Lee, M.J. Lang, and R.D. Kamm, *A microfluidic system with optical laser tweezers to study mechanotransduction and focal adhesion recruitment.* Lab Chip, 2011. **11**: 684-694.
29. Romero, S., A. Quatela, T. Bornschlogl, S. Guadagnini, P. Bassereau, and G. Tran Van Nhieu, *Filopodium retraction is controlled by adhesion to its tip.* J Cell Sci, 2012. **125**: 4999-5004.
30. Helenius, J., C.P. Heisenberg, H.E. Gaub, and D.J. Muller, *Single-cell force spectroscopy.* J Cell Sci, 2008. **121**: 1785-1791.
31. Taubenberger, A.V., D.W. Hutmacher, and D.J. Muller, *Single-cell force spectroscopy, an emerging tool to quantify cell adhesion to biomaterials.* Tissue Eng Part B Rev, 2014. **20**: 40-55.
32. Friedrichs, J., K.R. Legate, R. Schubert, M. Bharadwaj, C. Werner, D.J. Muller, and M. Benoit, *A practical guide to quantify cell adhesion using single-cell force spectroscopy.* Methods, 2013. **60**: 169-178.
33. Haase, K. and A.E. Pelling, *Investigating cell mechanics with atomic force microscopy.* J R Soc Interface, 2015. **12**: 20140970.
34. Benoit, M., D. Gabriel, G. Gerisch, and H.E. Gaub, *Discrete interactions in cell adhesion measured by single-molecule force spectroscopy.* Nat Cell Biol, 2000. **2**: 313-317.
35. Taubenberger, A., D.A. Cisneros, J. Friedrichs, P.H. Puech, D.J. Muller, and C.M. Franz, *Revealing early steps of alpha2beta1 integrin-mediated adhesion to collagen type I by using single-cell force spectroscopy.* Mol Biol Cell, 2007. **18**: 1634-1644.

36. Li, F., S.D. Redick, H.P. Erickson, and V.T. Moy, *Force measurements of the alpha5beta1 integrin-fibronectin interaction.* Biophys J, 2003. **84**: 1252-1262.
37. Zhang, X., S.E. Craig, H. Kirby, M.J. Humphries, and V.T. Moy, *Molecular basis for the dynamic strength of the integrin alpha4beta1/VCAM-1 interaction.* Biophys J, 2004. **87**: 3470-3478.
38. Kokkoli, E., S.E. Ochsenhirt, and M. Tirrell, *Collective and single-molecule interactions of alpha5beta1 integrins.* Langmuir, 2004. **20**: 2397-2404.
39. Litvinov, R.I., J.S. Bennett, J.W. Weisel, and H. Shuman, *Multi-step fibrinogen binding to the integrin (alpha)IIb(beta)3 detected using force spectroscopy.* Biophys J, 2005. **89**: 2824-2834.
40. Muller, D.J., J. Helenius, D. Alsteens, and Y.F. Dufrene, *Force probing surfaces of living cells to molecular resolution.* Nat Chem Biol, 2009. **5**: 383-390.
41. Owen, R.J., C.D. Heyes, D. Knebel, C. Rocker, and G.U. Nienhaus, *An integrated instrumental setup for the combination of atomic force microscopy with optical spectroscopy.* Biopolymers, 2006. **82**: 410-414.
42. Jacobs, M.J. and K. Blank, *Joining forces: integrating the mechanical and optical single molecule toolkits.* Chem Sci, 2014. **5**: 1680-1697.
43. Polacheck, W.J. and C.S. Chen, *Measuring cell-generated forces: a guide to the available tools.* Nat Methods, 2016. **13**: 415-423.
44. Harris, A.K., P. Wild, and D. Stopak, *Silicone rubber substrata: a new wrinkle in the study of cell locomotion.* Science, 1980. **208**: 177-179.
45. Lee, J., M. Leonard, T. Oliver, A. Ishihara, and K. Jacobson, *Traction forces generated by locomoting keratocytes.* J Cell Biol, 1994. **127**: 1957-1964.
46. Dembo, M. and Y.L. Wang, *Stresses at the cell-to-substrate interface during locomotion of fibroblasts.* Biophys J, 1999. **76**: 2307-2316.
47. Beningo, K.A., M. Dembo, I. Kaverina, J.V. Small, and Y.L. Wang, *Nascent focal adhesions are responsible for the generation of strong propulsive forces in migrating fibroblasts.* J Cell Biol, 2001. **153**: 881-888.
48. Maskarinec, S.A., C. Franck, D.A. Tirrell, and G. Ravichandran, *Quantifying cellular traction forces in three dimensions.* Proc Natl Acad Sci U S A, 2009. **106**: 22108-22113.
49. Legant, W.R., J.S. Miller, B.L. Blakely, D.M. Cohen, G.M. Genin, and C.S. Chen, *Measurement of mechanical tractions exerted by cells in three-dimensional matrices.* Nat Methods, 2010. **7**: 969-971.
50. Pelham, R.J., Jr. and Y. Wang, *Cell locomotion and focal adhesions are regulated by substrate flexibility.* Proc Natl Acad Sci U S A, 1997. **94**: 13661-13665.
51. Khetan, S., M. Guvendiren, W.R. Legant, D.M. Cohen, C.S. Chen, and J.A. Burdick, *Degradation-mediated cellular traction directs stem cell fate in covalently crosslinked three-dimensional hydrogels.* Nat Mater, 2013. **12**: 458-465.
52. Tan, J.L., J. Tien, D.M. Pirone, D.S. Gray, K. Bhadriraju, and C.S. Chen, *Cells lying on a bed of microneedles: an approach to isolate mechanical force.* Proc Natl Acad Sci U S A, 2003. **100**: 1484-1489.
53. Trichet, L., J. Le Digabel, R.J. Hawkins, S.R. Vedula, M. Gupta, C. Ribrault, P. Hersen, R. Voituriez, and B. Ladoux, *Evidence of a large-scale mechanosensing*

mechanism for cellular adaptation to substrate stiffness. Proc Natl Acad Sci U S A, 2012. **109**: 6933-6938.

54. Balaban, N.Q., U.S. Schwarz, D. Riveline, P. Goichberg, G. Tzur, I. Sabanay, D. Mahalu, S. Safran, A. Bershadsky, L. Addadi, and B. Geiger, *Force and focal adhesion assembly: a close relationship studied using elastic micropatterned substrates.* Nat Cell Biol, 2001. **3**: 466-472.
55. Albrecht, C., K. Blank, M. Lalic-Multhaler, S. Hirler, T. Mai, I. Gilbert, S. Schiffmann, T. Bayer, H. Clausen-Schaumann, and H.E. Gaub, *DNA: a programmable force sensor.* Science, 2003. **301**: 367-370.
56. Wang, X. and T. Ha, *Defining single molecular forces required to activate integrin and notch signaling.* Science, 2013. **340**: 991-994.
57. de Gennes, P.G., *Maximum pull out force on DNA hybrids.* C R Acad Sci Ser IV: Phys., Astrophys, 2001. **2**: **1505-15508**.
58. Wang, X., J. Sun, Q. Xu, F. Chowdhury, M. Roein-Peikar, Y. Wang, and T. Ha, *Integrin Molecular Tension within Motile Focal Adhesions.* Biophys J, 2015. **109**: 2259-2267.
59. Roein-Peikar, M., Q. Xu, X.F. Wang, and T. Ha, *Ultrasensitivity of Cell Adhesion to the Presence of Mechanically Strong Ligands.* Phys Rev X, 2016. **6**.
60. Chowdhury, F., I.T. Li, T.T. Ngo, B.J. Leslie, B.C. Kim, J.E. Sokoloski, E. Weiland, X. Wang, Y.R. Chemla, T.M. Lohman, and T. Ha, *Defining Single Molecular Forces Required for Notch Activation Using Nano Yoyo.* Nano Lett, 2016. **16**: 3892-3897.
61. Wan, Z., X. Chen, H. Chen, Q. Ji, Y. Chen, J. Wang, Y. Cao, F. Wang, J. Lou, Z. Tang, and W. Liu, *The activation of IgM- or isotype-switched IgG- and IgE-BCR exhibits distinct mechanical force sensitivity and threshold.* Elife, 2015. **4**: e06925.
62. Liu, Y., L. Blanchfield, V.P. Ma, R. Andargachew, K. Galior, Z. Liu, B. Evavold, and K. Salaita, *DNA-based nanoparticle tension sensors reveal that T-cell receptors transmit defined pN forces to their antigens for enhanced fidelity.* Proc Natl Acad Sci U S A, 2016. **113**: 5610-5615.
63. Wang, X., Z. Rahil, I.T. Li, F. Chowdhury, D.E. Leckband, Y.R. Chemla, and T. Ha, *Constructing modular and universal single molecule tension sensor using protein G to study mechano-sensitive receptors.* Sci Rep, 2016. **6**: 21584.
64. Watt, F.M. and W.T. Huck, *Role of the extracellular matrix in regulating stem cell fate.* Nat Rev Mol Cell Biol, 2013. **14**: 467-473.
65. Das, R.K., V. Gocheva, R. Hammink, O.F. Zouani, and A.E. Rowan, *Stress-stiffening-mediated stem-cell commitment switch in soft responsive hydrogels.* Nat Mater, 2016. **15**: 318-325.
66. Chowdhury, F., I.T.S. Li, B.J. Leslie, S. Doganay, R. Singh, X. Wang, J. Seong, S.H. Lee, S. Park, N. Wang, and T. Ha, *Single molecular force across single integrins dictates cell spreading.* Integr Biol (Camb), 2015. **7**: 1265-1271.
67. Lee, M.K., J. Park, X. Wang, M. Roein-Peikar, E. Ko, E. Qin, J. Lee, T. Ha, and H. Kong, *Rupture force of cell adhesion ligand tethers modulates biological activities of a cell-laden hydrogel.* Chem Commun (Camb), 2016. **52**: 4757-4760.

68. Stabley, D.R., C. Jurchenko, S.S. Marshall, and K.S. Salaita, *Visualizing mechanical tension across membrane receptors with a fluorescent sensor.* Nat Methods, 2011. **9**: 64-67.
69. Jurchenko, C., Y. Chang, Y. Narui, Y. Zhang, and K.S. Salaita, *Integrin-generated forces lead to streptavidin-biotin unbinding in cellular adhesions.* Biophys J, 2014. **106**: 1436-1446.
70. Liu, Y., R. Medda, Z. Liu, K. Galior, K. Yehl, J.P. Spatz, E.A. Cavalcanti-Adam, and K. Salaita, *Nanoparticle tension probes patterned at the nanoscale: impact of integrin clustering on force transmission.* Nano Lett, 2014. **14**: 5539-5546.
71. Chang, Y., Z. Liu, Y. Zhang, K. Galior, J. Yang, and K. Salaita, *A General Approach for Generating Fluorescent Probes to Visualize Piconewton Forces at the Cell Surface.* J Am Chem Soc, 2016. **138**: 2901-2904.
72. Liu, Y., K. Yehl, Y. Narui, and K. Salaita, *Tension sensing nanoparticles for mechano-imaging at the living/nonliving interface.* J Am Chem Soc, 2013. **135**: 5320-5323.
73. Morimatsu, M., A.H. Mekhdjian, A.C. Chang, S.J. Tan, and A.R. Dunn, *Visualizing the interior architecture of focal adhesions with high-resolution traction maps.* Nano Lett, 2015. **15**: 2220-2228.
74. Grashoff, C., B.D. Hoffman, M.D. Brenner, R. Zhou, M. Parsons, M.T. Yang, M.A. McLean, S.G. Sligar, C.S. Chen, T. Ha, and M.A. Schwartz, *Measuring mechanical tension across vinculin reveals regulation of focal adhesion dynamics.* Nature, 2010. **466**: 263-266.
75. Morimatsu, M., A.H. Mekhdjian, A.S. Adhikari, and A.R. Dunn, *Molecular tension sensors report forces generated by single integrin molecules in living cells.* Nano Lett, 2013. **13**: 3985-3989.
76. Blakely, B.L., C.E. Dumelin, B. Trappmann, L.M. McGregor, C.K. Choi, P.C. Anthony, V.K. Duesterberg, B.M. Baker, S.M. Block, D.R. Liu, and C.S. Chen, *A DNA-based molecular probe for optically reporting cellular traction forces.* Nat Methods, 2014. **11**: 1229-1232.
77. Zhang, Y., C. Ge, C. Zhu, and K. Salaita, *DNA-based digital tension probes reveal integrin forces during early cell adhesion.* Nat Commun, 2014. **5**: 5167.
78. Galior, K., Y. Liu, K. Yehl, S. Vivek, and K. Salaita, *Titin-Based Nanoparticle Tension Sensors Map High-Magnitude Integrin Forces within Focal Adhesions.* Nano Lett, 2016. **16**: 341-348.
79. Woodside, M.T., W.M. Behnke-Parks, K. Larizadeh, K. Travers, D. Herschlag, and S.M. Block, *Nanomechanical measurements of the sequence-dependent folding landscapes of single nucleic acid hairpins.* Proc Natl Acad Sci U S A, 2006. **103**: 6190-6195.
80. Rief, M., M. Gautel, F. Oesterhelt, J.M. Fernandez, and H.E. Gaub, *Reversible unfolding of individual titin immunoglobulin domains by AFM.* Science, 1997. **276**: 1109-1112.
81. Carrion-Vazquez, M., A.F. Oberhauser, S.B. Fowler, P.E. Marszalek, S.E. Broedel, J. Clarke, and J.M. Fernandez, *Mechanical and chemical unfolding of a single protein: a comparison.* Proc Natl Acad Sci U S A, 1999. **96**: 3694-3699.

82. Smith, S.B., Y. Cui, and C. Bustamante, *Overstretching B-DNA: the elastic response of individual double-stranded and single-stranded DNA molecules.* Science, 1996. **271**: 795-799.
83. Cluzel, P., A. Lebrun, C. Heller, R. Lavery, J.L. Viovy, D. Chatenay, and F. Caron, *DNA: an extensible molecule.* Science, 1996. **271**: 792-794.
84. Aschenbrenner, D., D.A. Pippig, K. Klamecka, K. Limmer, H. Leonhardt, and H.E. Gaub, *Parallel force assay for protein-protein interactions.* Plos One, 2014. **9**: e115049.
85. Zohar, H., C.L. Hetherington, C. Bustamante, and S.J. Muller, *Peptide nucleic acids as tools for single-molecule sequence detection and manipulation.* Nano Lett, 2010. **10**: 4697-4701.
86. Dutta, S., B.A. Armitage, and Y.L. Lyubchenko, *Probing of miniPEGgamma-PNA-DNA Hybrid Duplex Stability with AFM Force Spectroscopy.* Biochemistry, 2016. **55**: 1523-1528.
87. Hatch, K., C. Danilowicz, V. Coljee, and M. Prentiss, *Demonstration that the shear force required to separate short double-stranded DNA does not increase significantly with sequence length for sequences longer than 25 base pairs.* Phys Rev E Stat Nonlin Soft Matter Phys, 2008. **78**: 011920.
88. Mosayebi, M., A.A. Louis, J.P. Doye, and T.E. Ouldridge, *Force-Induced Rupture of a DNA Duplex: From Fundamentals to Force Sensors.* ACS Nano, 2015. **9**: 11993-12003.
89. Bell, G.I., *Models for the specific adhesion of cells to cells.* Science, 1978. **200**: 618-627.
90. Evans, E. and K. Ritchie, *Dynamic strength of molecular adhesion bonds.* Biophys J, 1997. **72**: 1541-1555.
91. Evans, E., *Probing the relation between force--lifetime--and chemistry in single molecular bonds.* Annu Rev Biophys Biomol Struct, 2001. **30**: 105-128.
92. Bockelmann, U., B. EssevazRoulet, and F. Heslot, *Molecular stick-slip motion revealed by opening DNA with piconewton forces.* Phys Rev Lett, 1997. **79**: 4489-4492.
93. Xu, F., H. Zheng, N. Clauvelin, X.J. Lu, W.K. Olson, and V. Nanda, *Parallels between DNA and collagen - comparing elastic models of the double and triple helix.* Sci Rep, 2017. **7**: 12802.
94. Lu, X.J. and W.K. Olson, *3DNA: a software package for the analysis, rebuilding and visualization of three-dimensional nucleic acid structures.* Nucleic Acids Res, 2003. **31**: 5108-5121.
95. Ruoslahti, E., *RGD and other recognition sequences for integrins.* Annu Rev Cell Dev Biol, 1996. **12**: 697-715.
96. Moutevelis, E. and D.N. Woolfson, *A periodic table of coiled-coil protein structures.* J Mol Biol, 2009. **385**: 726-732.
97. Fuchs, E. and K. Weber, *Intermediate filaments: structure, dynamics, function, and disease.* Annu Rev Biochem, 1994. **63**: 345-382.
98. Cooper, G.M., *The Cell: A Molecular Approach.* 2nd edition ed. Intermediate Filaments. 2000, Sunderland (MA): Sinauer Associates.

99. Kolomeisky, A.B., *Motor proteins and molecular motors: how to operate machines at the nanoscale.* J Phys Condens Matter, 2013. **25**: 463101.

100. Sweeney, H.L. and A. Houdusse, *Structural and functional insights into the Myosin motor mechanism.* Annu Rev Biophys, 2010. **39**: 539-557.

101. Rice, S., A.W. Lin, D. Safer, C.L. Hart, N. Naber, B.O. Carragher, S.M. Cain, E. Pechatnikova, E.M. Wilson-Kubalek, M. Whittaker, E. Pate, R. Cooke, E.W. Taylor, R.A. Milligan, and R.D. Vale, *A structural change in the kinesin motor protein that drives motility.* Nature, 1999. **402**: 778-784.

102. Burgess, S.A., M.L. Walker, H. Sakakibara, P.J. Knight, and K. Oiwa, *Dynein structure and power stroke.* Nature, 2003. **421**: 715-718.

103. Burkhard, P., J. Stetefeld, and S.V. Strelkov, *Coiled coils: a highly versatile protein folding motif.* Trends Cell Biol, 2001. **11**: 82-88.

104. Woolner, S. and W.M. Bement, *Unconventional myosins acting unconventionally.* Trends Cell Biol, 2009. **19**: 245-252.

105. Paulsson, M., D. Piecha, D. Segat, N. Smyth, and R. Wagener, *The matrilins: a growing family of A-domain-containing proteins.* Biochem Soc Trans, 1999. **27**: 824-826.

106. Kammerer, R.A., T. Schulthess, R. Landwehr, A. Lustig, D. Fischer, and J. Engel, *Tenascin-C hexabrachion assembly is a sequential two-step process initiated by coiled-coil alpha-helices.* J Biol Chem, 1998. **273**: 10602-10608.

107. Engel, J., *Laminins and other strange proteins.* Biochemistry, 1992. **31**: 10643-10651.

108. Adams, J.C., *Thrombospondins: multifunctional regulators of cell interactions.* Annu Rev Cell Dev Biol, 2001. **17**: 25-51.

109. Guo, Y., R.A. Kammerer, and J. Engel, *The unusually stable coiled-coil domain of COMP exhibits cold and heat denaturation in 4-6 M guanidinium chloride.* Biophys Chem, 2000. **85**: 179-186.

110. Malashkevich, V.N., R.A. Kammerer, V.P. Efimov, T. Schulthess, and J. Engel, *The crystal structure of a five-stranded coiled coil in COMP: a prototype ion channel?* Science, 1996. **274**: 761-765.

111. Klatt, A.R., A.K. Becker, C.D. Neacsu, M. Paulsson, and R. Wagener, *The matrilins: modulators of extracellular matrix assembly.* Int J Biochem Cell Biol, 2011. **43**: 320-330.

112. Engel, J., *Role of oligomerization domains in thrombospondins and other extracellular matrix proteins.* Int J Biochem Cell Biol, 2004. **36**: 997-1004.

113. Hamill, K.J., K. Kligys, S.B. Hopkinson, and J.C. Jones, *Laminin deposition in the extracellular matrix: a complex picture emerges.* J Cell Sci, 2009. **122**: 4409-4417.

114. Liu, J. and B. Rost, *Comparing function and structure between entire proteomes.* Protein Sci, 2001. **10**: 1970-1979.

115. Thomas, F., A.L. Boyle, A.J. Burton, and D.N. Woolfson, *A set of de novo designed parallel heterodimeric coiled coils with quantified dissociation constants in the micromolar to sub-nanomolar regime.* J Am Chem Soc, 2013. **135**: 5161-5166.

116. Steinmetz, M.O., I. Jelesarov, W.M. Matousek, S. Honnappa, W. Jahnke, J.H. Missimer, S. Frank, A.T. Alexandrescu, and R.A. Kammerer, *Molecular basis of coiled-coil formation.* Proc Natl Acad Sci U S A, 2007. **104**: 7062-7067.

117. Woolfson, D.N., *The design of coiled-coil structures and assemblies.* Adv Protein Chem, 2005. **70**: 79-112.

118. Goktas, M., C. Luo, R.M.A. Sullan, A.E. Bergues-Pupo, R. Lipowsky, A. Vila Verde, and K.G. Blank, *Molecular mechanics of coiled coils loaded in the shear geometry.* Chem Sci, 2018. **9**: 4610-4621.

119. Woolfson, D.N. and T. Alber, *Predicting Oligomerization States of Coiled Coils.* Protein Sci, 1995. **4**: 1596-1607.

120. Parry, D.A.D., *Coiled-Coils in Alpha-Helix-Containing Proteins - Analysis of the Residue Types within the Heptad Repeat and the Use of These Data in the Prediction of Coiled-Coils in Other Proteins.* Biosci Rep, 1982. **2**: 1017-1024.

121. O'Shea, E.K., J.D. Klemm, P.S. Kim, and T. Alber, *X-ray structure of the GCN4 leucine zipper, a two-stranded, parallel coiled coil.* Science, 1991. **254**: 539-544.

122. Gonzalez, L., D.N. Woolfson, and T. Alber, *Buried polar residues and structural specificity in the GCN4 leucine zipper.* Nat Struct Biol, 1996. **3**: 1011-1018.

123. Harbury, P.B., T. Zhang, P.S. Kim, and T. Alber, *A switch between two-, three-, and four-stranded coiled coils in GCN4 leucine zipper mutants.* Science, 1993. **262**: 1401-1407.

124. Sodek, J., R.S. Hodges, L.B. Smillie, and L. Jurasek, *Amino-acid sequence of rabbit skeletal tropomyosin and its coiled-coil structure.* Proc Natl Acad Sci U S A, 1972. **69**: 3800-3804.

125. O'Shea, E.K., R. Rutkowski, W.F. Stafford, 3rd, and P.S. Kim, *Preferential heterodimer formation by isolated leucine zippers from fos and jun.* Science, 1989. **245**: 646-648.

126. O'Shea, E.K., R. Rutkowski, and P.S. Kim, *Mechanism of specificity in the Fos-Jun oncoprotein heterodimer.* Cell, 1992. **68**: 699-708.

127. Dahiyat, B.I., D.B. Gordon, and S.L. Mayo, *Automated design of the surface positions of protein helices.* Protein Sci, 1997. **6**: 1333-1337.

128. Kaplan, J.B., A.W. Reinke, and A.E. Keating, *Increasing the affinity of selective bZIP-binding peptides through surface residue redesign.* Protein Sci, 2014. **23**: 940-953.

129. Drobnak, I., H. Gradisar, A. Ljubetic, E. Merljak, and R. Jerala, *Modulation of Coiled-Coil Dimer Stability through Surface Residues while Preserving Pairing Specificity.* J Am Chem Soc, 2017. **139**: 8229-8236.

130. Lupas, A.N. and M. Gruber, *The structure of alpha-helical coiled coils.* Adv Protein Chem, 2005. **70**: 37-78.

131. Herrmann, H., H. Bar, L. Kreplak, S.V. Strelkov, and U. Aebi, *Intermediate filaments: from cell architecture to nanomechanics.* Nat Rev Mol Cell Biol, 2007. **8**: 562-573.

132. Apostolovic, B., M. Danial, and H.A. Klok, *Coiled coils: attractive protein folding motifs for the fabrication of self-assembled, responsive and bioactive materials.* Chem Soc Rev, 2010. **39**: 3541-3575.

133. Schwaiger, I., C. Sattler, D.R. Hostetter, and M. Rief, *The myosin coiled-coil is a truly elastic protein structure.* Nat Mater, 2002. **1**: 232-235.

134. Root, D.D., V.K. Yadavalli, J.G. Forbes, and K. Wang, *Coiled-coil nanomechanics and uncoiling and unfolding of the superhelix and alpha-helices of myosin.* Biophys J, 2006. **90**: 2852-2866.

135. Taniguchi, Y., B.S. Khatri, D.J. Brockwell, E. Paci, and M. Kawakami, *Dynamics of the coiled-coil unfolding transition of myosin rod probed by dissipation force spectrum.* Biophys J, 2010. **99**: 257-262.

136. Ackbarow, T. and M.J. Buehler, *Superelasticity, energy dissipation and strain hardening of vimentin coiled-coil intermediate filaments: atomistic and continuum studies.* J Mater Sci, 2007. **42**: 8771-8787.

137. Qin, Z., L. Kreplak, and M.J. Buehler, *Hierarchical Structure Controls Nanomechanical Properties of Vimentin Intermediate Filaments.* Plos One, 2009. **4**: e7294.

138. Ramm, B., J. Stigler, M. Hinczewski, D. Thirumalai, H. Herrmann, G. Woehlke, and M. Rief, *Sequence-resolved free energy profiles of stress-bearing vimentin intermediate filaments.* Proc Natl Acad Sci U S A, 2014. **111**: 11359-11364.

139. Block, J., H. Witt, A. Candelli, E.J. Peterman, G.J. Wuite, A. Janshoff, and S. Koster, *Nonlinear Loading-Rate-Dependent Force Response of Individual Vimentin Intermediate Filaments to Applied Strain.* Phys Rev Lett, 2017. **118**: 048101.

140. Brown, A.E.X., R.I. Litvinov, D.E. Discher, and J.W. Weisel, *Forced unfolding of coiled-coils in fibrinogen by single-molecule AFM.* Biophys J, 2007. **92**: L39-L41.

141. Lim, B.B.C., E.H. Lee, M. Sotomayor, and K. Schulten, *Molecular basis of fibrin clot elasticity.* Structure, 2008. **16**: 449-459.

142. Zhmurov, A., O. Kononova, R.I. Litvinov, R.I. Dima, V. Barsegov, and J.W. Weisel, *Mechanical transition from alpha-helical coiled coils to beta-sheets in fibrin(ogen).* J Am Chem Soc, 2012. **134**: 20396-20402.

143. Miserez, A. and P.A. Guerette, *Phase transition-induced elasticity of alpha-helical bioelastomeric fibres and networks.* Chem Soc Rev, 2013. **42**: 1973-1995.

144. Minin, K.A., A. Zhmurov, K.A. Marx, P.K. Purohit, and V. Barsegov, *Dynamic Transition from alpha-Helices to beta-Sheets in Polypeptide Coiled-Coil Motifs.* J Am Chem Soc, 2017. **139**: 16168-16177.

145. Qin, Z. and M.J. Buehler, *Molecular dynamics simulation of the alpha-helix to beta-sheet transition in coiled protein filaments: evidence for a critical filament length scale.* Phys Rev Lett, 2010. **104**: 198304.

146. Rief, M., H. Clausen-Schaumann, and H.E. Gaub, *Sequence-dependent mechanics of single DNA molecules.* Nat Struct Biol, 1999. **6**: 346-349.

147. Bornschlogl, T. and M. Rief, *Single molecule unzipping of coiled coils: sequence resolved stability profiles.* Phys Rev Lett, 2006. **96**: 118102.

148. Xi, Z., Y. Gao, G. Sirinakis, H. Guo, and Y. Zhang, *Single-molecule observation of helix staggering, sliding, and coiled coil misfolding.* Proc Natl Acad Sci U S A, 2012. **109**: 5711-5716.

149. Bornschlogl, T., G. Woehlke, and M. Rief, *Single molecule mechanics of the kinesin neck.* Proc Natl Acad Sci U S A, 2009. **106**: 6992-6997.

150. Hanwell, M.D., D.E. Curtis, D.C. Lonie, T. Vandermeersch, E. Zurek, and G.R. Hutchison, *Avogadro: an advanced semantic chemical editor, visualization, and analysis platform.* J Cheminform, 2012. **4**: 17.

151. Zimmermann, J.L., T. Nicolaus, G. Neuert, and K. Blank, *Thiol-based, site-specific and covalent immobilization of biomolecules for single-molecule experiments.* Nat Protoc, 2010. **5**: 975-985.

152. Su, J.Y., R.S. Hodges, and C.M. Kay, *Effect of chain length on the formation and stability of synthetic alpha-helical coiled coils.* Biochemistry, 1994. **33**: 15501-15510.

153. Block, J., H. Witt, A. Candelli, E.J.G. Peterman, G.J.L. Wuite, A. Janshoff, and S. Koster, *Nonlinear Loading-Rate-Dependent Force Response of Individual Vimentin Intermediate Filaments to Applied Strain.* Phys Rev Lett, 2017. **118**: 048101.

154. Taniguchi, Y., B.S. Khatri, D.J. Brockwell, E. Paci, and M. Kawakami, *Dynamics of the Coiled-Coil Unfolding Transition of Myosin Rod Probed by Dissipation Force Spectrum.* Biophys J, 2010. **99**: 257-262.

155. Miserez, A. and P.A. Guerette, *Phase transition-induced elasticity of alpha-helical bioelastomeric fibres and networks.* Chem Soc Rev, 2013. **42**: 1973-1995.

156. Minin, K.A., A. Zhmurov, K.A. Marx, P.K. Purohit, and V. Barsegov, *Dynamic Transition from alpha-Helices to beta-Sheets in Polypeptide Coiled-Coil Motifs.* J Am Chem Soc, 2017. **139**: 16168-16177.

157. Falkovich, S.G., I.M. Neelov, and A.A. Darinskii, *Mechanism of Shear Deformation of a Coiled Myosin Coil: Computer Simulation.* Polym Sci Ser a+, 2010. **52**: 662-670.

158. Hamed, E. and S. Keten, *Hierarchical Cascades of Instability Govern the Mechanics of Coiled Coils: Helix Unfolding Precedes Coil Unzipping.* Biophys J, 2014. **107**: 477-484.

159. Kreuzer, S.M., T.J. Moon, and R. Elber, *Catch bond-like kinetics of helix cracking: network analysis by molecular dynamics and milestoning.* J Chem Phys, 2013. **139**: 121902.

160. Sorin, E.J. and V.S. Pande, *Exploring the helix-coil transition via all-atom equilibrium ensemble simulations.* Biophys J, 2005. **88**: 2472-2493.

161. Fierz, B., A. Reiner, and T. Kiefhaber, *Local conformational dynamics in alpha-helices measured by fast triplet transfer.* Proc Natl Acad Sci U S A, 2009. **106**: 1057-1062.

162. Jeon, S.I., J.H. Lee, J.D. Andrade, and P.G. De Gennes, *Protein—surface interactions in the presence of polyethylene oxide: I. Simplified theory.* J Colloid Interface Sci, 1991. **142**: 149-158.

163. Alcantar, N.A., E.S. Aydil, and J.N. Israelachvili, *Polyethylene glycol-coated biocompatible surfaces.* J Biomed Mater Res, 2000. **51**: 343-351.

164. Plow, E.F., T.K. Haas, L. Zhang, J. Loftus, and J.W. Smith, *Ligand binding to integrins.* J Biol Chem, 2000. **275**: 21785-21788.

165. Maruthamuthu, V., B. Sabass, U.S. Schwarz, and M.L. Gardel, *Cell-ECM traction force modulates endogenous tension at cell-cell contacts.* Proc Natl Acad Sci U S A, 2011. **108**: 4708-4713.

166. Cosgrove, B.D., K.L. Mui, T.P. Driscoll, S.R. Caliari, K.D. Mehta, R.K. Assoian, J.A. Burdick, and R.L. Mauck, *N-cadherin adhesive interactions modulate matrix mechanosensing and fate commitment of mesenchymal stem cells.* Nat Mater, 2016. **15**: 1297-1306.

167. Kon, T., K. Imamula, A.J. Roberts, R. Ohkura, P.J. Knight, I.R. Gibbons, S.A. Burgess, and K. Sutoh, *Helix sliding in the stalk coiled coil of dynein couples ATPase and microtubule binding.* Nat Struct Mol Biol, 2009. **16**: 325-333.
168. Carter, A.P., C. Cho, L. Jin, and R.D. Vale, *Crystal structure of the dynein motor domain.* Science, 2011. **331**: 1159-1165.
169. Gibbons, I.R., J.E. Garbarino, C.E. Tan, S.L. Reck-Peterson, R.D. Vale, and A.P. Carter, *The affinity of the dynein microtubule-binding domain is modulated by the conformation of its coiled-coil stalk.* J Biol Chem, 2005. **280**: 23960-23965.
170. Yogurtcu, O.N., C.W. Wolgemuth, and S.X. Sun, *Mechanical response and conformational amplification in alpha-helical coiled coils.* Biophys J, 2010. **99**: 3895-3904.
171. Morfill, J., F. Kuhner, K. Blank, R.A. Lugmaier, J. Sedlmair, and H.E. Gaub, *B-S transition in short oligonucleotides.* Biophys J, 2007. **93**: 2400-2409.
172. Strunz, T., K. Oroszlan, R. Schafer, and H.J. Guntherodt, *Dynamic force spectroscopy of single DNA molecules.* Proc Natl Acad Sci U S A, 1999. **96**: 11277-11282.
173. Gross, P., N. Laurens, L.B. Oddershede, U. Bockelmann, E.J.G. Peterman, and G.J.L. Wuite, *Quantifying how DNA stretches, melts and changes twist under tension.* Nat Phys, 2011. **7**: 731-736.
174. Dietz, H., T. Bornschlogl, R. Heym, F. Konig, and M. Rief, *Programming protein self assembly with coiled coils.* New J Phys, 2007. **9**: 1-8.
175. Gao, Y., G. Sirinakis, and Y. Zhang, *Highly anisotropic stability and folding kinetics of a single coiled coil protein under mechanical tension.* J Am Chem Soc, 2011. **133**: 12749-12757.
176. Berkemeier, F., M. Bertz, S. Xiao, N. Pinotsis, M. Wilmanns, F. Grater, and M. Rief, *Fast-folding alpha-helices as reversible strain absorbers in the muscle protein myomesin.* Proc Natl Acad Sci U S A, 2011. **108**: 14139-14144.
177. Paik, D.H. and T.T. Perkins, *Overstretching DNA at 65 pN does not require peeling from free ends or nicks.* J Am Chem Soc, 2011. **133**: 3219-3221.
178. Fu, H., H. Chen, X. Zhang, Y. Qu, J.F. Marko, and J. Yan, *Transition dynamics and selection of the distinct S-DNA and strand unpeeling modes of double helix overstretching.* Nucleic Acids Res, 2011. **39**: 3473-3481.
179. King, G.A., P. Gross, U. Bockelmann, M. Modesti, G.J. Wuite, and E.J. Peterman, *Revealing the competition between peeled ssDNA, melting bubbles, and S-DNA during DNA overstretching using fluorescence microscopy.* Proc Natl Acad Sci U S A, 2013. **110**: 3859-3864.
180. Zhang, X., H. Chen, S. Le, I. Rouzina, P.S. Doyle, and J. Yan, *Revealing the competition between peeled ssDNA, melting bubbles, and S-DNA during DNA overstretching by single-molecule calorimetry.* Proc Natl Acad Sci U S A, 2013. **110**: 3865-3870.
181. Roca-Cusachs, P., T. Iskratsch, and M.P. Sheetz, *Finding the weakest link: exploring integrin-mediated mechanical molecular pathways.* J Cell Sci, 2012. **125**: 3025-3038.
182. Thoumine, O., P. Kocian, A. Kottelat, and J.J. Meister, *Short-term binding of fibroblasts to fibronectin: optical tweezers experiments and probabilistic analysis.* Eur Biophys J, 2000. **29**: 398-408.

183. Sun, Z., L.A. Martinez-Lemus, A. Trache, J.P. Trzeciakowski, G.E. Davis, U. Pohl, and G.A. Meininger, *Mechanical properties of the interaction between fibronectin and alpha5beta1-integrin on vascular smooth muscle cells studied using atomic force microscopy.* Am J Physiol Heart Circ Physiol, 2005. **289**: H2526-2535.

184. Burton, K., J.H. Park, and D.L. Taylor, *Keratocytes generate traction forces in two phases.* Mol Biol Cell, 1999. **10**: 3745-3769.

185. du Roure, O., A. Saez, A. Buguin, R.H. Austin, P. Chavrier, P. Silberzan, and B. Ladoux, *Force mapping in epithelial cell migration.* Proc Natl Acad Sci U S A, 2005. **102**: 2390-2395.

186. Arnold, M., E.A. Cavalcanti-Adam, R. Glass, J. Blummel, W. Eck, M. Kantlehner, H. Kessler, and J.P. Spatz, *Activation of integrin function by nanopatterned adhesive interfaces.* Chemphyschem, 2004. **5**: 383-388.

187. Cavalcanti-Adam, E.A., T. Volberg, A. Micoulet, H. Kessler, B. Geiger, and J.P. Spatz, *Cell spreading and focal adhesion dynamics are regulated by spacing of integrin ligands.* Biophys J, 2007. **92**: 2964-2974.

188. Koo, L.Y., D.J. Irvine, A.M. Mayes, D.A. Lauffenburger, and L.G. Griffith, *Co-regulation of cell adhesion by nanoscale RGD organization and mechanical stimulus.* J Cell Sci, 2002. **115**: 1423-1433.

189. Marshall, B.T., M. Long, J.W. Piper, T. Yago, R.P. McEver, and C. Zhu, *Direct observation of catch bonds involving cell-adhesion molecules.* Nature, 2003. **423**: 190-193.

190. Guo, B. and W.H. Guilford, *Mechanics of actomyosin bonds in different nucleotide states are tuned to muscle contraction.* Proc Natl Acad Sci U S A, 2006. **103**: 9844-9849.

191. Yago, T., J. Lou, T. Wu, J. Yang, J.J. Miner, L. Coburn, J.A. Lopez, M.A. Cruz, J.F. Dong, L.V. McIntire, R.P. McEver, and C. Zhu, *Platelet glycoprotein Ibalpha forms catch bonds with human WT vWF but not with type 2B von Willebrand disease vWF.* J Clin Invest, 2008. **118**: 3195-3207.

192. Pierschbacher, M.D. and E. Ruoslahti, *Cell attachment activity of fibronectin can be duplicated by small synthetic fragments of the molecule.* Nature, 1984. **309**: 30-33.

193. Danen, E.H., S. Aota, A.A. van Kraats, K.M. Yamada, D.J. Ruiter, and G.N. van Muijen, *Requirement for the synergy site for cell adhesion to fibronectin depends on the activation state of integrin alpha 5 beta 1.* J Biol Chem, 1995. **270**: 21612-21618.

194. Redick, S.D., D.L. Settles, G. Briscoe, and H.P. Erickson, *Defining fibronectin's cell adhesion synergy site by site-directed mutagenesis.* J Cell Biol, 2000. **149**: 521-527.

195. Aota, S., M. Nomizu, and K.M. Yamada, *The short amino acid sequence Pro-His-Ser-Arg-Asn in human fibronectin enhances cell-adhesive function.* J Biol Chem, 1994. **269**: 24756-24761.

196. Nagae, M., S. Re, E. Mihara, T. Nogi, Y. Sugita, and J. Takagi, *Crystal structure of alpha5beta1 integrin ectodomain: atomic details of the fibronectin receptor.* J Cell Biol, 2012. **197**: 131-140.

197. Baneres, J.L., F. Roquet, A. Martin, and J. Parello, *A minimized human integrin alpha(5)beta(1) that retains ligand recognition.* J Biol Chem, 2000. **275**: 5888-5903.

198. Mould, A.P., S.K. Akiyama, and M.J. Humphries, *Regulation of integrin alpha 5 beta 1-fibronectin interactions by divalent cations. Evidence for distinct classes of binding sites for Mn2+, Mg2+, and Ca2+.* J Biol Chem, 1995. **270**: 26270-26277.
199. Takagi, J., B.M. Petre, T. Walz, and T.A. Springer, *Global conformational rearrangements in integrin extracellular domains in outside-in and inside-out signaling.* Cell, 2002. **110**: 599-511.
200. Danmark, S., C. Aronsson, and D. Aili, *Tailoring Supramolecular Peptide-Poly(ethylene glycol) Hydrogels by Coiled Coil Self-Assembly and Self-Sorting.* Biomacromolecules, 2016. **17**: 2260-2267.
201. Oesterhelt, F., *Single molecule force spectroscopy by AFM indicates helical structure of poly(ethylene-glycol) in water.* New J Phys, 1999. **1**: 6.1-6.11.
202. Berendsen, H.J.C., D. Vanderspoel, and R. Vandrunen, *Gromacs - a Message-Passing Parallel Molecular-Dynamics Implementation.* Comput Phys Commun, 1995. **91**: 43-56.
203. Van der Spoel, D., E. Lindahl, B. Hess, G. Groenhof, A.E. Mark, and H.J.C. Berendsen, *GROMACS: Fast, flexible, and free.* J Comput Chem, 2005. **26**: 1701-1718.
204. Hess, B., C. Kutzner, D. van der Spoel, and E. Lindahl, *GROMACS 4: Algorithms for highly efficient, load-balanced, and scalable molecular simulation.* J Chem Theory Comput, 2008. **4**: 435-447.
205. Pronk, S., S. Pall, R. Schulz, P. Larsson, P. Bjelkmar, R. Apostolov, M.R. Shirts, J.C. Smith, P.M. Kasson, D. van der Spoel, B. Hess, and E. Lindahl, *GROMACS 4.5: a high-throughput and highly parallel open source molecular simulation toolkit.* Bioinformatics, 2013. **29**: 845-854.
206. Qiu, D., P.S. Shenkin, F.P. Hollinger, and W.C. Still, *The GB/SA continuum model for solvation. A fast analytical method for the calculation of approximate Born radii.* J Phys Chem A, 1997. **101**: 3005-3014.
207. Hornak, V., R. Abel, A. Okur, B. Strockbine, A. Roitberg, and C. Simmerling, *Comparison of multiple Amber force fields and development of improved protein backbone parameters.* Proteins, 2006. **65**: 712-725.
208. Bromley, E.H., K.J. Channon, P.J. King, Z.N. Mahmoud, E.F. Banwell, M.F. Butler, M.P. Crump, T.R. Dafforn, M.R. Hicks, J.D. Hirst, A. Rodger, and D.N. Woolfson, *Assembly pathway of a designed alpha-helical protein fiber.* Biophys J, 2010. **98**: 1668-1676.

Appendix

A1 Experimental details for the steered molecular dynamics simulations

All simulations were performed using the GROMACS-4.6.7 software package [202-205] and the Amber99-SB force field with the GBSA implicit water model [206, 207]. The standard leap-frog integrator for stochastic dynamics with a time step of 2 fs was used. Non-periodic simulation boxes without pressure coupling were used for all simulations in implicit solvent. The Coulomb interaction cut-off was 5 nm, which is sufficiently long for non-periodic simulations. All covalent bonds to hydrogen were constrained to remove fast vibrations. The simulation box size was $17 \times 7 \times 7$ nm^3 and a NVT ensemble was used during pulling. The fast smooth Particle-Mesh Ewald (PME) method was used to calculate long-range Coulomb interactions and the cut-off for short-range interactions was 1.0 nm. The points of force application were located on the α-C-atoms of the terminal glycines, using virtual harmonic springs with an elastic constant of $k = 1000$ kJ mol^{-1} nm^{-2} = 1650 pN nm^{-1}. The distal end of the virtual spring at the N-terminus of peptide A was fixed, while the distal end of the virtual spring coupled to the C-terminus of the B-peptides was moved at a constant speed, parallel to the axis of the coiled coil. All simulations were carried out at room temperature ($T = 300$ K) and the retract speeds varied from v = 10^6 nm s^{-1} to v = 10^9 nm s^{-1}. During each constant velocity simulation, the extension $\Delta L = v \times t$, where v is the retract speed and t is time, and the corresponding force F felt by the pulled virtual spring were calculated.

For the coiled coil sequences used no crystal structures are available. Therefore, the initial structures of all coiled coils were generated in the following way: (1) two separate α-helices were generated using the given sequences using Avogadro [150] and geometry optimized. (2) The individual α-helices were moved together slowly at T = 10 K with paired distance restraints between the heptads of each helix. (3) All restraints were removed and the structure was relaxed at T = 300 K for 300 ns. The resulting structures were stable at 300 K and showed a typical coiled coil structure, characterized by a left-handed superhelix with paired salt-bridges and a well-defined hydrophobic core. For the two slowest retract speeds, 5 (CC-A_4B_3) and 6 (CC-A_4B_4) independent simulations were performed in implicit solvent. 20 independent simulations were carried out for both coiled coils at $v = 10^8$ nm s^{-1}. At $v = 10^9$ nm s^{-1}, 40 simulations were performed for CC-A_4B_4 and 20 for CC-A_4B_3. Only 20 independent runs were performed for CC-A_4B_3 at $v = 10^9$ nm s^{-1}, because the comparison of the results from 20 and 40 simulations for CC-A_4B_4 at the same retract speed indicated that the lower number of simulations was sufficient to obtain meaningful results. Each independent run used the same simulation parameters, but started from different initial structures, obtained at different time points of the equilibration simulation (between 200 and 300 ns).

A2 CD analysis of RGDS-functionalized coiled coils and CC-A_6B_6

To show that RGDS conjugation does not affect the secondary structure and the thermal stability of the resulting CC-based MFS constructs, CD spectra and thermal denaturation curves were recorded for CC-A_4B_4, A_4B_4-MFS, CC-A_5B_5 and A_5B_5-MFS. For all CCs, the CD spectra show the characteristic minima at 208 nm and 222 nm, indicating α-helical secondary structure (**Figure S1**). The thermal denaturation experiments reveal that the conjugation of RGDS does not have any significant effect on the thermal stability of the final MFS constructs. A melting temperature (T_m) of 80.5ºC was recorded for CC-A_4B_4 and for A_4B_4-MFS the T_m was 80.3ºC (**Figure S2A**, **Table S1**). The longer CC-A_5B_5 and A_5B_5-MFS possess a very high thermodynamic stability and no unfolding transition was observed during the thermal denaturation experiment, indicating a T_m above 90.0ºC for both CCs (**Figure S2B**, **Table S1)**.

The secondary structure analysis for the CC-A_6B_6 indicated that even the individual A_6 and B_6 peptides were highly helical (as judged by the increased intensity of the 222 nm peak) (**Figure S3A**). When combined together to form the CC-A_6B_6 heterodimer, the spectra became distorted and are characterized by a decreased intensity at 208 nm and a red shifted 222 nm peak (**Figure S3B**). These changes in the CD spectra indicate the formation of elongated helical structures, as described in previous studies [208].

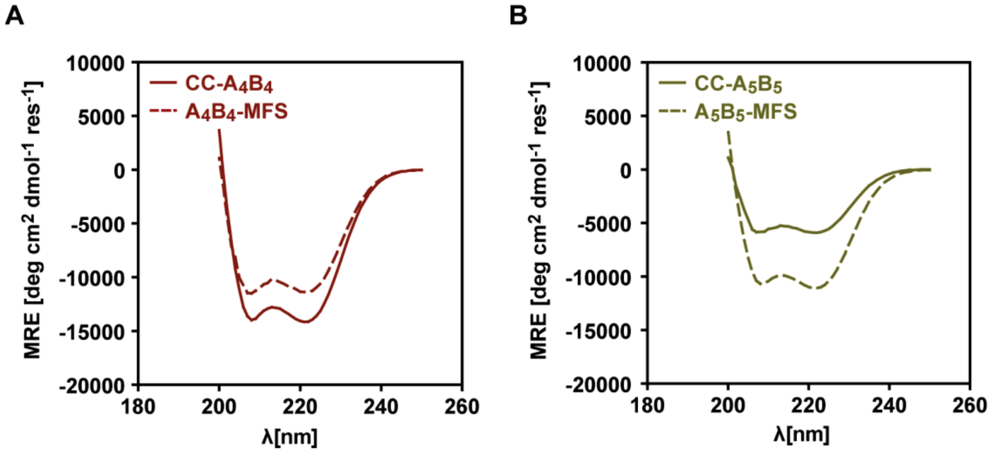

Figure S1. CD spectra of CC-A_4B_4 and CC-A_5B_5 and the corresponding CCs modified with cell-adhesive ligands (20°C). A) Comparison of the CD spectra of CC-A_4B_4 and A_4B_4-MFS. B) Comparison of the CD spectra of CC-A_5B_5 and A_5B_5-MFS. All measurements were performed in PBS, using a total peptide concentration of 100 μM.

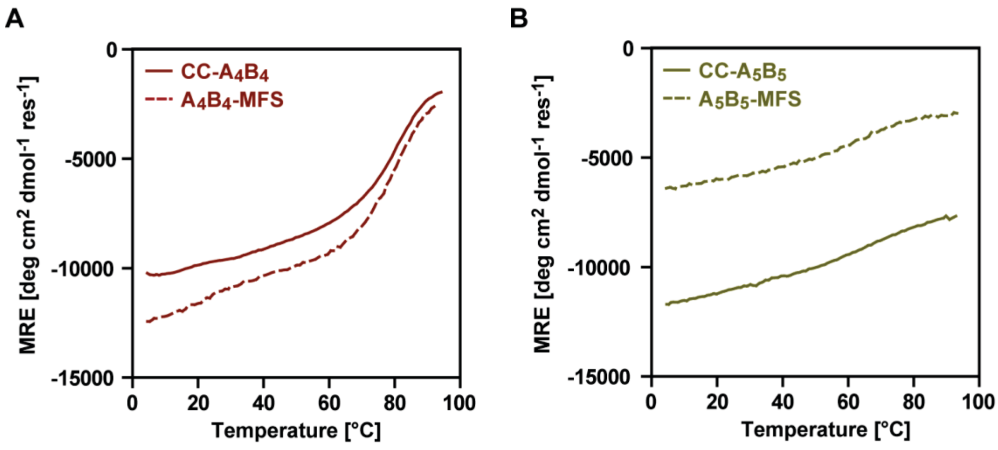

Figure S2. Thermal denaturation of CC-A_4B_4 and CC-A_5B_5 and the corresponding CCs modified with cell-adhesive ligands (222 nm). A) Thermal stability of CC-A_4B_4 and A_4B_4-MFS. B) Thermal stability of CC-A_5B_5 and A_5B_5-MFS. All measurements were performed in PBS, using a total peptide concentration of 100 μM.

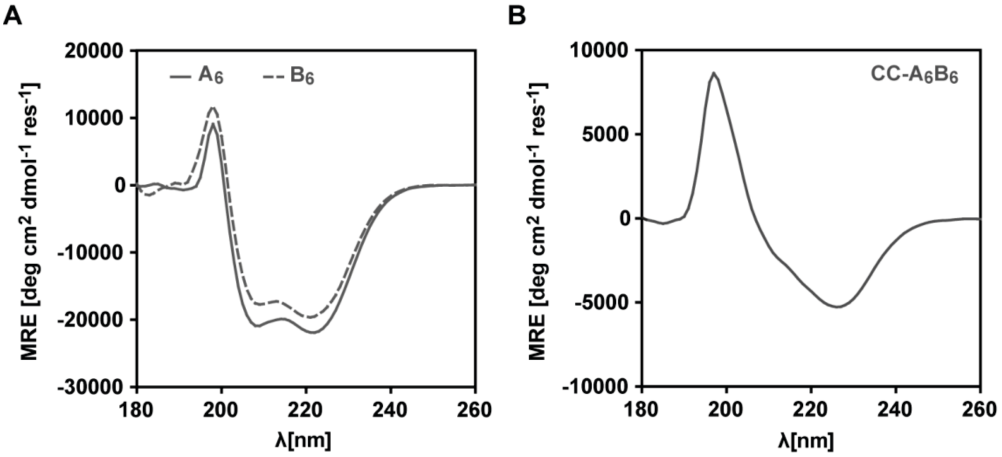

Figure S3. CD spectra of the individual A_6, B_6 peptides and CC-A_6B_6 (20°C). A) Comparison of the CD spectra of the individual A_6 and B_6 peptides. B) CD spectrum of CC-A_6B_6, suggesting a fiber-like structure. All measurements were performed in PBS, using a total peptide concentration of 100 μM.

Table S1. Summary of the melting temperatures for CC-A_4B_4 and CC-A_5B_5 and the corresponding RGDS conjugates. The data represents the mean ± SEM of 3 independent measurements.

Heterodimer	T_{m_CC} **[°C]**
CC-A_4B_4	80.5 ± 0.8
A_4B_4-MFS	80.3 ± 0.1
CC-A_5B_5	> 90.0
A_5B_5-MFS	> 90.0

A3 Length dependence of coiled coil rupture determined with dynamic single-molecule force spectroscopy (SMFS)

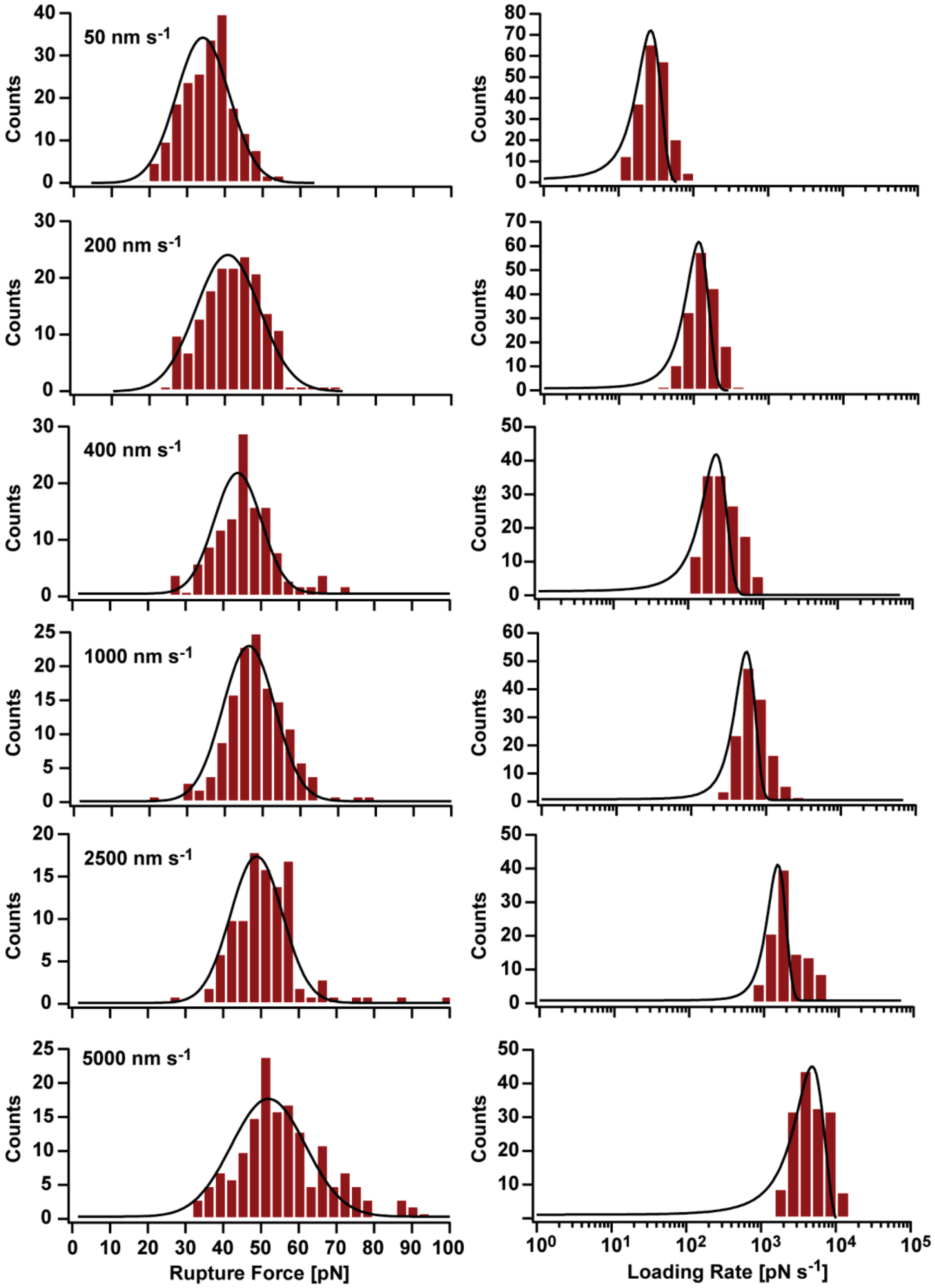

Figure S4. Data set (Cantilever 2) for CC-A_4B_4 measured at 6 different retract speeds. The black lines represent Gaussian fits to the data. The number of rupture events included in each histogram is listed in table S2.

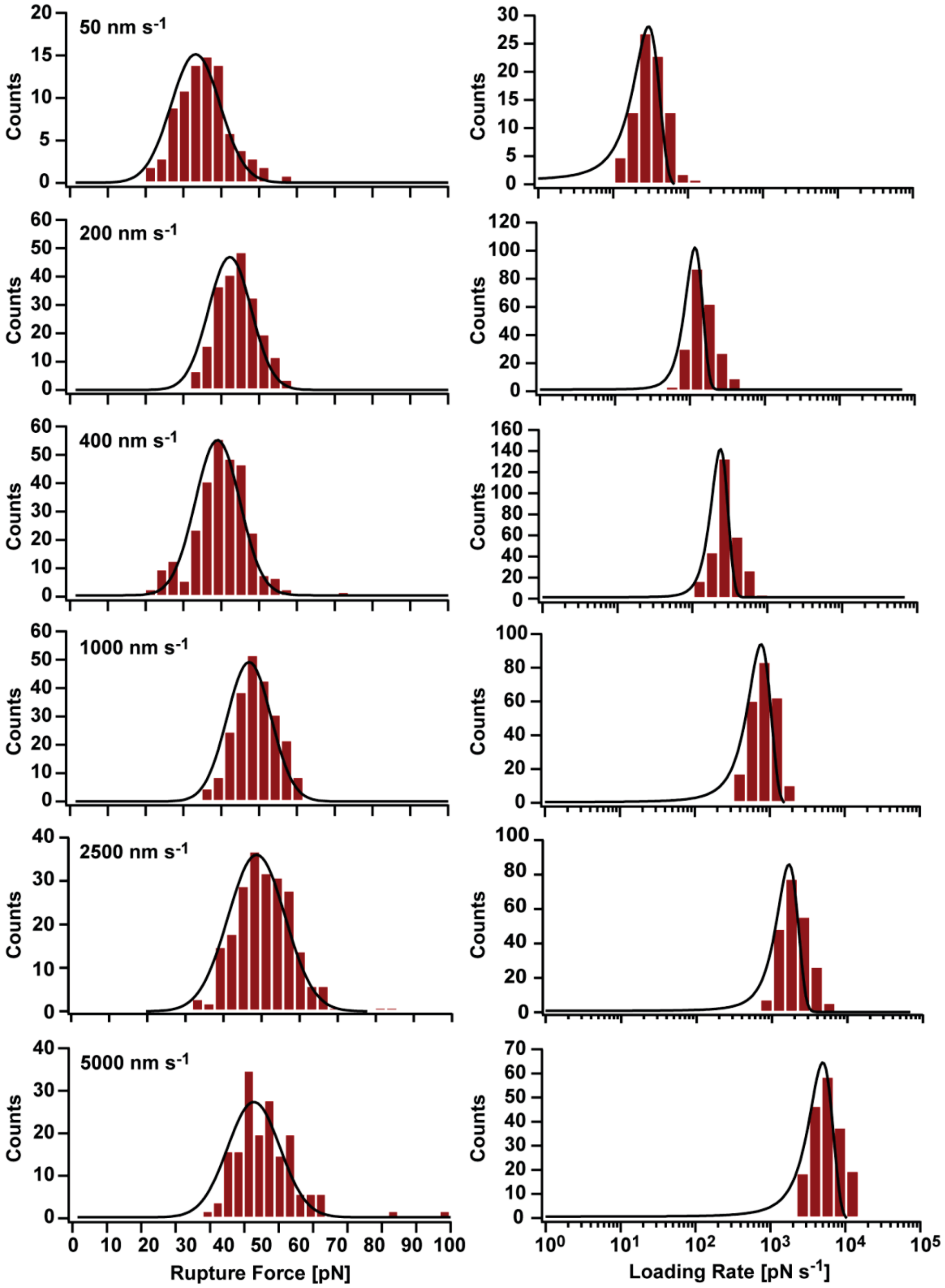

Figure S5. Data set (Cantilever 3) for CC-A_4B_4 measured at 6 different retract speeds. The black lines represent Gaussian fits to the data. The number of rupture events included in each histogram is listed in table S2.

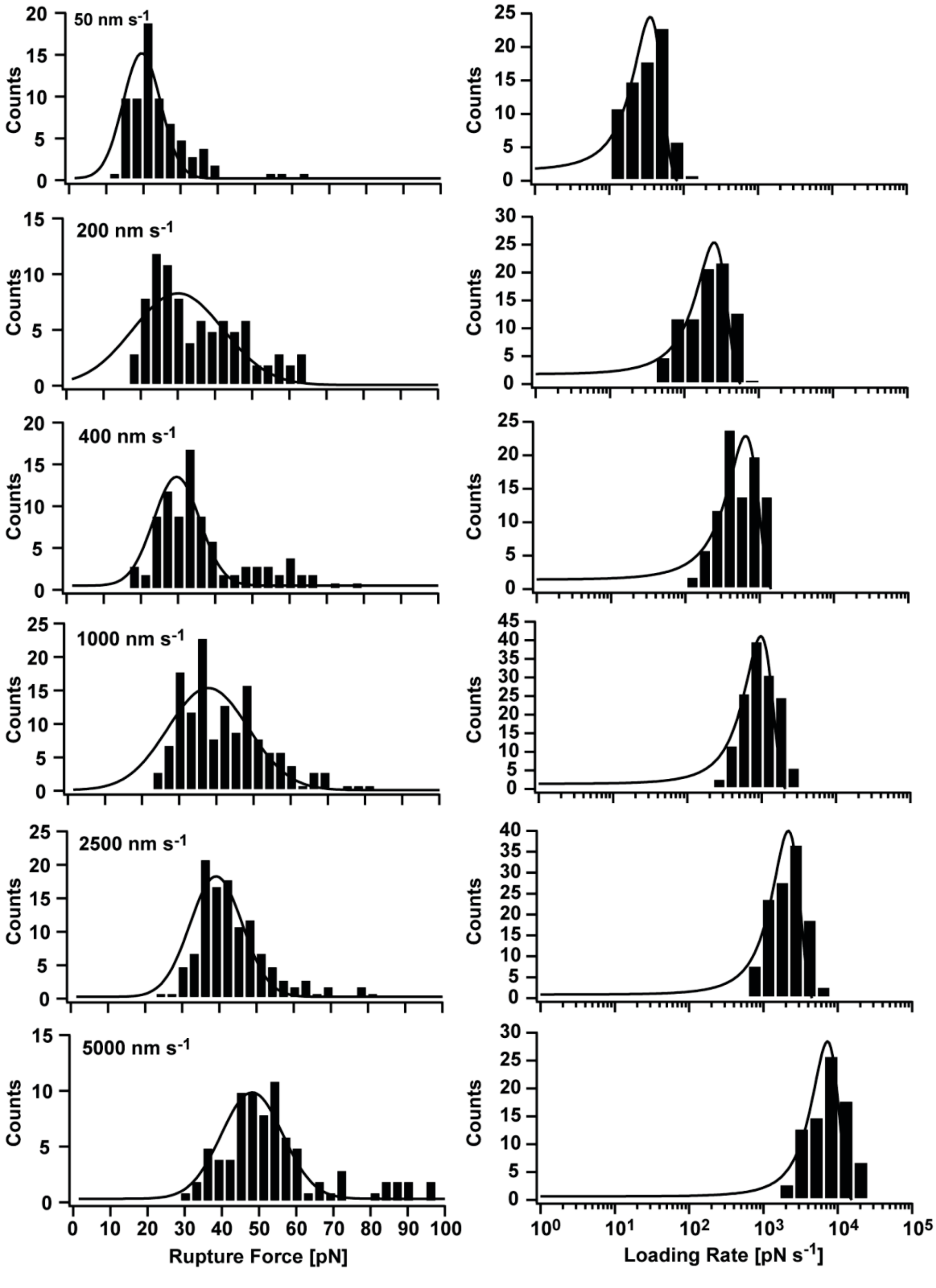

Figure S6. Data set (Cantilever 2) for CC-$A_4B_{3.5}$ measured at 6 different retract speeds. The black lines represent Gaussian fits to the data. The number of rupture events included in each histogram is listed in table S2.

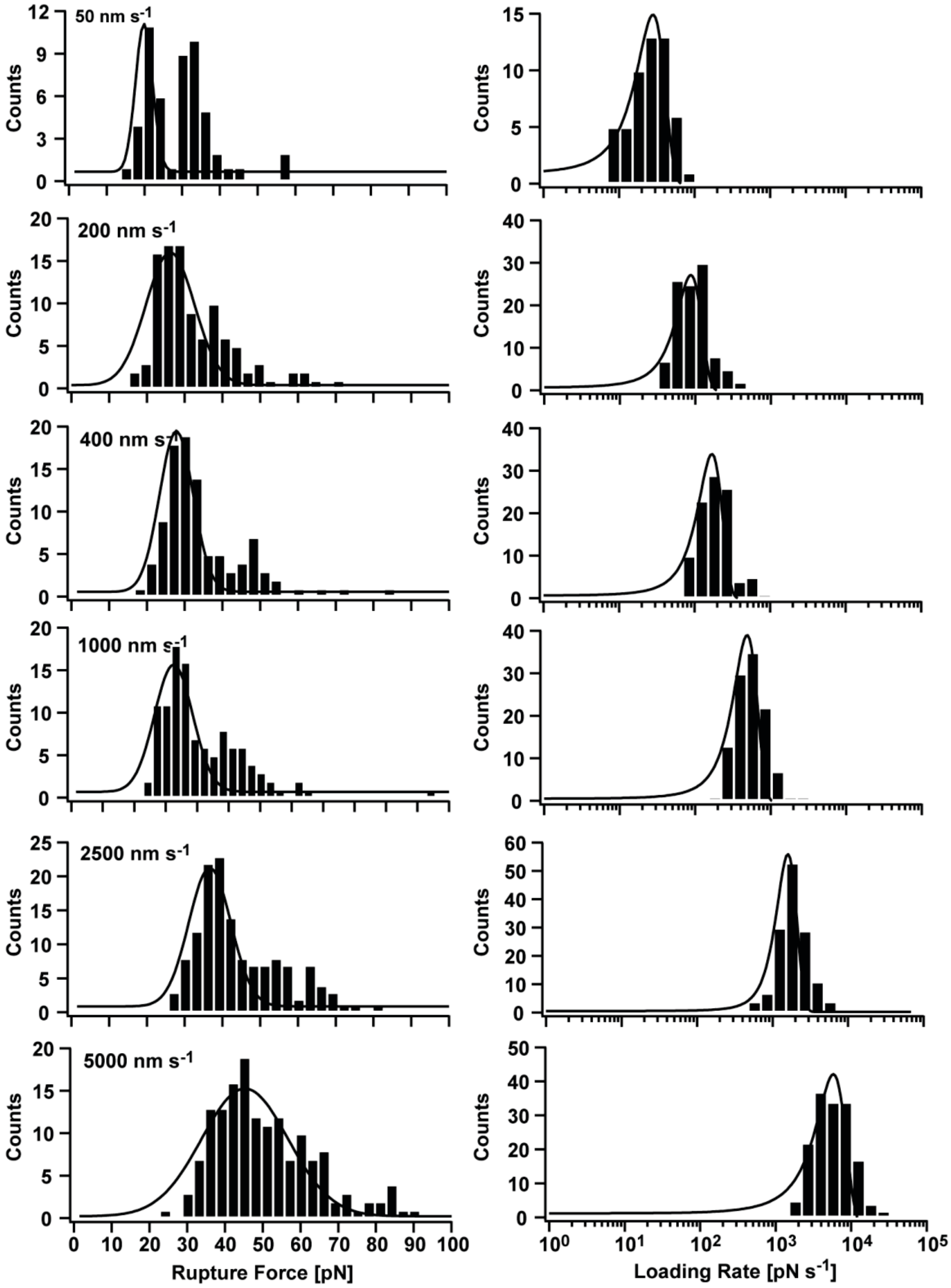

Figure S7. Data set (Cantilever 3) for CC-$A_4B_{3.5}$ measured at 6 different retract speeds. The black lines represent Gaussian fits to the data. The number of rupture events included in each histogram is listed in table S2.

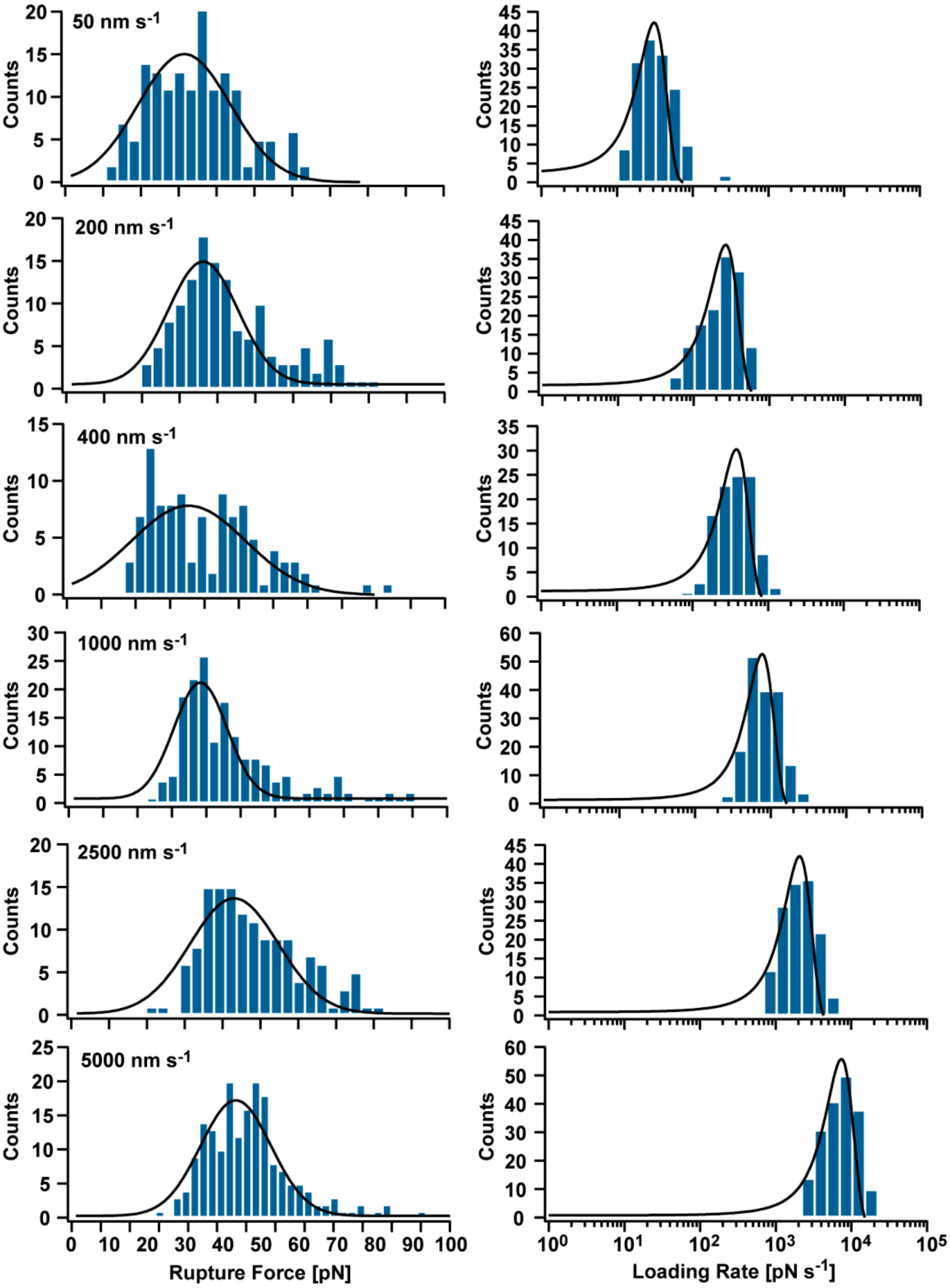

Figure S8. Data set (Cantilever 2) for CC-A_4B_3 measured at 6 different retract speeds. The black lines represent Gaussian fits to the data. The number of rupture events included in each histogram is listed in table S2.

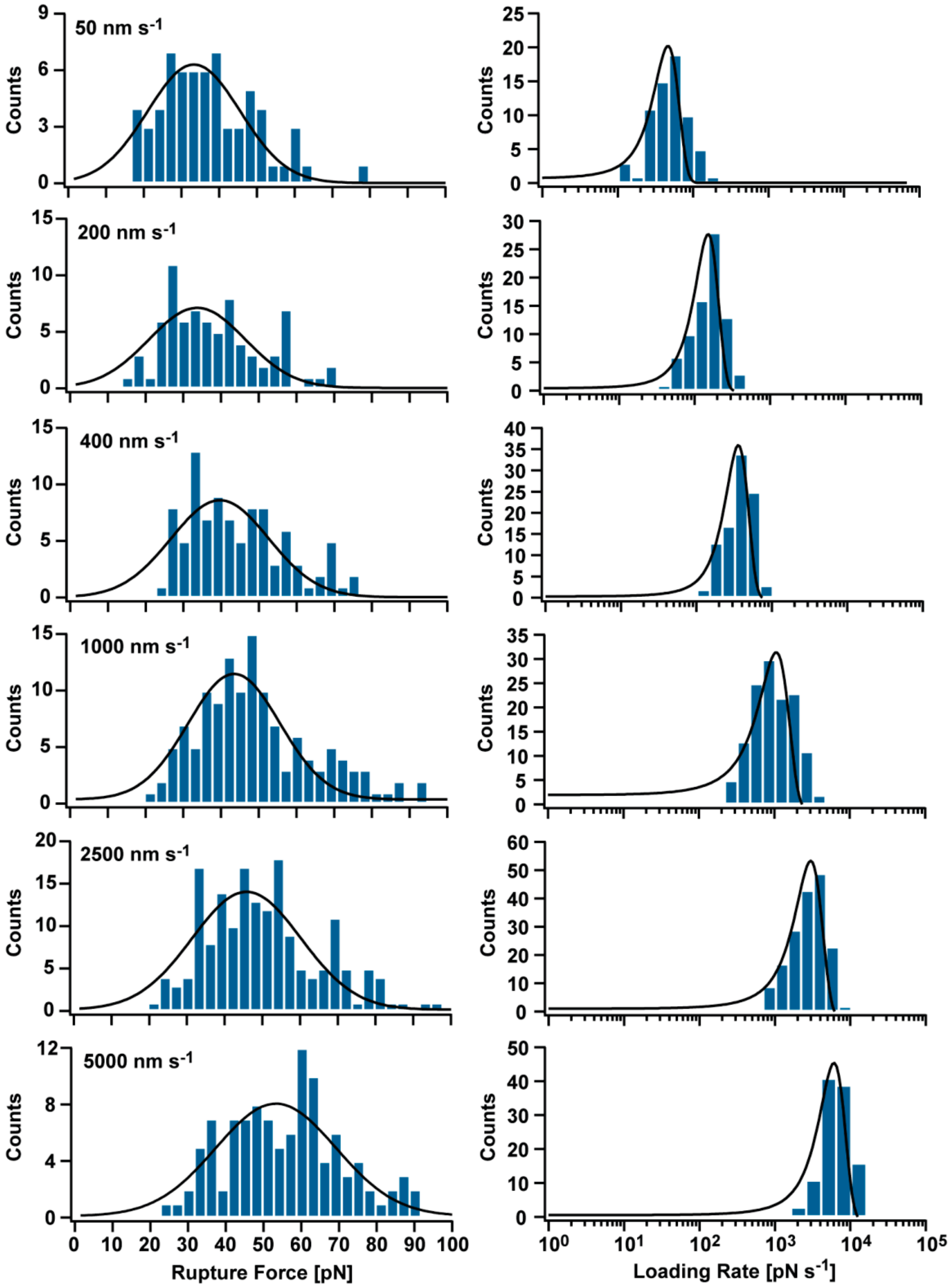

Figure S9. Data set (Cantilever 3) for CC-A_4B_3 measured at 6 different retract speeds. The black lines represent Gaussian fits to the data. The number of rupture events included in each histogram is listed in table S2.

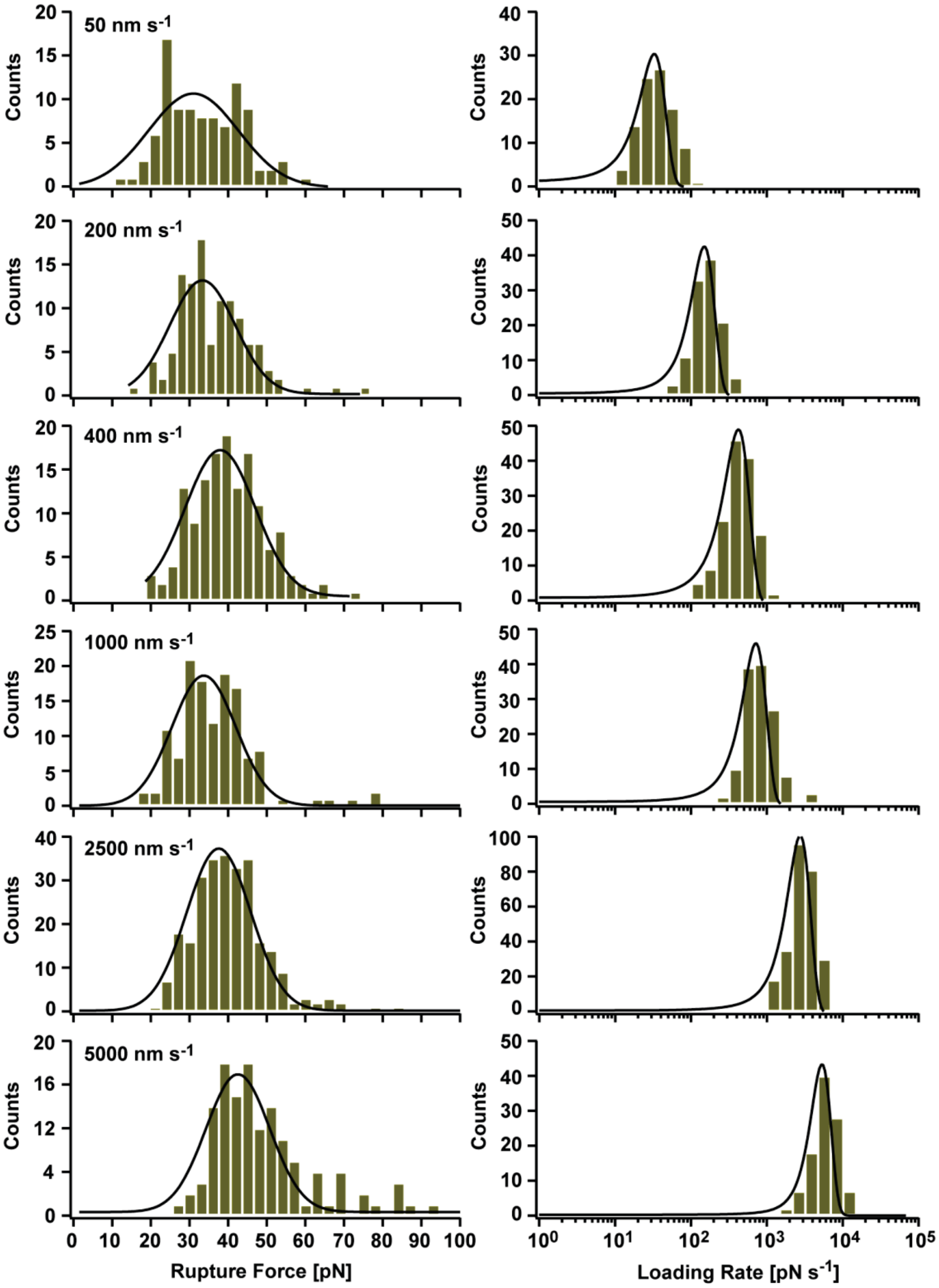

Figure S10. Data set (Cantilever 2) for CC-A_5B_5 measured at 6 different retract speeds. The black lines represent Gaussian fits to the data. The number of rupture events included in each histogram is listed in table S2.

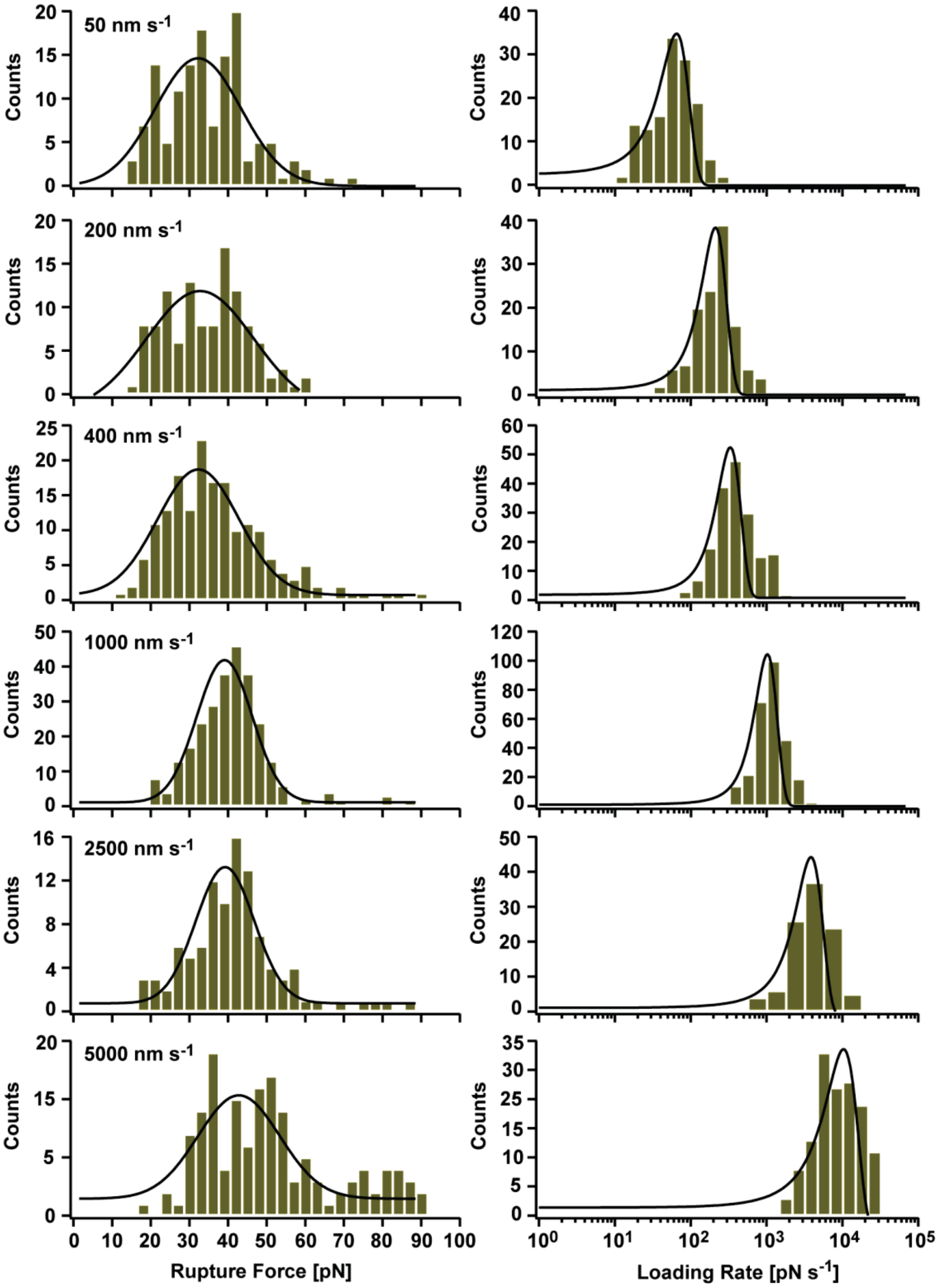

Figure S11. Data set (Cantilever 3) for CC-A_5B_5 measured at 6 different retract speeds. The black lines represent Gaussian fits to the data. The number of rupture events included in each histogram is listed in table S2.

Table S2. Summary of the rupture forces F and loading rates $\dot{F}$ obtained from Gaussian fits to the respective distributions.

		cantilever 1			**cantilever 2**			**cantilever 3**		
heterodimer	***v*** **[nm s^{-1}]**	***n***[a]	***F*** **[pN]**	$\dot{F}$ **[pN s^{-1}]**	***n***[a]	***F*** **[pN]**	$\dot{F}$ **[pN s^{-1}]**	***n***[a]	***F*** **[pN]**	$\dot{F}$ **[pN s^{-1}]**
CC-A_6B_6	50	55	20.3	28	---	---	---	---	---	---
	200	101	30.6	162	---	---	---	---	---	---
	400	76	36.3	420	---	---	---	---	---	---
	1000	124	28.3	469	---	---	---	---	---	---
	2500	107	33.7	1524	---	---	---	---	---	---
	5000	69	63.1	6419	---	---	---	---	---	---
CC-A_5B_5	50	102	33.0	32	98	31.0	33	135	32.2	65
	200	190	34.5	115	114	33.4	150	124	32.7	212
	400	196	35.1	286	145	38.0	422	179	32.3	333
	1000	194	35.9	686	130	33.8	718	277	39.1	1021
	2500	161	36.3	1659	265	37.6	2746	102	39.3	3854
	5000	181	41.6	4718	103	42.5	5325	127	42.9	10367
CC-A_4B_4	50	170	35.1	27	201	34.2	27	84	33.2	30
	200	273	41.2	147	168	40.8	117	224	42.3	117
	400	285	44.0	335	136	43.8	236	294	39.0	237
	1000	260	43.6	711	139	46.4	547	240	47.4	764
	2500	193	47.7	2351	105	48.8	1530	224	48.7	1678
	5000	166	49.5	3972	159	52.0	4807	185	52.7	4987
CC-$A_4B_{3.5}$	50	77	18.5	24	74	19.6	35	---	---	---
	200	133	23.9	79	86	30.0	252	103	26.2	86
	400	187	27.2	158	92	29.6	647	98	27.8	170
	1000	108	34.9	631	144	37.8	974	110	32.5	487
	2500	88	33.1	1846	119	39.1	2159	138	36.7	1593
	5000	127	43.7	5141	82	48.1	7267	155	45.3	5795
CC-A_4B_3	50	139	29.1	25	152	31.5	31	65	33.3	46
	200	158	34.4	155	137	36.2	265	77	33.7	151
	400	145	36.7	239	105	35.4	381	94	39.7	360
	1000	136	38.2	591	172	38.3	769	131	43.5	1058
	2500	70	46.7	3636	139	43.1	2070	174	45.8	2975
	5000	133	49.8	6406	184	56.4	7364	111	53.3	6059

n[a] represents the number of force curves analyzed

Table S3. Summary of the $k_{\text{off\_SMFS}}$ and Δx_{SMFS} values for the different coiled coils CC-A_5B_5, CC-A_4B_4, CC-$A_4B_{3.5}$ and CC-A_4B_3 obtained from Bell-Evans fits of 3 independent measurements. The table also shows the corresponding mean ± SEM.

	individual measurements		**mean values**	
heterodimer	**k_{off} [s^{-1}]**	**Δx [nm]**	**k_{off} [s^{-1}]**	**Δx [nm]**
CC-A_5B_5	3.3×10^{-5}	1.82	$(1.2 \pm 1.1) \times 10^{-5}$	2.14 ± 0.18
	2.1×10^{-6}	2.14		
	1.1×10^{-7}	2.45		
CC-A_4B_4	1.8×10^{-5}	1.52	$(3.2 \pm 2.1) \times 10^{-4}$	1.29 ± 0.12
	2.2×10^{-4}	1.22		
	7.3×10^{-4}	1.12		
CC-$A_4B_{3.5}$	6.8×10^{-2}	0.96	$(1.1 \pm 0.4) \times 10^{-1}$	0.89 ± 0.05
	1.9×10^{-1}	0.79		
	6.9×10^{-2}	0.92		
CC-A_4B_3	3.6×10^{-3}	1.10	$(6.5 \pm 2.4) \times 10^{-3}$	1.03 ± 0.04
	1.1×10^{-2}	0.96		
	4.7×10^{-3}	1.03		

A4 Uncoiling and α-β transition observed for a 6-heptad CC

SMFS experiments performed on heterodimers with 3-5 heptad repeats demonstrated that these short CCs dissociate after the uncoiling of a small amount of helical structure. Under experimentally relevant loading rates, CCs with a length of 3-4 heptads most likely dissociate before the plateau phase (phase II) is reached, while a 5 heptad-long CC can rupture in phase I just before reaching the force plateau or right at the plateau phase. The SMFS results further indicated that longer CCs can tolerate a larger amount of deformations before they become thermodynamically unstable and dissociate. Overall, these results suggest that a minimum length of 5 heptad repeats is required for CC heterodimers to observe the uncoiling transition under shear geometry.

For the 3-5 heptad long CCs studied, phase III was always missing due to the additional freedom provided by the shear geometry. The shear geometry allows the individual helices to dissociate perpendicular to the force axis at any extension. Therefore, the appearance of phase III is expected to require an even higher thermodynamic stability than provided by 5 heptad repeats. To test if phase III can be detected experimentally with synthetic peptides, a 6 heptad long heterodimer (CC-A_6B_6) was designed (**Figure S12A**). To maintain heterospecificity and destabilize undesired homodimers as well as other heptad registers, a second asparagine was included into the 5th heptad of CC-A_6B_6. As can be seen in the CD spectra of CC-A_6B_6 (Figure S3), this strategy may not have been successful. It appears that the individual peptides form homodimers, while CC-A_6B_6 assembles into fiber-like structures.

Despite these possible problems, SMFS was performed to obtain first hints about possible CC-A_6B_6 heterodimer formation. Indeed, a number of force-extension curves was obtained, which fulfilled the criteria defined for a specific rupture event. These force-extension curves, recorded at a retract speed of 400 nm s^{-1}, show that CC-A_6B_6 ruptures during any of the possible 3 phases. Similar to the CC-A_5B_5 results, a small portion (<5%) of the force-extension curves demonstrate a transition to phase II and even phase III (**Figure S12B, C**). The high frequency of rupture events occurring during phase I, indicates that uncoiling-assisted dissociation is still the dominant strand separation mechanism even for CC-A_6B_6.

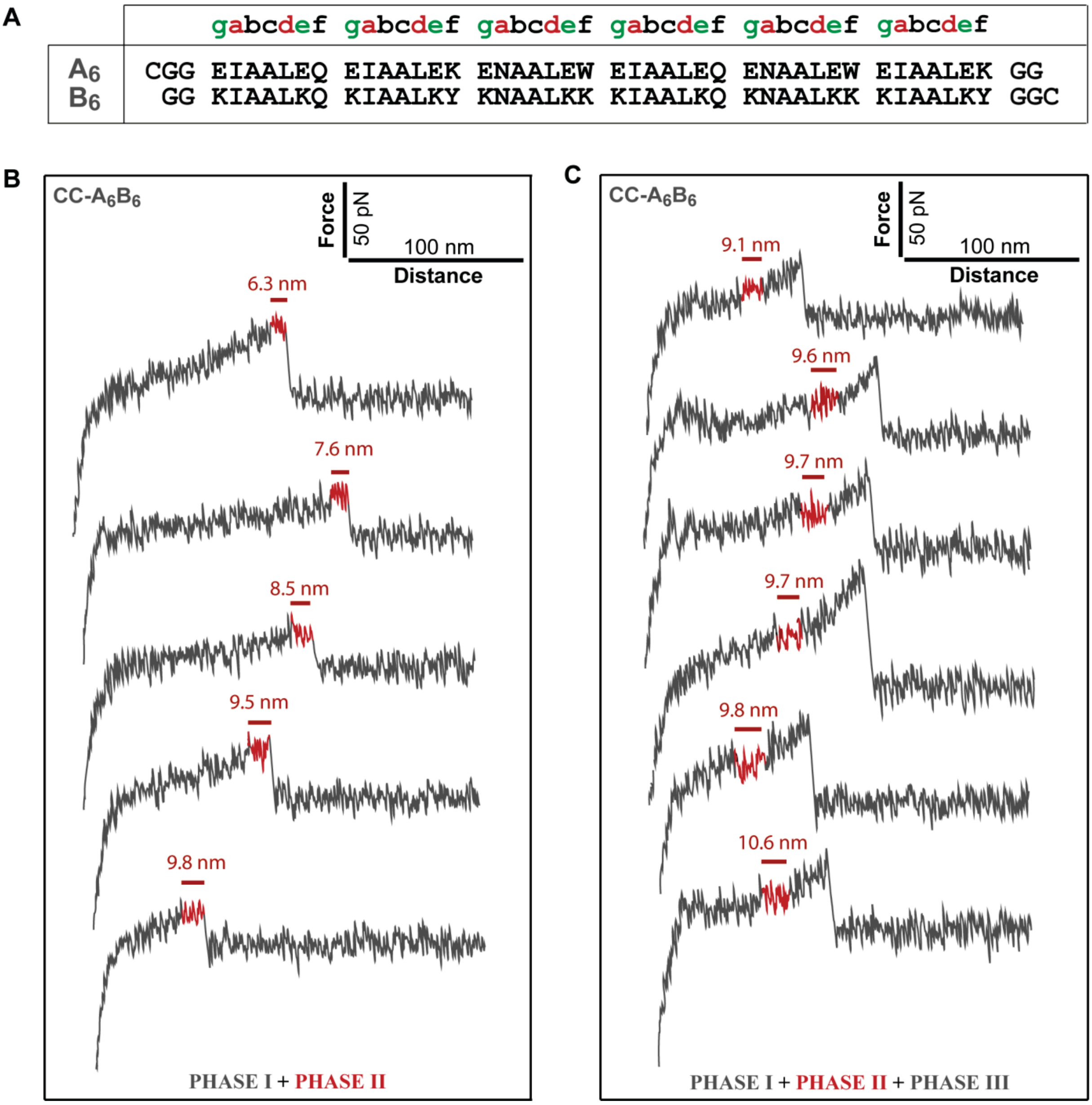

Figure S12. SMFS of CC-A_6B_6. A) Sequence of the CC-A_6B_6 heterodimer. B) Force-extension curves exhibiting the phase I to phase II (plateau phase) transition only. A short plateau (labelled in red) is seen before the rupture event. The data was recorded at a retract speed of 400 nm s^{-1}. C) Force-extension curves exhibiting a complete 3-phase structural response (phase I + phase II (plateau phase) + phase III). The red lines represent the plateau phase. The data was recorded at a retract speed of 400 nm s^{-1}.

Due to small differences in the designed sequences, the heptad at the C-terminal force application point was different for CC-A_5B_5 and CC-A_6B_6. The helical stability of individual mechanically loaded turns might have a direct effect on the overall mechanical stability of the structure, since helix uncoiling starts at the force application points and propagates along the helical axis. Therefore, a direct comparison of the observed plateau forces for CC-A_5B_5 (~20-50 pN) and CC-A_6B_6 (~20-45 pN) may not be possible, yet they were in a similar range. For the force-extension curves exhibiting a full 3-phase response, following the plateau phase, a steeper increase in the force was observed, which may represent the stretching of possible β-sheet structures, overlaid by the polymer extension behavior of PEG (**Figure S12C**). At the current stage, it is not possible to conclude that the observed stretching behavior is indeed the result of the α-β transition. As mentioned above, CD spectroscopy measurements indicated that CC-A_6B_6 has the tendency to form fiber-like structures (**Figure S3**). Under these circumstances, the observation of a 3-phase behavior may not be the mechanical response of a single heterodimer to the shear load. Instead, higher order fibrous assemblies might mimic a mechanical response similar to natural CC fibers. To fully resolve the molecular mechanical response of CC-A_6B_6, a detailed structural analysis of the CC-assembly and further molecular dynamics simulations are required. Also, additional experiments with an optimized heterospecific sequence will be required to confirm the appearance of the α-β transition and to determine its loading rate dependence.

As the majority of the force-extension curves did not show any obvious signs of phases II and III, the data obtained at 6 different retract speeds were analyzed in the usual way. The obtained rupture force histograms were generally not Gaussian and exhibited a small tail at higher rupture forces, especially at medium retract speeds (200-2500 nm s^{-1}) (**Figure S13**). This high force tail might reflect the presence of rupture events occurring in different phases. One may hypothesize that the main peak observed at lower forces represents rupture events occurring in phase I, while the high force tail represents the small number of ruptures in phases II and III. To fully confirm this hypothesis, a more detailed analysis is still required. Due to this undefined distribution pattern (not Gaussian), the data was not analyzed further.

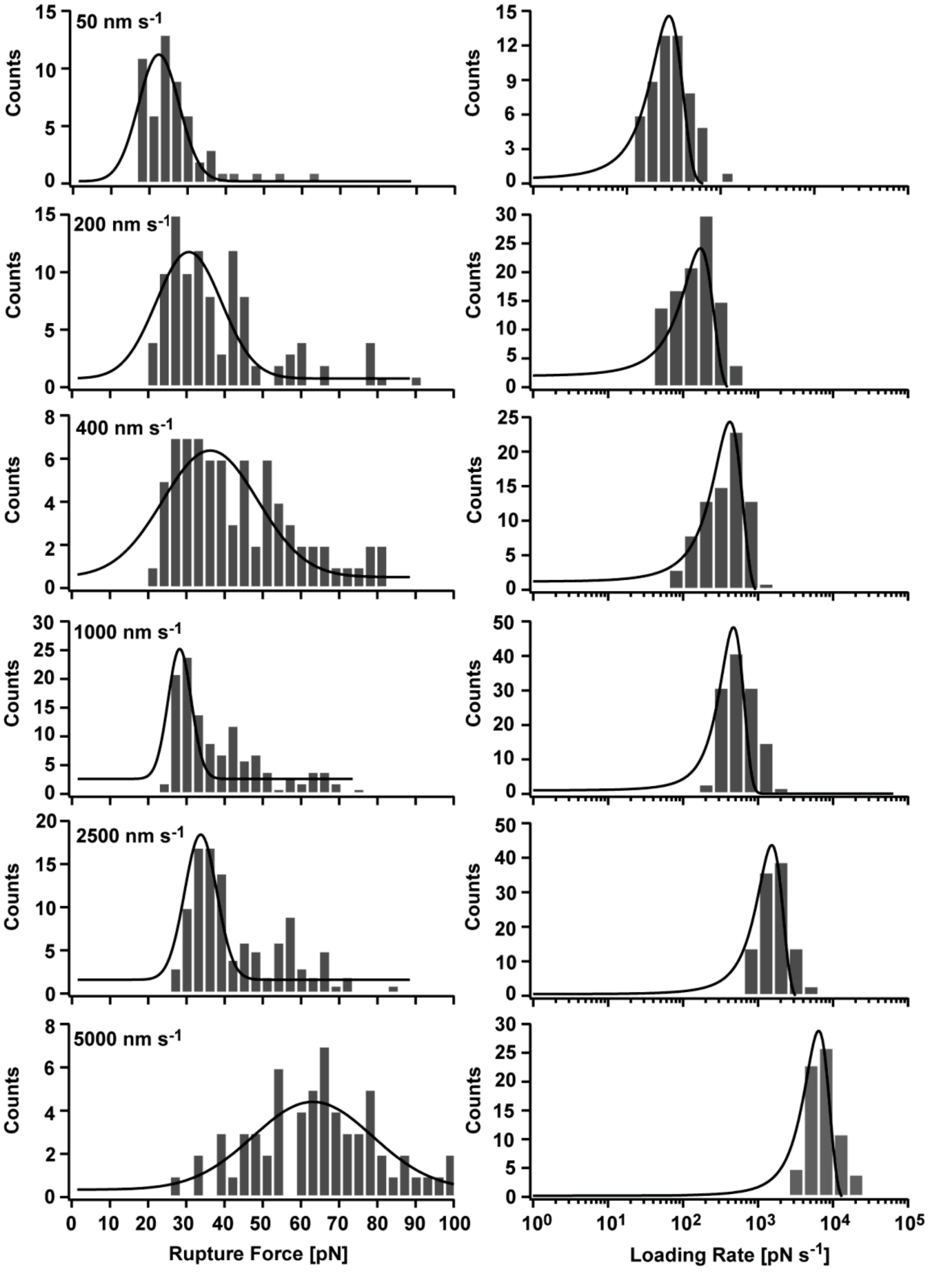

Figure S13. Example data set of CC-A_6B_6 measured at 6 different retract speeds. The black lines represent Gaussian fits to the data. The number of rupture events included in each histogram is listed in table S2.

A5 Characterization of the morphology and cytoskeletal organization of endothelial cells carrying mutations linked to cell-adhesion and mechanosensing

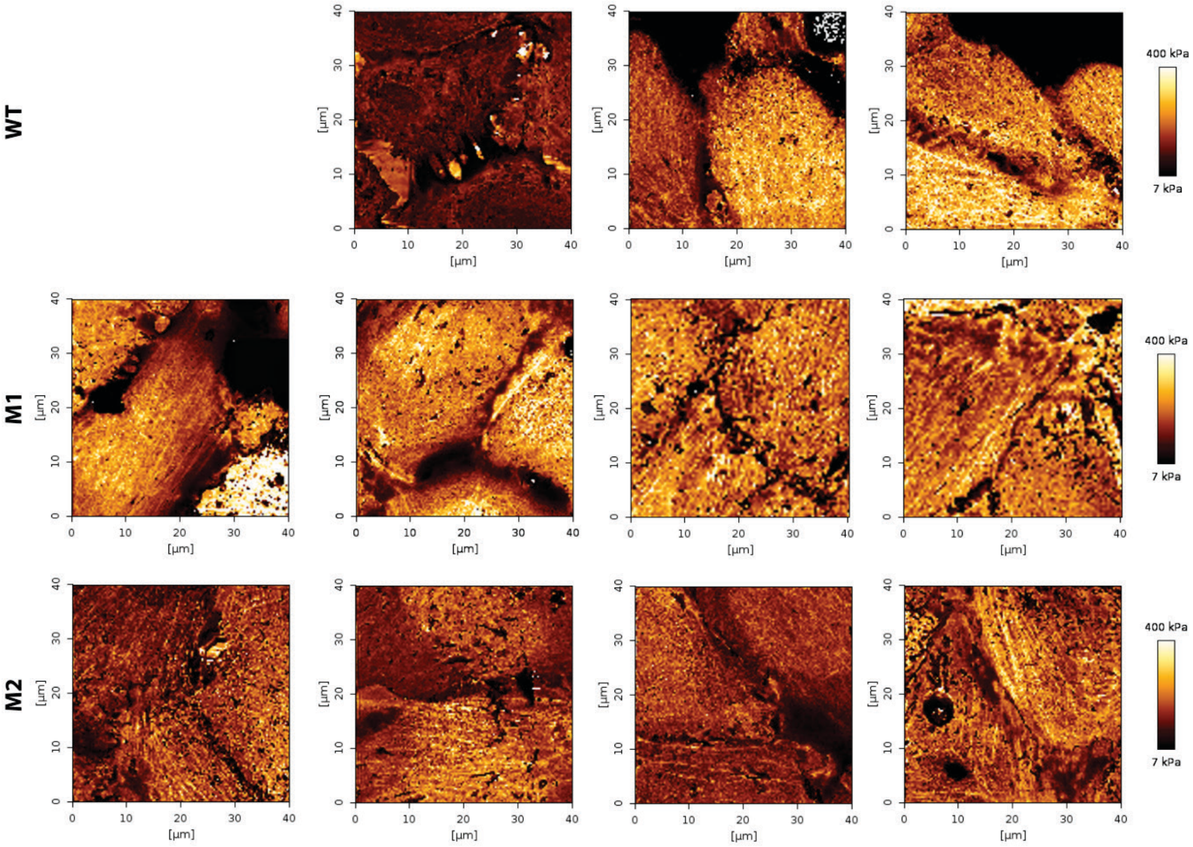

Figure S14. Representative stiffness (Young's modulus) maps, showing the general features of the cytoskeletal organization for WT, M1 and M2 endothelial cells.

A6 Time-dependent cell adhesion experiments

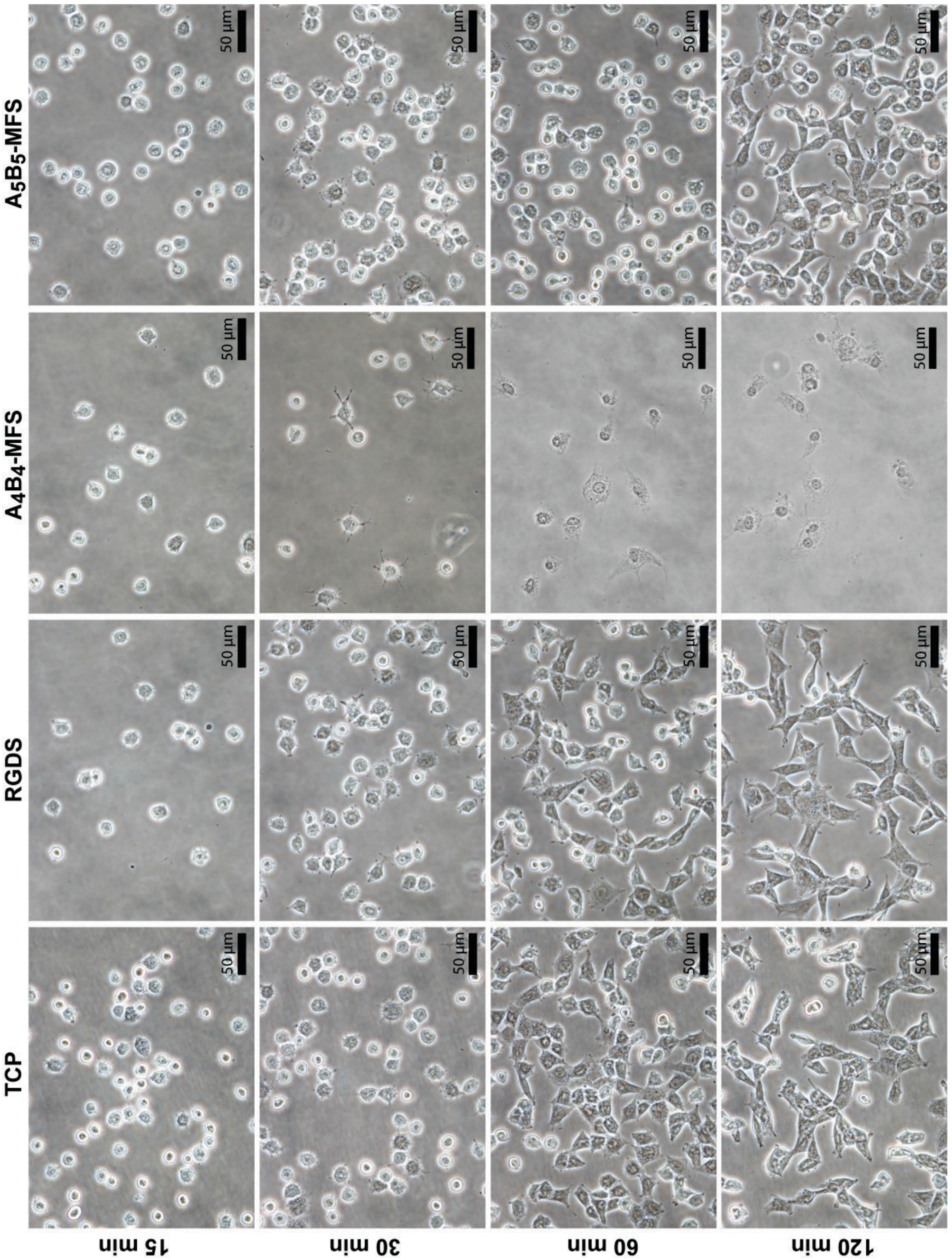

Figure S15. Phase-contrast images of 3T3 fibroblasts grown on TCP and glass surfaces functionalized with RGDS, A$_4$B$_4$-MFS and A$_5$B$_5$-MFS. The images were taken after 15, 30, 60 and 120 min. Scale bars: 50 µm.

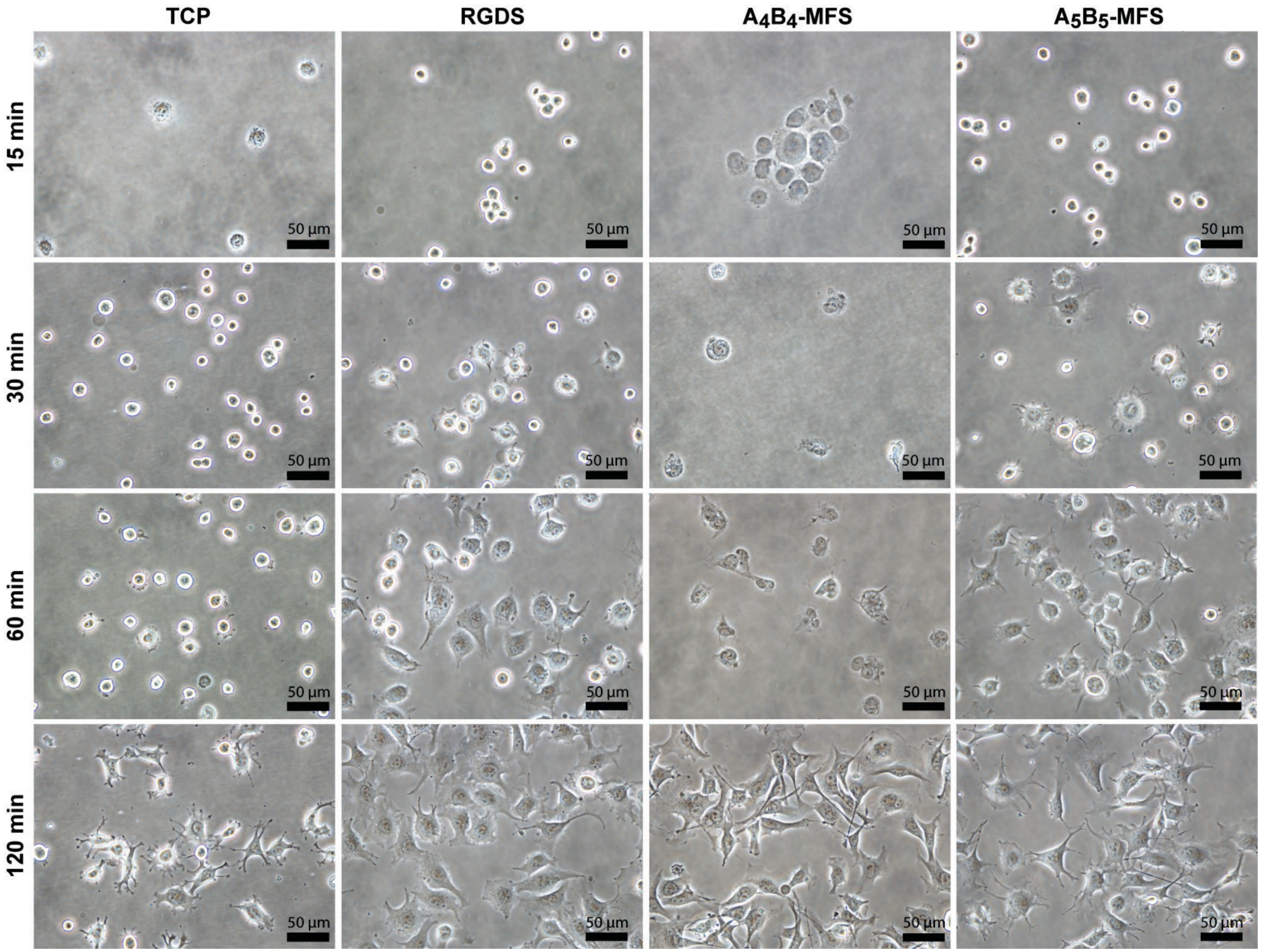

Figure S16. Phase-contrast images of WT endothelial cells grown on TCP and glass surfaces functionalized with RGDS, A_4B_4-MFS and A_5B_5-MFS. The images were taken after 15, 30, 60 and 120 min. Scale bars: 50 µm.

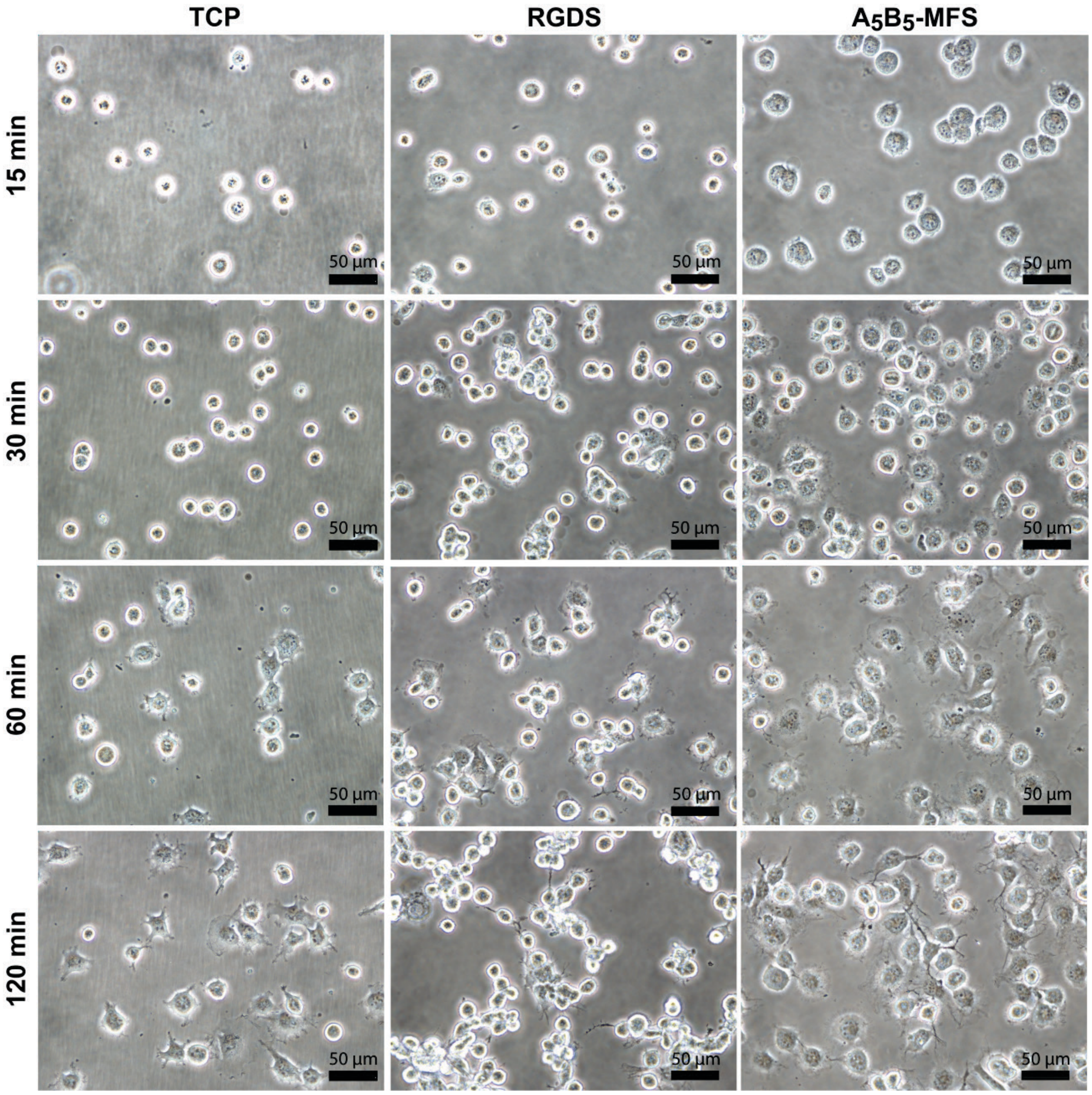

Figure S17. Phase-contrast images of M1 endothelial cells grown on TCP and glass surfaces functionalized with RGDS and A_5B_5-MFS. The images were taken after 15, 30, 60 and 120 min. Scale bars: 50 µm.

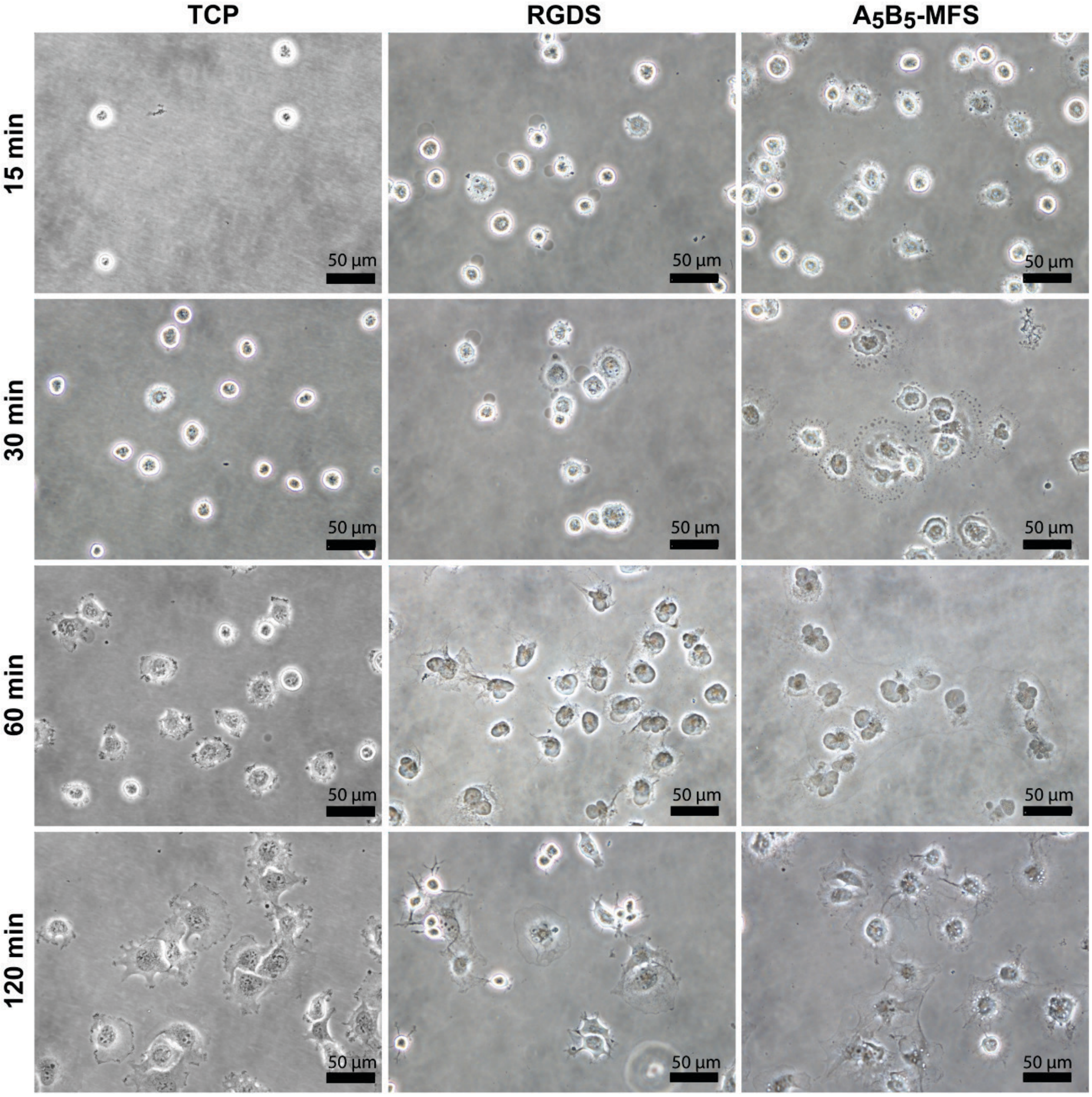

Figure S18. Phase-contrast images of M2 endothelial cells grown on TCP and glass surfaces functionalized with RGDS and A_5B_5-MFS. The images were taken after 15, 30, 60 and 120 min. Scale bars: 50 µm.

A7 Effect of cell-adhesive ligand density on the adhesion behavior of endothelial cells

To investigate the effect of the RGDS ligand density on cellular adhesion behavior, WT endothelial cells were cultured on glass surfaces functionalized with different concentrations of RGDS and A_5B_5-MFS. The concentration of GGGRGDS and B_5-RGDS used for the formation of A_5B_5-MFS was altered from 1 to 500 µM during the immobilization. For the higher ligand concentration (50-100 µM for RGDS control; 10-500 µM for A_5B_5-MFS), cell adhesion was promoted efficiently (**Figure S19**). For lower ligand concentrations, cell-ECM interactions did not form, probably because of the low number of available RGDS ligands. In the absence of integrin-ligand interactions, the formation of cell islands is promoted, which is a result of more pronounced cell-cell interactions. The difference in the critical minimum concentration (50 µM for RGDS control; 10 µM for A_5B_5-MFS) required for cell adhesion to functionalized surfaces might result from different ligand spacing introduced during the immobilization procedure.

Even though cell adhesion was still supported at low RGDS concentrations, distinct differences in the morphology of the adhered cells were observed (**Figure S19**). The spreading areas were generally larger for high RGDS densities (500 µM for both cases), while the cells adapted a spindle-shaped morphology with elongated protrusions when the ligand concentration was decreased. This morphological change is likely a result of the increased ligand spacing.

In the future, a nanoarray-like immobilization strategy can be applied to the current system for generating surfaces functionalized with an ordered distribution and controlled spacing of CC-based MFSs. This will allow for further investigating the effect of different MFSs on the adapted cell morphology and focal adhesion shape. Such a system can also provide defined single-molecule mechanical cues to the cells via altering the combined spacing and mechanical stability of individual MFSs on the surface. This will ultimately define the formation of focal adhesions in a controlled manner and, consequently, shape cell fate via altered mechanoregulation.

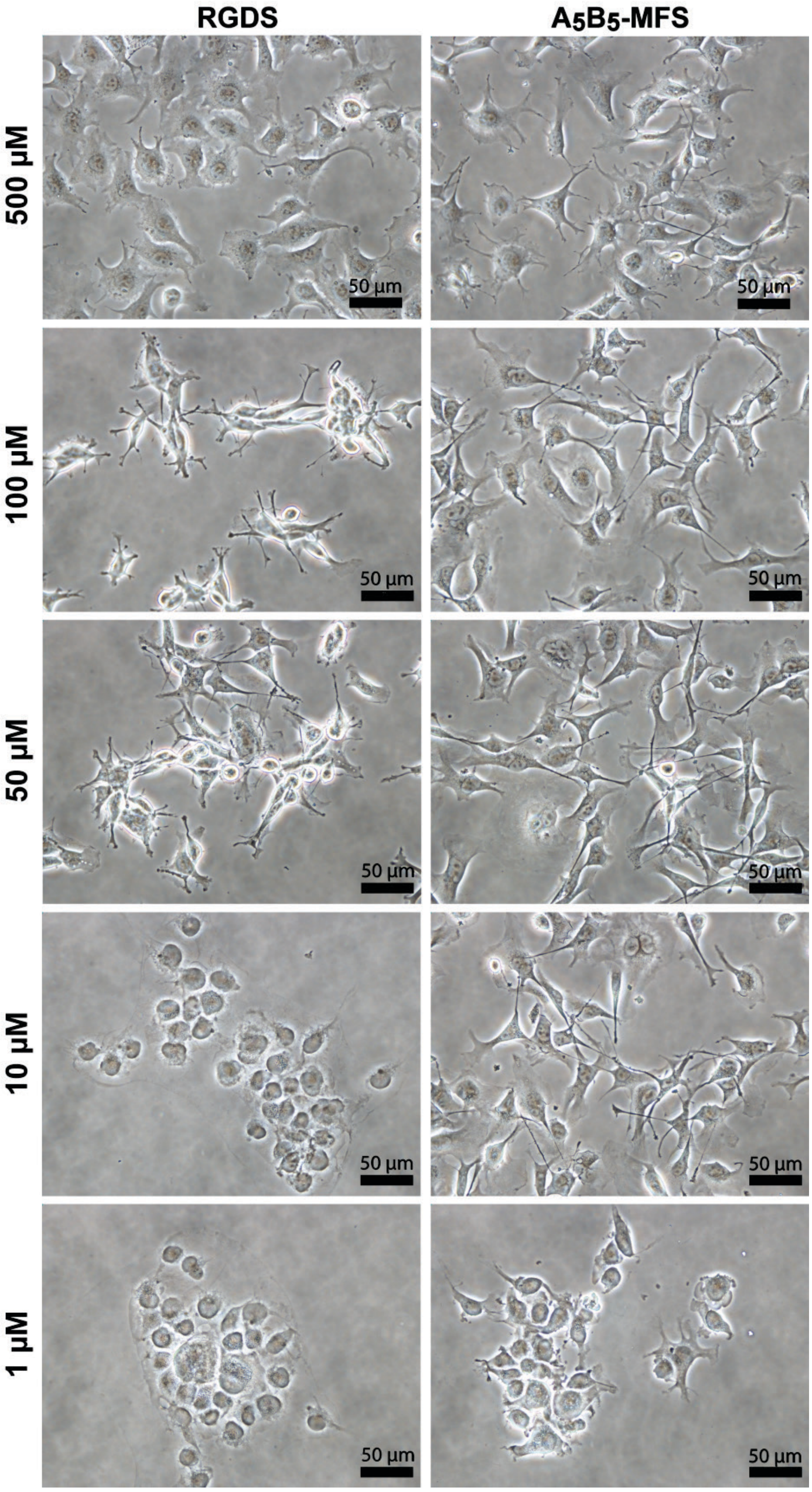

Figure S19. Phase-contrast images of WT endothelial cells grown on glass surfaces functionalized with RGDS and A_5B_5-MFS. The images were taken after 120 min of incubation. Scale bars: 50 µm.

Acknowledgements

I have spent four years in a great research environment with many valuable people. First of all, I would like to thank my supervisor Dr. Kerstin Blank for her support and guidance. Without her scientific advice, support and patience, this work would have not been possible.

I would also like to thank Prof. Dr. John Dunlop and Dr. Klaus Tauer for their further feedback and mentorship. Special thanks to Prof. Dr. Reinhard Lipowsky, Dr. Ana Vila Verde, Dr. Chuanfu Luo and Dr. Ana Bergues for their collaboration and priceless contribution for the SMD simulations leading to a very nice publication. I also thank Prof. Dr. Petra Knaus and Dr. Christian Hiepen for providing the endothelial cell lines for my experiments and for their valuable feedback.

I especially thank Reinhild Dünnebacke, Stefanie Riedel and Anne Heilig whose help in the institute makes everything inevitably easier for a little PhD student!

I would like to acknowledge the International Max Planck Research School (IMPRS) on Multiscale Bio-Systems for giving me the opportunity to conduct my doctoral research within this highly interdisciplinary graduate program at the Max Planck Institute of Colloids and Interfaces, where I also got the chance to meet not only great researchers but also many valuable friends.

To my colleagues and friends: it has been a great journey to meet you and work with you all for the last four years. Thanks for always cheering me up and for all the scientific/non-scientific discussions, coffee/lunch breaks, dinners and drinking sessions. Thank you Eddie, João, Tania, José, Sadra, Sara and Yanni as the first batch of people, together I have spent my first year in Germany, whose presence didn’t leave any room for adaptation issues to a new environment for me! Thank you Agnese, Lorena, Emilia, Alberto, Ale, Batu for the extra fun and unforgettable memories and Bastian for dealing also with my dark side apart from the good times! Special thanks to Patricia for being a constant source of influence in my life for the last three years! Last but not least, Dr. Ruby Sullan, you are such a great scientist and an amazing friend! Thank you for helping me through my baby steps in the beginning of my PhD, and for all the scientific and moral support!